Towards Diffractive Imaging with Single Pulses of FEL Radiation: Dynamics within Irradiated Samples and their Influence on the Analysis of Imaging Data

Dissertation

zur Erlangung des Doktorgrades
des Department Physik
der Universität Hamburg

vorgelegt von

Fenglin Wang

aus Anhui, China

Hamburg
2010

Gutachter/in der Dissertation :	Dr . habil . Beata Ziaja-Motyka Prof . Dr . Henry N. Chapman
Gutachter/in der Disputation :	Dr . habil. Beata Ziaja-Motyka Prof . Dr . Edgar Weckert
Datum der Disputation :	22. Juli 2010
Vorsitzender des Prüfungsausschusses :	Prof . Dr . Alexander Lichtenstein
Vorsitzender des Promotionsausschusses :	Prof . Dr . Jochen Bartels
MIN-Dekan des Fachbereichs Physik :	Prof . Dr . Heinrich H. Graener

Abstract

3D single particle coherent diffraction imaging (CDI) of bioparticles (such as proteins, macromolecules and viruses) is one of the main possible applications of the new generation of light sources: free-electron lasers (FELs), which are now available at FLASH (Hamburg, Germany) and LCLS (Stanford, U.S.A.). The extremely bright and ultrashort FEL pulses potentially enable CDI to achieve high resolution down to subnanometer length scale.

However, intense FEL pulses cause serious radiation damage in bioparticles, even during single shots, which may set the resolution limits for CDI with FELs. Currently, since the signal-to-noise ratio is very low for small biological particles, direct experimental study of radiation damage in the single particle imaging is fairly difficult. Single atomic (noble gas) clusters become good objects to reveal effects of radiation damage processes on CDI with FEL radiation.

This thesis studies three aspects of the radiation damage problem, which are treated in three independent chapters: (1) Molecular Dynamics simulations to quantitively describe radiation damage processes within irradiated atomic clusters during single pulses; (2) reconstruction analysis of single-shot CDI diffraction patterns of atomic clusters, which may potentially help to understand the radiation damage occurring in biological samples; and (3) testing the effects of coating water layers in CDI, which is supposed to minimize the radiation damage in irradiated bioparticles.

List of papers

This thesis is based on the following papers:

- *Paper I*
  Inverse bremsstrahlung cross section estimated within evolving plasmas using effective ion potentials
  F. Wang, E. Weckert and B. Ziaja
  J. Plasma Physics **75** 289–301 (2009).

- *Paper II*
  Multi-electron-recombination rates estimated within dense plasma
  B. Ziaja, *F. Wang* and E. Weckert
  High Energy Density Physics **5** 221–224 (2009).

- *Paper III*
  Energetics, ionization, and expansion dynamics of atomic clusters irradiated with short intense vacuum-ultraviolet pulses
  B. Ziaja, H. Wabnitz, *F. Wang*, E. Weckert and T. Möller
  Phys. Rev. Lett. **102** 205002 (2009).

- *Paper IV*
  Emission of electrons from rare gas clusters after irradiation with intense VUV pulses of wavelength 100nm and 32nm
  B. Ziaja, T. Laarmann, H. Wabnitz, *F. Wang*, E. Weckert, C. Bostedt and T. Möller
  New Journal of Physics **11** 103012 (2009).

- *Paper V*
  Coherent diffraction of a single virus particle: the impact of a water layer on the available orientational information
  F. Wang, E. Weckert, B. Ziaja, D.S.D. Larsson and D. van der Spoel
  Submitted.

Contents

Chapter 1

Dynamics within Irradiated Atomic Clusters

1.1 Introduction

Free-electron lasers (FELs), as the fourth generation light sources, have unique properties such as high peak brilliance and short pulse lengths. They combine these advantages which synchrotron radiation or table-top lasers already have. FLASH at DESY, as the first FEL facility in the world [1, 2], is a powerful tool to study matter properties, such as geometry and electronic structure, chemical composition and magnetic structure. Pulses of 10-200 femtoseconds allow measurement of ultrafast dynamics. Pulses with energies of up to 30-100 μJ in a focus of around 20×20 μm^2 can heat nanoscale samples to temperatures almost ten times higher as those of the solar surface. Hence, this new light source offers unique prospects for studies of matter properties. In this work, atomic clusters interacting with the FEL radiation at FLASH are studied.

Atomic clusters fill the gap between molecular and bulk solids. On one hand, they are almost spherical and have a loosely-bound structure, making them closely approximate a simple model of molecules. The study of the atomic clusters can reveal possible radiation damage processes in single-shot diffraction imaging of single biological particles (such as proteins, viruses, etc.). On the other hand, they have densities similar to solids, but unlike bulk solids they cause no energy dissipation into surrounding media when irradiated by intense lasers. The atomic cluster is an ideal test object for the study of interaction between matter and lasers. Therefore, the study of atomic clusters irradiated by FELs meets much interest.

In this chapter, the ionization dynamics of the irradiated clusters is investigated through a Molecular Dynamics (MD) model. The experimental results from ionic mass spectra and photoelectron emissions are successfully reproduced by this model. Current work is focused

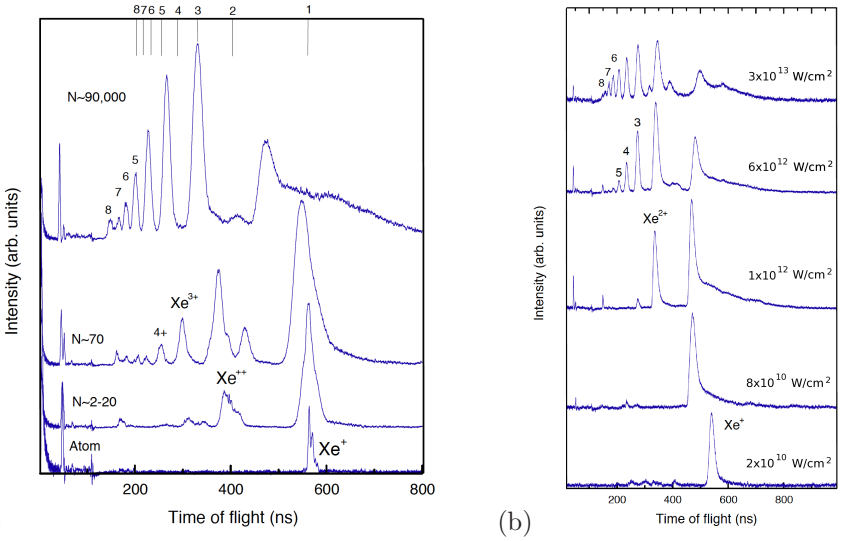

Figure 1.1: Time-of-flight (TOF) mass spectra of xenon atom and clusters ionized by ∼50 fs long FEL pulses at wavelength 100 nm [4]: (a) various cluster sizes at average power density of 8×10^{12} W/cm^2 ; (b) Xe_{2500} clusters at various power densities.

on clusters of single species (such as xenon and argon) irradiated at wavelengths of 100 and 32 nm.

The first cluster experiments with FEL radiation were performed at the facility FLASH at DESY [3]. The xenon clusters were ionized by vacuum ultraviolet (VUV) FEL radiation at a wavelength of 100 nm ($\hbar\omega = 12.7$ eV), and the ions were measured by time-of-flight mass spectrometer. The ionization threshold of a xenon atom is 12.1 eV, slightly below the photon energy. In the case of an isolated atom, only singly-charged ions were observed (Fig. 1.1a). This indicates that no multi-photon ionization process occurs in an isolated xenon atom. In the case of clusters, higher charges than 1+ were detected at a laser intensity of 8×10^{12} W/cm^2 . The ion charge can be up to 8+ when the clusters had sizes of 90,000 atoms. It was estimated in the experiments that about 30 photons per atom were efficiently absorbed within large clusters. The broad mass peaks, with tails and shifts of their positions, come from both space charge effects and different initial kinetic energies of ions before entering the mass spectrometer.

The population distribution of ion charge depends not only on the size of the xenon cluster, but also on the laser intensity. In case of xenon clusters with a fixed size of 2500 atoms (Fig. 1.1b), ions of higher charges were observed when the intensity of laser pulses increased. The strong dependence on the pulse intensity shows that some nonlinear processes dominate the ionization of the irradiated clusters. The smooth tails of the Xe^{1+} mass peaks indicate that no heavier fragments (such as Xe_n^+ , $n = 2, 3, ...$) exist, and therefore, the charged parts of the xenon clusters measured disintegrated completely in these cases.

Complete disintegration of highly charged clusters with high charges occurs in noble

gas clusters irradiated with intense infrared (IR) lasers at higher intensity ($> 10^{16}\,\mathrm{W/cm^2}$) [3]. The process of *field ionization* in the clusters is widely accepted to explain the related experimental findings [3]. But for the VUV FEL radiation which is considered here, the Keldysh parameter[1] is much larger than 1 due to the high laser frequency. This means that the *field ionization* process does not play a significant role as in noble gas clusters in the IR regime.

To understand the FEL experimental results, the authors in [3, 4] performed dedicated simulations based on *classical inverse bremsstrahlung* and classical motion of electrons in an electric laser field. This classical inverse bremsstrahlung model describes successfully the absorption of infrared light by ionized clusters. However, this model failed to explain so high energy absorption in the FEL experiments, with a discrepancy of at least of one order of magnitude. The energy absorption is much enhanced in the VUV regime.

Several research groups have proposed explanations on the enhanced energy absorption. Authors in [5, 6] included atomic structure and plasma screening effects into the inverse bremsstrahlung heating mechanism. In a dense plasma, electrons can experience more than standard Coulomb potentials from point charges of atoms. On the other hand, large numbers of quasi-free electrons can screen charges from atoms at long distances. Authors in [7, 8] attributed the enhanced energy absorption to a charged environment with an inhomogeneous charge distribution on the surface of the cluster system. The background charge lowers the ionization thresholds, and therefore higher charges can be created. Authors in [9] suggested a different mechanism of energy absorption through *many-body recombination*: in a strongly coupled plasma system, many-body collisions lead to enhanced recombination of high-charge states to form low-charge states, which can be ionized again by photons.

These improved mechanisms can qualitatively explain the amount of energy absorbed in the irradiated xenon clusters. Naturally, a question comes: do these mechanisms together combine into one complete picture? Such a complete picture could be important to understand the exact dynamics within the irradiated clusters.

This work combines the several possible mechanisms into one model and quantitively explains the ion spectra measured in the experiments mentioned above. To be complete, this work also calculates photoelectron emissions at different wavelengths for xenon and argon clusters within the same model. This complete model can reveal more features of the irradiated atomic clusters, and helps to understand radiation damage processes in single particle imaging.

This chapter is organized in the following way. § 1.2 describes the physical processes that occur in the clusters irradiated by VUV FEL. Then two published papers on inverse bremsstrahlung cross section and recombination rate are presented in § 1.3–1.4. The molecular dynamics model for numerical simulations is presented in § 1.5. Another two published

[1] The Keldysh parameter is defined as $\gamma = \sqrt{I_p/2E_p}$, with ionization potential I_p and ponderomotive energy $E_p = e^2E_0^2/4m_e\omega^2$. ω and E_0 are laser frequency and field strength, respectively. The regimes of field (tunnel) ionization and multi-photon ionization are characterized by $\gamma \ll 1$ and $\gamma \gg 1$ respectively. In the case of single xenon atom in Fig. 1.1a, $\gamma \simeq 29 \gg 1$.

papers on the dynamics simulations of ion and photoelectron follow (§ 1.6–1.7). § 1.8 contains further results and discussions not presented in the published papers, and is followed by a brief summary.

1.2 Physical processes

In this part, the interactions and processes that occur in the clusters are briefly discussed. The ionization dynamics is complex in an atomic clusters irradiated by FELs. The system is in a highly non-equilibrium state during the irradiation. This work treats two wavelengths: 100 nm and 32 nm. We start with the 100 nm one, and later continue with 32 nm.

(i) **Photoionizations of atoms**. The photon energy at wavelength 100 nm is 12.7 eV, which is just above the first binding energy of a xenon atom (12.1 eV). Single photoionizations of atoms occur in a cluster irradiated at the beginning of an FEL pulse. The slow photoelectrons and ions form a cold plasma, which induces further interactions. The multiphoton ionizations of single atom are significantly suppressed as indicated by the experiments (Fig. 1.1a).

For argon atoms at the same wavelength, only double photoionizations can occur because the first ionization energy is 15.8 eV. The two-photon energy (25.4 eV) is below the second ionization energy (27.6 eV), and therefore, an argon atom can be only singly ionized in the process.

(ii) **Inverse bremsstrahlung heating**. Photons can be absorbed by electrons during elastic electron-atom collisions in the clusters. The primary kinetic energy of a photoelectron from a xenon atom is small (0.6 eV at 100 nm wavelength). The inverse bremsstrahlung process may heat the slow electrons and make the collisional ionizations possible. In the classical limit, the absorption or emission of large number of photons at one time can be treated as a continuous process, for instance, in the IR regime. But in the VUV regime, few photon exchange dominates the processes and the classical approximation is not valid [10, 11]. Therefore, quantum mechanical cross sections [12] for the inverse bremsstrahlung should be applied in this regime. In § 1.3, the cross sections are calculated and are found to be sensitive to atomic structure and plasma screening effect in the VUV regime. This heating process plays an important role in the problem of high absorption mentioned in § 1.1.

(iii) **Inelastic and elastic collisions between atoms/ions and electrons**. Atoms or ions can be ionized during collisions with impact electrons. Secondary electrons are released and then increase the electron density in the clusters that may stimulate the heating mechanism (ii). It creates high charges in irradiated clusters. Inelastic collisions may also lead to multistep ionization and excitation of atoms or ions, which will be not considered in the following simulation model (§ 1.5).

The system of the electron gas and ion cluster can be thermalized through the inelastic

collisions. Due to the mass discrepancy between electrons and atoms, the thermalization timescales are very different. The electron gas in the cluster needs a time of the order of 10-100 femtoseconds to thermalize [13], while thermalization of ions take much longer (picoseconds, depending on masses and charge states of atoms). Since energetic photoelectrons escape from the systems, the charged clusters will explode due to Coulomb interactions between ions. The inelastic collisions will be rare when the atoms in the cluster become spread out during the explosion.

(iv) **Many-body recombination of ions with electrons**. This inelastic process can be regarded as the inverse of the process of collisional ionization. The spectator electron(s) close to the ion receives the kinetic energy released by the recombining electron. The recombination process decreases ion charge and the low charge state of the ion could be photoionized again, absorbing more energy from the laser field. The calculations for many-body recombination in § 1.4 show that this process significantly depends on electron density and temperature, and that it cannot be neglected in a charge system with high electron density and low electron temperature.

(v) **Electromagnetic interaction of electrons/ions with laser field**. Laser field can be regarded as a highly-oscillating electric field within the dipole approximation. Since the oscillating field is of high frequency (in the VUV regime) and ions have large masses, the classical interactions of ions with the field are negligible. An electron which is much lighter can be accelerated and decelerated by the field. The electron can exchange energy with the field (i.e. it can absorb or emit) if it stays in potential field of atoms or ions. This is the case discussed in (ii). For a free electron in vacuum, the energy exchange becomes zero when averaged over oscillation circles. Hence, the interactions of electrons with laser field can be neglected when electrons escape from clusters during radiation.

There are two phases occurring in an atomic clusters irradiated by single FEL pulses. The first phase occurs on a timescale comparable to that of the pulse length from the beginning of the pulse. It is highly non-equilibirium, and the processes (i-v) are then involved. The second one follows afterwards, and it is an expansion phase. The cluster system is charged due to the escape of electrons, and this causes its Coulomb explosion. The related processes are (iii) and (iv), which are roughly balanced. In contrast to the first phase, it is quasi-equilibrium with a slow expansion. The simulations in this work are focused on the non-equilibrium phase.

At 32 nm wavelength, only argon clusters will be considered. The photon energy (37.8 eV) is above the second ionization threshold of argon atom (27.6 eV). The photoionization of argon atoms is assumed to be sequential: $Ar^{0+} \rightarrow Ar^{1+} \rightarrow Ar^{2+}$. The first photoelectrons, with energies around 22.0 eV, may easily escape from the argon clusters. The effect of inverse bremsstrahlung becomes much weaker at such short wavelength than that at 100 nm (see § 1.7). The simulations of argon clusters at 32 nm will be discussed in § 1.7.

In the next two sections, the rates (or cross sections) for the interactions (ii) and (iv) are calculated. These two parts have been published.

1.3 Inverse bremsstrahlung cross section estimated within evolving plasmas using effective ion potentials[2]

Abstract

We estimate the total cross sections for field-stimulated photoemissions and photoabsorptions by quasi-free electrons within a non-equilibrium plasma evolving from the strong coupling to the weak coupling regime. Such a transition may occur within laser-created plasmas, when the initially created plasma is cold but the heating of the plasma by the laser field is efficient. In particular, such a transition may occur within plasmas created by intense vacuum ultraviolet (VUV) radiation from a free-electron laser (FEL) as indicated by the results of the first experiments performed by Wabnitz at the FLASH facility at DESY. In order to estimate the inverse bremsstrahlung cross sections, we use point-like and effective atomic potentials. For ions modelled as point-like charges, the total cross sections are strongly affected by the changing plasma environment. The maximal change of the cross sections may be of the order of 75 at the change of the plasma parameters: inverse Debye length, κ, in the range $\kappa = 0 - 3\mathring{A}^{-1}$ and the electron density, ρ_e, in the range $\rho_e = 0.01 - 1\mathring{A}^{-3}$. These ranges correspond to the physical conditions within the plasmas created during the first cluster experiments performed at the FLASH facility at DESY. In contrast, for the effective atomic potentials the total cross sections for photoemission and photoabsorption change only by a factor of seven at most in the same plasma parameter range. Our results show that the inverse bremsstrahlung cross section estimated with the effective atomic potentials is not affected much by the plasma environment. This observation validates the estimations of the enhanced heating effect obtained by Walters, Santra and Greene. This is important as this effect may be responsible for high-energy absorption within clusters irradiated with VUV radiation.

Introduction

Processes of photoabsorption and photoemission by quasi-free electrons within a plasma stimulated by an external laser field have been known and investigated for many years [14, 15, 12, 10, 11, 5, 6, 16]. The process of field-stimulated absorption of radiation quanta is known as inverse bremsstrahlung (IB), and it is an inverse process to the stimulated photoemission. For a plasma in equilibrium the rates for both of these processes obey detailed balance equations [17]. If the number of absorptions is larger than the number of emissions, the thermal energy of electrons increases with time.

There exist various theoretical approaches to model the IB process (for a review see [11, 16]. Their applicability depends on the physical parameters of the system such as the drift velocity of electrons in the laser field, their thermal velocity, and the energy of radiation quanta. The applicability of some models is restricted only to a specific regime defined by these parameters [11]. In what follows we will use the quantum-mechanical approach to calculate the IB cross section, σ_{IB}, as proposed by Kroll and Watson [12]. This approach can be used to describe photoemission and photoabsorption by both slow and fast electrons. In particular, within this approximation, if the field strength parameter, $s = e\mathbf{E}_0/\hbar\omega^2$ is small, and the free electrons are slow, single-photon exchanges dominate. The quantity,

[2]This section has been published as *Paper I*: F. Wang, E. Weckert and B. Ziaja, J. Plasma Physics **75** 289–301 (2009).

$\mathbf{E}_0$, denotes the electric field strength, ω is the photon frequency. For slow electrons, the photoabsorption of n radiation quanta, γ, of energy $\hbar\omega$: $e(E_e) + n\gamma \rightarrow e(E_e + n\hbar\omega)$, may significantly increase the thermal energy of the electrons.

If s is large, or if the free electrons are fast and undergo collisions with ions at large momentum transfers, multi-photon exchanges occur. This latter case can be described by the classical impact picture [12] that is only valid if the drift component of the kinetic energy of the electron is much larger than the photon energy [10].

During IB heating the total energy absorption within the sample can be nonlinear with respect to the exposure time and the pulse intensity, $dE_{abs}/dt \propto N_{ion}(I,t)\sigma_{IB}(I)N_{el}(I,t)$, as the total numbers of ions and electrons, $N_{ion}(I,t)$ and $N_{el}(I,t)$, change with the pulse intensity and the exposure time and, in addition, the cross section, $\sigma_{IB}(I)$, is also a function of the pulse intensity.

The IB process has attracted much attention as a possible mechanism of efficient plasma heating when the results of the cluster experiments with vacuum ultraviolet (VUV) free-electron-laser (FEL) radiation performed at the FLASH facility at DESY became available [3, 4, 18, 19, 20, 21]. These experiments covered the wavelength range from 100 nm ($E_\gamma =$ 12.7 eV) down to 13 nm ($E_\gamma = 95.4\,eV$). single pulse durations did not exceed 50 fs, and the maximal pulse intensity was, $I \propto 10^{14}\,W\,cm^{-2}$.

In the first experiment performed at 100 nm photon wavelength (VUV regime) with Xe_{2500} clusters highly charged Xe ions (up to +8) of high kinetic energies were detected. This indicated a strong energy absorption that could not be explained using standard theoretical approaches [4, 21, 22]. More specifically, the energy absorbed was almost an order of magnitude larger than that one predicted with classical absorption models, and the ion charge states were much higher than those observed during the irradiation of isolated atoms at similar flux densities. This indicated that at this radiation wavelength some processes specific to many-body systems are responsible for the enhanced energy absorption. Several theoretical models have been proposed [5, 7, 23, 9] which could explain various aspects of the increased photoabsorption and ionization dynamics observed in the experiments (for a review see [24]).

The contribution of the IB process, considered as a possible mechanism of the efficient electron heating, was evaluated in detail in [5, 6]. There it was proposed that the strong energy absorption within an irradiated atomic cluster may result from the enhanced IB heating of quasi-free electrons. This enhanced IB rate is estimated with the effective atomic potential [25] which represents the attraction of the nucleus and the average screening effect of bound electrons surrounding the nucleus. An energetic electron that passes through the atom/ion is then scattered by the effective positive charge, Z_{eff}, which is larger than the net charge of the ion. This effect leads to an enhancement of the total IB rate that is proportional to the squared effective charge of the scatterer. This mechanism was first explored in [5]. Simulations of cluster irradiation including this mechanism revealed to the creation of high charges within the irradiated clusters. These high charges were created in

a sequence of electron impact ionizations. The ion charge state distributions were similar to those observed in the experiment [3].

We stress here that the derivation of the IB rate from the effective atomic potentials as performed in [5, 6] is in contrast to the standard approaches that assume Coulomb potentials of point-like ions [14, 15, 11]. However, a heating mechanism similar to the one used in [5] was recently successfully tested in [26]. It was applied to a model the heating of quasi-free electrons in large rare-gas clusters irradiated with infrared laser pulses. These electrons were heated during elastic large-angle backscatterings on ion cores. The potentials of the ions were modelled with the parametrized atomic potential similar to that one in [5]. An absolute x-ray yield obtained with this effective atomic potential was in better agreement with the experimental data than that one obtained with the point-like atomic potential.

Here we aim to investigate in detail how the IB cross sections calculated using effective atomic potential from [5, 26] depend on the changing plasma environment evolving from the strongly coupled to the weakly coupled regime. Up to the authors' knowledge this question has not been addressed so far. Our results will validate the estimations of the heating rate obtained with the effective potentials in [5, 6] by evaluating the impact of the changing plasma conditions on IB cross sections.

As mentioned above, we will consider the limits of strongly and weakly coupled plasmas. The results obtained with effective atomic potentials will be compared to the IB cross sections calculated with point-like potentials.

Our results will give estimates for the accuracy of the IB modelling within the evolving plasma in the regime relevant for the first cluster experiments [3]. Such estimates are important for performing the simulations of plasma heating, especially within plasmas that are created during the interaction of intense radiation with matter [5, 6, 26, 27, 28, 29].

Effective atomic potentials

For our tests we will use two different parametrizations of the effective atomic potential. The first one was also applied in [5] to describe the enhanced heating of electrons within atomic clusters irradiated with intense pulses of VUV radiation. The second one represents the independent-particle-model (IPM) potential introduced in [30] and used in [26] in order to estimate the cross section for elastic scattering of electrons on ions. The general form of these spherically symmetric potentials is:

$$\phi(r) = \frac{1}{4\pi\epsilon_0}\left(\frac{ie}{r} + \frac{(Z-i)e}{r}\Omega(r)\right), \tag{1.1}$$

where the charge Z is the nuclear charge, $i = 0, 1, ...$ denotes the net ion charge. For point-like ions, $\phi_0(r)$, we have: $\Omega(r) = 0$. In [5] an exponential profile is used to model the screening by bound electrons: $\Omega_1(r) = e^{-\alpha_i r}$, where α_i is chosen so that the ionization energy of an ion calculated with this effective potential, $\phi_1(r)$, matches the corresponding experimental value. in [26] the IPM potential [30] $\phi_2(r)$ is used: $\Omega_2(r) = [\eta/\zeta(e^{\zeta r}-1)+1]^{-1}$,

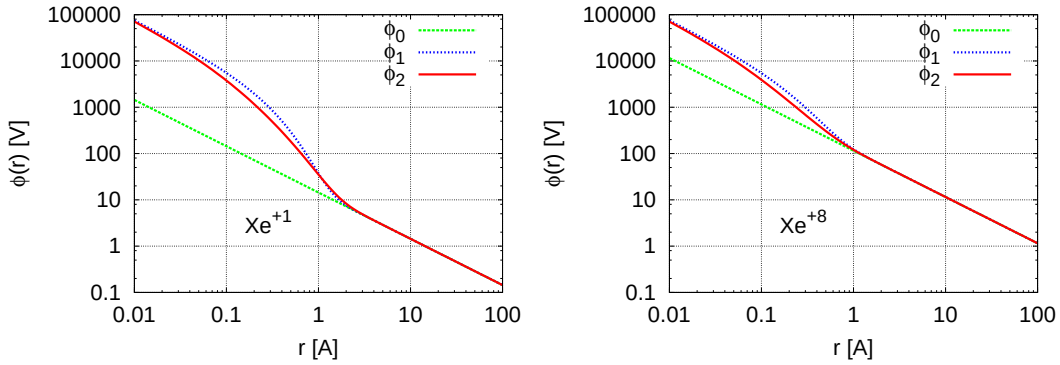

Figure 1.2: Effective atomic potentials for Xe ions. The potential applied in [5], $\phi_1(r)$, and the potential proposed in [30], $\phi_2(r)$, are plotted for Xe^{+1} ion (left), and Xe^{+8} ion (right). The corresponding point-like potentials, $\phi_0(r)$, are also plotted for comparison.

where parameters η , ζ are element-specific and depend also on the ionization stage. We plot the different potentials for Xe ions at two ionization stages, $i = 1$ and $i = 8$ in Fig.1. Despite the different parametrization, the effective potentials are close to each other. As expected, for small values of $r \leq 1\mathring{A}$ (atomic size) there is a large discrepancy between the point-like and the effective atomic potentials. For larger values of r the effective potentials approach the point-like potentials.

The limiting values of $\Omega(r)$, $0 < \Omega(r) < 1$, are identical for both potentials and correspond to the physical limits of: (i) the potential created by a pure nuclear charge, Z, at $r = 0$; and (ii) the potential created by net ion charge, i, at $r = \infty$.

The charge density, $\rho(r)$, that generates these effective potentials, is spherically symmetric and consists of the point-like positive nucleus charge, Z , screened by the cloud of bound electrons:

$$\rho(r) = \frac{Z\delta(r)}{4\pi r^2} - \frac{(Z-i)}{4\pi r}\Omega''(r)\,, \tag{1.2}$$

where $\Omega''(r)$ is the second derivative of $\Omega(r)$. For a point-like ion of net charge, i, the corresponding charge density is:

$$\rho(r) = \frac{i\delta(r)}{4\pi r^2}\,. \tag{1.3}$$

Weakly and strongly coupled plasma

The temperature, density and charges of species determine the physical properties of plasmas. Two parameters are introduced in order to classify various plasma regimes [31]. The Coulomb coupling parameter, Γ, is defined separately for each plasma component as the ratio of its average potential energy to the average kinetic energy, $\Gamma \sim \mid \phi(r)/kT \mid$. If $\Gamma \gg 1$, plasma enters the strong coupling regime, where many-body screening effects are significant.

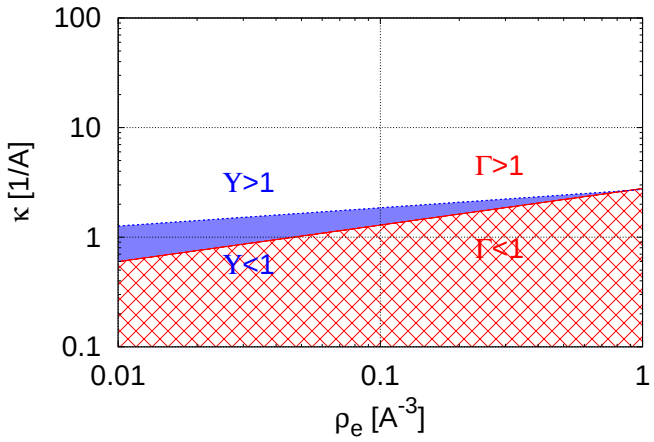

Figure 1.3: Regions of strongly and weakly coupled plasma. Plasma parameters, Γ and Y are plotted as a function of screening parameter, κ, and electron density, ρ_e. The area filled with pattern corresponds to the regime of classical ideal plasma. The area filled with colour represents the regime of strongly coupled classical plasma. The remaining area represents the regime of degenerate, strongly coupled plasma.

If $\Gamma \ll 1$, a plasma is considered to be ideal. The second parameter is the degeneracy parameter, Y, that is the ratio of the Fermi energy of a given plasma component to its average kinetic energy, $Y \sim \mid E_F/kT \mid$. For $Y \gg 1$, quantum statistics should be used (non-classical plasma). For $Y \ll 1$, the plasma can be treated classically.

Various plasma regimes are plotted in Fig. 1.3. They correspond to the estimated physical conditions within the plasmas created during the first cluster experiments performed at the FLASH facility at DESY [3]. For the typical electron densities within xenon clusters in the range of $\rho_e = 0.01 - 1$ Å^{-3} plasmas enter the degenerate strong coupling regime if the Debye screening parameter, $\kappa \equiv \lambda_D^{-1}$ is more than $1 - 3$ Å^{-1}. In this regime the ion-sphere screening should be applied. For lower values of κ the weak coupling approach is valid.

We will first consider the classical plasma regime, where the classical statistical mechanics can be applied to model the screening. If the Coulomb interaction within plasma is weak, $\Gamma \ll 1$, mean field estimates for charge densities can be linearized and the Poisson equation for the potential reduces to the Helmholtz equation of the form:

$$(\nabla^2 - \kappa^2)\phi_D(r) = -4\pi e\rho(r)\,\frac{1}{4\pi\epsilon_0}. \tag{1.4}$$

Solution of this equation can be obtained by the convolution of the charge density with the Green function, $G(\mathbf{r}) = e^{-\kappa|\mathbf{r}|}/\mid \mathbf{r} \mid$. At $\kappa = 0$ this Green function reduces to the Green function for the unscreened Coulomb potential, $G(\mathbf{r}) = 1/\mid \mathbf{r} \mid$. The general solution of the Helmholtz equation then reads:

$$\phi_D(r) = \frac{1}{4\pi\epsilon_0}\int d^3r'\,\frac{e^{-\kappa|\mathbf{r}-\mathbf{r}'|}}{\mid \mathbf{r}-\mathbf{r}' \mid}\,e\,\rho(r')\,. \tag{1.5}$$

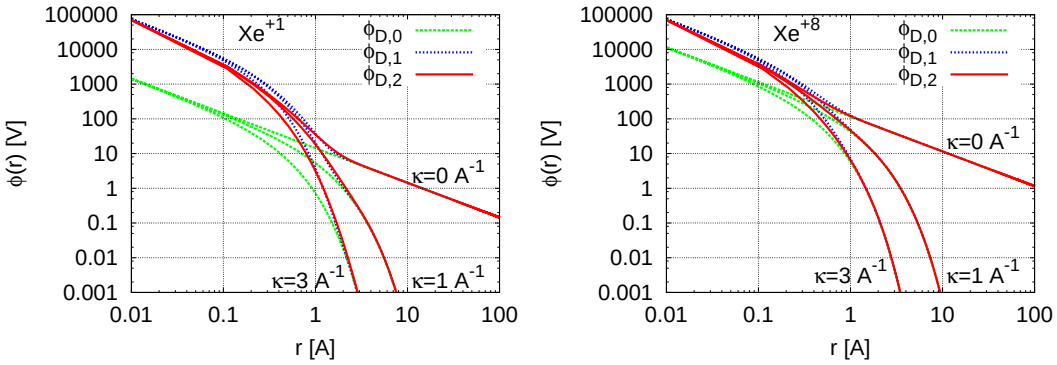

Figure 1.4: Screened effective atomic potentials of Xe ions within weakly coupled plasma. Potential, $\phi_{D,1}(r)$, from Eq. (1.7) and potential, $\phi_{D,2}(r)$, from Eq. (1.8) are plotted for Xe^{+1} ion (left), and Xe^{+8} ion (right) at three different values of $\kappa \equiv \lambda_D^{-1}$, $\kappa = 0, 1, 3$ Å^{-1}. The corresponding Debye screened point-like potentials, $\phi_{D,0}(r)$, are also plotted for comparison.

If the source density is spherically symmetric, the integral over the spherical angle can be performed. If the potential is investigated far away from the source, the dipole approximation can be applied in the expansion of the term, $e^{-\kappa|\mathbf{r}-\mathbf{r}'|}/\mid \mathbf{r}-\mathbf{r}' \mid$. Eq. (1.5) then reduces to:

$$\phi_D(r) = \frac{1}{4\pi\epsilon_0} \int dr'\, r'^2\, 4\pi\, e\rho(r') \left(\theta(r-r')\, \frac{e^{-\kappa r}}{r} + \theta(r'-r)\, \frac{e^{-\kappa r'}}{r'} \right), \tag{1.6}$$

where $\theta(r')$ is the step function. For the effective atomic potentials defined in the previous section, the weakly screened potential reads

$$\phi_{D,1}(r) = \frac{1}{4\pi\epsilon_0} \left(\frac{ie}{r}\, e^{-\kappa r} + \frac{(Z-i)e\alpha_i\kappa}{\kappa+\alpha_i}\, e^{-(\kappa+\alpha_i)r} + \frac{(Z-i)e}{r}\, e^{-(\kappa+\alpha_i)r} \right), \tag{1.7}$$

for $\Omega_1(r) = e^{-\alpha_i r}$, and:

$$\begin{aligned} \phi_{D,2}(r) = & \frac{1}{4\pi\epsilon_0} \left(\frac{ie}{r}\, e^{-\kappa r} + (Z-i)e \left(e^{-\kappa r} \left[\frac{\Omega_2(r)}{r} + \kappa\Omega_2(r) \right] \right.\right. \\ & \left.\left. -\kappa^2 \int_r^\infty dr'\, e^{-\kappa r'}\, \Omega_2(r') \right) \right), \end{aligned} \tag{1.8}$$

for $\Omega_2(r) = \left[\eta/\zeta(e^{\zeta r}-1)+1\right]^{-1}$. We note that in the limit, $\kappa \ll 1$ Å^{-1}, the second term, $(Z-i)e\alpha_i\kappa\, e^{-(\kappa+\alpha_i)r}/\kappa+\alpha_i$, in (1.7) can be neglected, and the potential, $\phi_{D,1}$, approaches the approximate screened potential used in [5]. These potentials are plotted in Fig. 1.4 for two Xe ionization states: Xe^{+1} and Xe^{+8}, at three different values of $\kappa = 0, 1, 3$ Å^{-1}. Despite the different parametrization of the density of bound electrons, the two screened effective potentials are close to each other. The largest discrepancy between the effective and the point-like potentials occurs at distances less or comparable with the atomic size. The asymptotic limits of all potentials are identical.

The results obtained so far depend on the assumption of weak coupling permitting the linearization of the Poisson equation. If any of the plasma species is strongly coupled, this

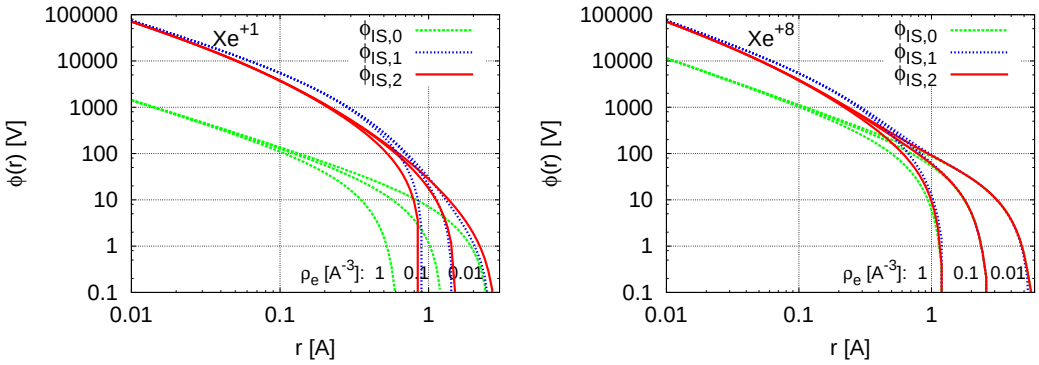

Figure 1.5: Screened effective atomic potentials of Xe ions within strongly coupled plasma. IS approximation is used to model the strong screening. Potential, $\phi_{IS,1}(r)$, and potential, $\phi_{IS,2}(r)$, from Eq. (1.10) are plotted for Xe^{+1} ion (left), and Xe^{+8} ion (right) at three different values of density of electrons within a cell ρ_e, $\rho_e = 0.01, 0.1, 1$ Å^{-3} (correspondingly $\rho_e = 10^{22}, 10^{23}, 10^{24}$ cm^{-3}). The IS screened point-like potentials, $\phi_0(r)$, are also plotted for comparison.

approximation is no longer valid and another approach should be applied. The potentials near the target ions can then be computed by putting each ion into a separate cell. The electrons are divided among the cells in order to provide net charge neutrality to each cell [31]. The electron density around the target ion can be approximated as uniform. The Poisson equation for each cell then reads

$$\nabla^2 \phi_{IS}(r) = -4\pi e\rho(r) + 4\pi e\rho_e, \tag{1.9}$$

where ρ_e is the uniform density of free electrons in this cell, and $\rho(r)$ is the ion density (1.2) that includes the density of bound electrons. This approximation is called the ion-sphere (IS) model.

The general solution of this equation is:

$$\phi_{IS}(r) = \theta(R-r)\left(\phi(r) - 4\pi e\rho_e\left[\frac{R^2}{2} - \frac{r^2}{6}\right]\frac{1}{4\pi\epsilon_0}\right) \tag{1.10}$$

where $\phi(r)$ is the unscreened atomic potential. The radius of IS cell, R, is estimated from the neutrality condition at the cell edge, $\phi_{IS}(R) = 0$. For a point-like ion, the cell size is $R = ((3i)/(4\pi\rho_e))^{1/3}$. For the effective potentials R also depends on the parameters of the unscreened potentials, i. e. α_i, ζ, η. There is no simple analytical solution of the neutrality condition in this case. The radius of a cell can then be either estimated with the asymptotic conditions of this equation at $r = 0$ and $r = \infty$, or evaluated numerically. In Fig. 1.5 we plot the screened effective potentials within strongly coupled plasma at three different values of the density of free electrons, $\rho_e = 0.01, 0.1, 1$ Å^{-3}, within a cell for Xe^{+1} and Xe^{+8} ions. As in case of weak coupling, the screened effective potentials are close to each other. At $r < 1$ Å the largest discrepancy between the effective and the point-like potentials occurs. However, the application of the effective potentials extends the size of the cell, when compared to the

case with point-like ions. This effect is more pronounced for Xe^{+1} ion, and less for highly charged Xe^{+8} ion, when the contribution of the point-like term in the effective potentials dominates, and sizes of cells are nearly identical for all potentials considered.

Cross sections for elastic electron-ion scattering within plasma

The quantum mechanical cross section for the elastic scattering of an electron on a central potential in first Born approximation is obtained from the corresponding scattering amplitude, that is proportional to the Fourier transform of the scattering potential [25]:

$$\widetilde{\phi}(\Delta k) = \frac{-1}{\Delta k} \int_0^\infty dr\, r\, sin(\Delta k \cdot r)\, \phi(r). \tag{1.11}$$

where $\mathbf{\Delta k} = \mathbf{k_i} - \mathbf{k_f}$ is the wave vector transfer, k_i, k_f are the wave vectors of the electron before and after the collision. The differential cross section then reads

$$\frac{d\sigma_{el,B}}{d\Omega} = \mid \widetilde{\phi}(\Delta k) \mid^2 \left(\frac{2m}{\hbar^2}\right)^2, \tag{1.12}$$

where m is electron mass. For the screened effective potentials as defined in the previous section, the scattering amplitudes in first Born approximation are calculated as

$$\widetilde{\phi}_{D,1}(\Delta k) = -\frac{1}{4\pi\epsilon_0}\left[\frac{ie}{(\Delta k)^2+\kappa^2} + 2\,\frac{(Z-i)e\alpha\kappa}{((\Delta k)^2+(\kappa+\alpha)^2)^2} + \frac{(Z-i)e}{(\Delta k)^2+(\kappa+\alpha)^2}\right] \tag{1.13}$$

$$\begin{aligned}\widetilde{\phi}_{D,2}(\Delta k) = &-\frac{1}{4\pi\epsilon_0}\left[\frac{ie}{(\Delta k)^2+\kappa^2} + \frac{(Z-i)e}{\Delta k}\int_0^\infty dr\, sin(\Delta k\cdot r)\, e^{-\kappa r}\,\Omega_2(r)\right.\\ &+ \frac{(Z-i)e\kappa}{\Delta k}\int_0^\infty dr\, r\, sin(\Delta k\cdot r)\, e^{-\kappa r}\,\Omega_2(r)\\ &\left.- \frac{(Z-i)e\kappa^2}{\Delta k}\int_0^\infty dr\,\left(\frac{sin(\Delta k\cdot r)}{(\Delta k)^2} - \frac{r\, cos(\Delta k\cdot r)}{\Delta k}\right) e^{-\kappa r}\,\Omega_2(r)\right]\end{aligned} \tag{1.14}$$

for the weak coupling case, and

$$\begin{aligned}\widetilde{\phi}_{IS,l}(\Delta k) = &-\frac{1}{4\pi\epsilon_0}\left[\frac{ie}{(\Delta k)^2}\,[1-cos(\Delta k\cdot R)] + \frac{(Z-i)e}{\Delta k}\int_0^R dr\, sin(\Delta k\cdot r)\,\Omega_l(r)\right.\\ &\left.- (4\pi e\rho_e)\left(-\frac{R^3}{3}\,\frac{cos(\Delta k\cdot R)}{\Delta k^2} + \frac{sin(\Delta k\cdot R)}{(\Delta k)^5} - \frac{R\, cos(\Delta k\cdot R)}{(\Delta k)^4}\right)\right]\end{aligned} \tag{1.15}$$

for the strong coupling case, where indices $l = 1, 2$ refer to the potential from [5] and [30], respectively. Below we summarize our results on the elastic cross sections obtained for Xe^{+1} and Xe^{+8} (plots not shown). The cross sections calculated with effective ion potentials in the weak coupling regime change extensively with the parameter κ: they decrease with increasing κ. For comparison, at $\Delta k = 0.1$ Å^{-1} the ratio of the cross sections, $R_D \equiv (d\sigma(\kappa=0)/d\Omega)/(d\sigma(\kappa=10)/d\Omega)$ is $R_D \sim 10^5$ for Xe^{+1} and $R_D \sim 10^7$ for Xe^{+8}. In contrast, the cross sections in the strong coupling approach change less at the considered electron densities, $\rho_e = 0.01 - 1$ Å^{-3}. They decrease with the increasing density, and

$R_{IS} \equiv (d\sigma(\rho_e = 0.01)/d\Omega)/(d\sigma(\rho_e = 1)/d\Omega)$ is $R_{IS} \sim 5$ for Xe^{+1}, and $R_{IS} \sim 10^2$ for Xe^{+8}, also at $\Delta k = 0.1$ Å^{-1}.

For point-like ions the impact of both weak and strong screening effect on the elastic cross sections is much larger: (i) for both Xe^{+1} and Xe^{+8} ions, $R_D = 10^8$, in the weak coupling regime, and (ii) $R_{IS} = 40$ for both Xe^{+1} and Xe^{+8} ions in the strong coupling regime.

Cross sections for stimulated photoemission and photoabsorption

If an electron scatters on an ion in the presence of an external laser field, absorption or emission of radiation quanta may occur. The quantum mechanical cross section for this process was derived by Kroll and Watson in [12]. It sums the individual cross sections for the exchange of n radiation photons:

$$\left(\frac{d\sigma}{d\Omega'}\right)_{IB} = \sum_{n=-\infty, n\neq 0}^{\infty} \frac{d\sigma_n}{d\Omega'} = \sum_{n=-\infty, n\neq 0}^{\infty} \frac{v_0'}{v_0}\, J_n^2(s\,\Delta v\, cos(\Theta_{\Delta v,\epsilon}))\, \frac{d\sigma_{el,B}}{d\Omega'}(\Delta v)\,, \quad (1.16)$$

where v_0 denotes time averaged velocity of the incoming electron, v_0' denotes velocity of the outcoming electron and Δv is the magnitude of the velocity transfer, $\Delta v = |\mathbf{\Delta v}|$. The kinetic energies of the incoming, E_0, and the outcoming electron, E_0', fulfill the relation: $E_0' = E_0 + n\,\hbar\omega$, where $\hbar\omega$ is the photon energy, and n denotes the number of emitted/absorbed photons. The field strength parameter, s, is defined as $s = e\mathbf{E}_0/\hbar\omega^2$. The angle $\Theta_{\Delta v,\epsilon}$ measures the angle between the vector, $\mathbf{\Delta v}$, and the vector of the field polarization, $\boldsymbol{\epsilon}$.

Equation (1.16) holds whenever the Born approximation provides an accurate description of the elastic process, in which case the elastic cross section depends on the velocity transfer only [12]. We note here that the velocity transfer in this case is due not only to the change of electron momentum but also to the change of the velocity magnitude after emission or absorption of radiation photons. Asymptotics of the Bessel function, J_n, implies that at small values of argument, $s\,\Delta v \ll 1$ (low field and/or slow electrons) single photon exchanges dominate. At high values of $s\,\Delta v \gg 1$, the envelope of Bessel function behaves like $(s\,\Delta v)^{-1/2}$. This yields the classical limit of the stimulated absorption and emission cross section (the impact model) [11].

We integrate Eq. (1.16) over the scattering angle and average over the direction of the field polarization, $\boldsymbol{\epsilon}$:

$$\langle\sigma\rangle_{IB} = \frac{1}{4\pi} \int d\Omega_\epsilon\, d\Omega'\, \frac{d\sigma}{d\Omega'}. \quad (1.17)$$

Below we plot the averaged total cross section for stimulated photoemission and photoabsorption as a function of the kinetic energy of the incoming electron for the various parametrizations of the atomic potentials of Xe^{+1} and Xe^{+8} ions (Fig. 1.6). The value of the field strength parameter, s, was chosen to match the experimental conditions during

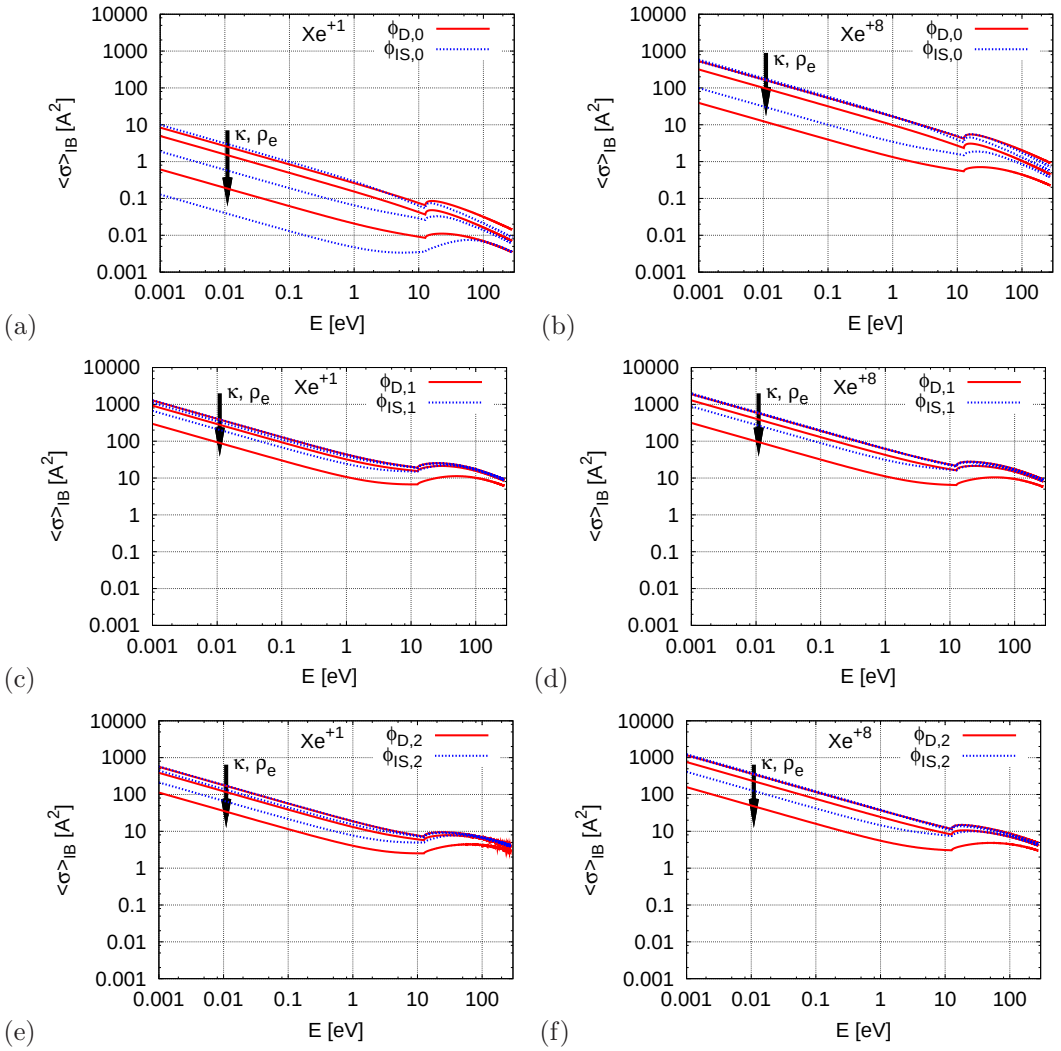

Figure 1.6: Averaged cross sections for stimulated photoemission and photoabsorption obtained for various atomic potentials: (a),(b) point-like Coulomb potential, (c),(d) effective atomic potential from [5], (e),(f) effective atomic potential from [30], at the fixed value of field strength parameter, $s = 0.01$ fs/Å. Results for Xe^{+1} ions (left) and Xe^{+8} ions (right) were obtained at three different values of $\kappa = 0, 1, 3$ Å^{-1} (weak screening case) and $\rho_e = 0.01, 0.1, 1$ Å^{-3} (strong screening case) and are plotted as function of the kinetic energy of the incoming electron. Arrows show how the cross sections change with the increasing values of κ and ρ_e.

the first cluster experiment, $s = 0.01$ fs/Å at $I \leq 10^{14}$ W cm^{-2} and at the photon energy, $E_\gamma = 12.7$ eV.

For both parametrizations of the effective atomic potentials we obtain similar values of the total IB cross sections, $\langle\sigma\rangle_{IB}$. These values are much higher than the corresponding ones obtained for the point-like potential, i.e. about 140 times larger for Xe^{+1} ions and four times larger for Xe^{+8} ions. The discrepancy of the cross sections is smaller in case of highly charged ion, as the contribution of the point-like term to the effective potentials Eqs. (1.13), (1.14), (1.15) is then much larger than in case of singly charged ions. A significant increase of the cross sections estimated with effective potentials in respect to the cross section estimated with point like potentials has been first observed in [5, 26], and has lead to the hypothesis of the enhanced plasma heating.

As next we characterize how the plasma environment affects the total IB cross section. As our results should estimate these cross sections within a changing plasma environment, e. g. in case of transition from the strongly coupled to the weakly coupled plasma regime, we again consider a broad range of plasma parameters: (i) $\kappa = 0, 1, 3$ Å^{-1} in weakly coupled regime, (ii) $\rho_e = 0.01, 0.1, 1$ Å^{-3} ($\rho_e = 10^{22}, 10^{23}, 10^{24}$ cm^{-3}).

For point-like potentials the total cross sections are strongly affected by the plasma environment. At the considered plasma parameters the ratio of the maximal and the minimal cross sections, $R \equiv \sigma_{max}/\sigma_{min}$, is $R \leq 75$ for Xe^{+1} ion and $R \leq 14$ for Xe^{+8} ion. The corresponding ratios, estimated using the effective potentials, are: (i) $R \leq 4$ for Xe^{+1} and $R \leq 6$ for Xe^{+8} with the parametrization from [5], and (ii) $R \leq 5$ for Xe^{+1} and $R \leq 7$ for Xe^{+8} with the parametrization from [30]. The maximal expected change of the cross sections obtained using effective potentials can then be estimated with a factor of seven.

Summary

To sum up, we have calculated the total cross section for stimulated photoabsorption and photoemission using point-like and effective atomic potentials within an evolving plasma. The effect of a possible transition from the strongly coupled to the weakly coupled regime on the cross section was evaluated.

The application of the effective atomic potentials increased significantly the total IB cross sections by a factor of 140 for Xe^{+1} ions and by a factor 4 for Xe^{+8} ions in respect to the corresponding cross sections calculated with point-like potentials. Similar effect was observed in [5, 6].

The total cross sections for photoemissions and absorptions obtained with effective atomic potentials can change by a factor of seven at most for plasma parameters in the range: $\kappa = 0 - 3$ Å^{-1} and $\rho_e = 0.01 - 1$Å^{-3}, and at a fixed value of the field strength parameter, $s = 0.01$ fs/Å. This range of the plasma parameters correspond to that one expected for plasmas created during the interaction of intense VUV radiation from a FEL with xenon

clusters [3]. In contrast, for point-like ions the maximal change of the cross sections is much larger and may be of the order of 75.

Our results show that the inverse bremsstrahlung cross sections estimated with effective atomic potentials are not much affected by the changing plasma environment. This observation validates the estimate of the enhanced plasma heating effect from [5, 6] that may explain the high energy absorption within clusters irradiated with intense VUV radiation.

1.4 Multi-electron-recombination rates estimated within dense plasma[3]

Abstract

We investigate the rates for multielectron recombination within a dense plasma with Maxwellian electron energy distribution function. We find that these rates can be high within dense plasmas, and they should be treated in the simulations of the plasmas created by intense radiation, in particular for plasmas created by intense VUV radiation from free-electron-laser (FEL), or for modeling the inertial confinement fusion (ICF) plasmas.

Introduction

Electronic many-body recombination processes that occur within dense, cold plasmas have attracted much attention recently as a possible explanation of the strong energy absorption within laser-created plasmas [9, 24]. During the first cluster experiment performed at the free-electron-laser FLASH facility at DESY [3, 4] such plasmas were created after the irradiation of the xenon clusters with VUV photons of energy, $E_\gamma = 12.7$ eV. Pulse duration did not exceed 50 fs, and the maximal pulse intensity was, $I \leq 10^{14}$ W/cm^2 . Highly charged Xe ions (up to +8) of high kinetic energies were detected, indicating a strong energy absorption that could not be explained using the standard approaches [22, 4, 21]. More specifically, the energy absorbed was almost an order of magnitude larger than that one predicted with classical absorption models, and the ion charge states were much higher than those observed during the irradiation of isolated atoms at the similar conditions. This indicated that at these radiation wavelengths some processes specific to many-body systems were responsible for the enhanced energy absorption.

The lowest order many-body recombination is three-body recombination, where two continuum electrons are involved initially, and in the final state one of these electrons is captured by the target ion. The excess energy released by the recombining electron is then carried away by the other outgoing electron, therefore the three-body recombination does not involve any emission of photons [32]. For this to happen it is necessary that the electron density must be high enough so that the collisional processes are more probable than the dissipative radiation processes [33]. The three-body recombination is the inverse of the electron collisional ionization, and this relation is used in deriving the relevant cross-section formula, by detailed balance.

In the similar way higher-order recombination processes can be described. More than two electrons are then involved. Rates for these processes strongly depend on the electron density, and can again be calculated with the rates of the corresponding inverse many-body collisional processes.

[3]This section has been published as *Paper II*: B. Ziaja, F. Wang and E. Weckert, High Energy Density Physics **5** 221–224 (2009).

The mechanism of plasma heating due to many-body recombination that was proposed in Ref. [9] in order to explain the experimental results of Ref. [3] can be best described as a sequence of Auger processes followed by photoionization. According to [9], the strongly coupled nanoplasma is created shortly after the exposure. Within this plasma, a probability of finding two or more electrons being close to an ion is relatively high. One electron can be captured by the ion, while the other electrons (spectators) carry away the excess energy released by the recombining electron. The captured electron may then absorb a radiation photon and become ionized once more. This cycle repeats many times during the duration of the pulse, leading to an efficient heating of the electron cloud. Ions of charge up to +7 were predicted with this model for the Xe_{1000} cluster.

Here we aim to study a different many body recombination process that may also occur within dense plasmas. This is multielectron recombination (MER) that is an inverse process to multiple collisional ionization. Several electrons then recombine simultaneously, and a single spectator electron carries away the excess energy. We will evaluate the significance of this process within plasmas created by VUV FEL radiation from xenon and argon clusters [3] and also within ICF plasmas [34]. We will first derive analytical formulas for MER cross-section and rates, using the microscopic reciprocity relation and the detailed balance principle [35]. Using these formulas, we will obtain numerically the MER rates for Xe and Ar plasmas. These rates will give an estimate, how significantly these processes may contribute to the ionization dynamics within dense plasmas.

Calculation of rates for multielectron recombination

MER is an inverse of themultiple collisional process (Fig. 1.7), where the primary electron ionizes an atom, releasing one or more secondary electrons. At $n = 1$ we arrive at the three-body recombination (one-electron recombination), at $n = k$ we have k-electron recombination. Inwhat followswe will use the notation as in Ref. [35].

Derivation of the MER cross sections and rates bases on the validity of the quantum mechanical reciprocity relation:

$$w(i \to f) = w(f \to i), \tag{1.18}$$

where $w(i \to f)$ is the transition probability per unit time for the transition $|i > \to |f >$ between single quantum states of the states i and f. Reciprocity relation (1.18) is an essential condition for the validity of the principle of detailed balance [35]. The conditions for validity of the reciprocity relation can be obtained within the framework of the general scattering matrix theory [35]. The result is that the reciprocity relation $w(i \to f)$ is not generally valid, not even if the Hamiltonian of the system is invariant under space reflection (P) and time reversal (T). However, relation (1.18) holds in the framework of perturbation theory, and thus applies to radiative processes and to collisions in the Born approximation. The reciprocity relation holds moreover for all collision processes involving unpolarized particles, provided that the Hamiltonian is P- and T-invariant. In what follows we will consider

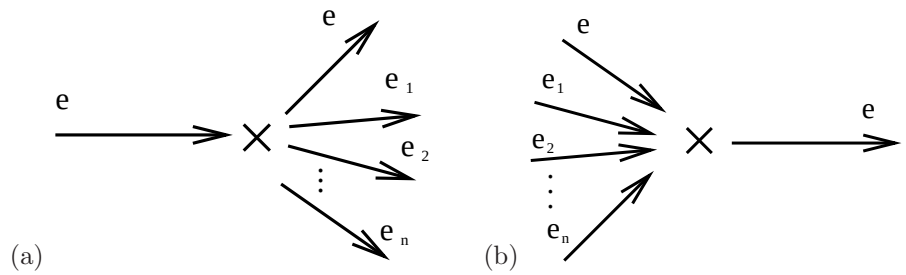

Figure 1.7: Collisional processes within a dense plasma: (a) multiple collisional ionization and (b) its inverse process: multielectron recombination. The electron, e, is a spectator.

only unpolarized particles, therefore the reciprocity relation will be valid for the processes considered.

Explicit form of the reciprocity relation for specific processes can be derived directly from quantum mechanics. Here, following Ref. [35], we will derive it through the principle of detailed balance, by writing down the rate equations and using the explicit form of the thermal distribution functions. This procedure is simple and straightforward, while the relations so found are independent of this method, and are identical with those derived directly from quantum mechanics. We will assume the electron distributions to be isotropic.

Balanced reaction equation for a collisional process (k-body multiple ionization) and its inverse process (k-body multielectron recombination) in Fig. 1.7 can be written as:

$$A(E_0) + e(E) \rightleftharpoons A^+(E_+) + e(E') + e(E_1) + \ldots + e(E_k), \tag{1.19}$$

where A denotes atom or ion in the state of initial energy E_0 , A^+ denotes the ionized atom or ion in the state of energy E^+, e is electron of energy $E(E_i)$. Energy of the spectator electron changes from $E \rightleftharpoons E'$ during the process. This reaction leads to the balanced rate equation:

$$\begin{aligned}
&\rho_0 \sqrt{\frac{2E}{m_e}}\, \rho_e\, f_e(E)\, \Omega_{0+}(E; E', E_1, \ldots, E_k) dE' dE_1 \ldots dE_k \\
&\quad = \rho_+ \sqrt{\frac{2E'}{m_e}}\, \rho_e\, f_e(E')\, dE' \sqrt{\frac{2E_1}{m_e}}\, \rho_e\, f_e(E_1)\, dE_1 \ldots \sqrt{\frac{2E_n}{m_e}}\, \rho_e\, f_e(E_k)\, dE_k \\
&\qquad \Omega_{+0}(E', E_1, \ldots, E_k; E)\, dE,
\end{aligned} \tag{1.20}$$

where we introduced the following notation: ρ_0 denotes density of atoms/ions in initial energy state E_0, ρ_+ denotes density of atoms/ions in the final energy state E_+, ρ_e is the electron density and m_e is the electron mass. The distribution, $f_e(E)$, is a normalized isotropic Maxwell-Boltzmann distribution of electron kinetic energy, and quantities $\Omega_{0+}(E; E', E_1, \ldots, E_n)$ and $\Omega_{+0}(E', E_1, \ldots, E_n; E)$ are differential cross sections (in respect to energy) for the multiple collisional ionization and multielectron recombination respectively. The angular distribution of electrons was assumed to be isotropic, and the integration over scattering angles was performed.

The rate for multielectron recombination is defined as:

$$R_{k(RC)} = \rho_e^{k+1} \int \sqrt{\frac{2E'}{m_e}}\sqrt{\frac{2E_1}{m_e}} \cdots \sqrt{\frac{2E_k}{m_e}} f_e(E')\, f_e(E_1) \ldots\, f_e(E_k) \\ \Omega_{+0}(E', E_1, \ldots, E_k; E) dE'\, dE_1\, \ldots\, dE_k\, dE, \tag{1.21}$$

and can be related to the collisional multiionization rate:

$$R_{k(I)} = \rho_e \int \sqrt{\frac{2E}{m_e}}\, f_e(E)\, \Omega_{0+}(E; E', E_1, \ldots, E_k)\, dE'\, dE_1\, \ldots\, dE_k\, dE, \tag{1.22}$$

through a relation that follows from Eq. (1.20):

$$\rho_+\, R_{k(RC)} = \rho_0\, R_{k(I)}. \tag{1.23}$$

In a balanced state the relation between the atom/ion distributions in states E_0 and E_+ is given by a Saha relation [35]. For k-multielectron recombination and k-multiple ionization this relation can be derived (not shown here) from Eq. (1.19) as:

$$\frac{\rho_0}{\rho_+} = \frac{g_0}{g_+}\, e^{\beta\, E_{+0}} \left(\frac{1}{2}\rho_e\, \lambda_e^3\right)^k, \tag{1.24}$$

where $\beta = 1/k_{_B}T$ is the inverse of the temperature within the system and $\lambda_e = \frac{h}{\sqrt{2\pi m_e k_{_B} T}}$ is the thermal de Broglie wavelength of free electrons. Coefficients, g_0, g_+, are statistical weights of the bound energy levels, E_0, E_+, respectively, and $E_{+0} = E_+ - E_0$ is the energy needed for transition from state E_0 to state E_+ (ionization energy). After substituting Eq. (1.24) to Eq. (1.23), we obtain:

$$R_{k(RC)} = R_{k(I)}\, \frac{g_0}{g_+}\, e^{\beta\, E_{+0}} \left(\frac{1}{2}\rho_e\, \lambda_e^3\right)^k. \tag{1.25}$$

From Eq. (1.20) also a microscopic relation between ionization and recombination cross sections can be obtained:

$$g_0\, E\, \Omega_{0+}(E; E', E_1, \ldots, E_k) = g_+ \frac{2^{4k}}{h^{3k}}\, (\pi\, m_e)^k\, E'\, E_1\, \ldots\, E_k\, \Omega_{+0}(E', E_1, \ldots, E_k; E). \tag{1.26}$$

This is a generalization of the Fowler relation obtained for three-body recombination [35, 36]. As expected, at $k = 1$ Eq. (1.26) reduces to the Fowler relation:

$$g_0\, E\, \Omega_{0+}(E; E', E_1) = g_+ \frac{2^4}{h^3}\, (\pi\, m_e)\, E'\, E_1\, \Omega_{+0}(E', E_1; E). \tag{1.27}$$

For non-Maxwellian plasmas (i.e. with non-Maxwellian electron energy distribution function) Eq. (1.25) is not longer valid. The non-equilibrium rate for multielectron recombination can then be still obtained from Eq. (1.21), using the recombination cross section derived from the microscopic relation, Eq. (1.26), and convoluted with non-equilibrium electron distributions. The difficulty lies in the correct parametrization of the differential multiple ionization cross section, which is not known for an arbitrary value of $n > 1$ [37, 38, 39]. Therefore we restrict here to Maxwellian plasmas, for which the direct rate equation, Eq. (1.25), can be used.

Estimation of multielectron recombination rates for xenon and argon

We used Eq. (1.25) to estimate the rate for multielectron recombination within Maxwellian plasmas. In order to calculate the collisional ionization rate, we used experimentally determined total cross sections for collisional multiionization from ground state from Ref. [40]. The limitations of data compilations are discussed in detail in [40]. From the data listed in [40] we estimated the maximal relative experimental uncertainties of the cross sections. They were: 9% for Ar→Ar^{+2} transition, 20% for Ar→Ar^{+3} transition and 11% for Ar→Ar^{+4} transition. For Xe correspondingly: 12% for Xe→Xe^{+2} transition, 14% for Xe→Xe^{+3} transition. For Xe→Xe^{+4} transition there were no estimates of the experimental errors given.

Eq. (1.25) implies that the electrons recombine in most cases to the higher Rydberg states, for which the statistical weights, g_0, are large. Therefore here we estimate the recombination rates to an "average" Rydberg state. However, due to the depression of ionization potential (IP) within a plasma, the number of available states above the ground level strongly decreases with the increasing electron density. Therefore, the recombination to the lower states becomes more probable. Using the rough estimate of a hybrid model from Ref. [31] to estimate the IP depression, we found that the ground state level approaches continuum for Ar plasma at densities $6 \cdot 10^{23}$ cm^{-3} to $3 \cdot 10^{24}$ cm^{-3} for the considered temperatures, 1-100 eV. For Xe plasma the corresponding density range is 10^{23} cm^{-3} to 10^{24} cm^{-3}. Therefore in our calculations we limit the densities to 10^{24} cm^{-3}, and restrict to the ground state excitations/recombinations. Further, we do not take the IP depression effect into account. The reason is that we know only experimental cross sections for multiple ionizations from the ground states. And we aim at making our predictions possibly independent of theoretical modeling that may lead to strongly differing predictions (e.g. estimates of IP depression from NLTE-4 Database [41]). Within the scheme proposed, our results will then constitute the lower limit estimate for the true MER rates.

The recombination rates obtained are plotted in Fig. 1.8. Density range, $\rho = 10^{22} - 10^{24}$ cm^{-3} at temperatures $T = 1 - 10$ eV corresponds to plasmas created by intense VUV laser pulse from FEL [28, 29, 42, 43]. The rates obtained for densities $\rho = 10^{22} - 10^{25}$ cm^{-3} and temperatures $T \sim 100$ eV are relevant for IFC plasmas.

At the density, $\rho = 10^{23}$ cm^{-3}, and temperatures, $T = 1 - 10$ eV, the highest rates are: the rate for 3-electron recombination (Xe), and 2-electron recombination (Ar). This tendency keeps with increasing electron density. The absolute values of recombination rates ($n = 1 - 3$) at $\rho = 10^{23}$ cm^{-3} are then between $10^{-1} - 10^{2}$ 1/fs for Xe and $10^{-3} - 10^{2}$ 1/fs for Ar, depending on the temperature.

In the region of high densities, $\rho > 10^{24}$ cm^{-3}, and at high temperatures, $T = 100$ eV, relevant for ICF plasmas, the absolute recombination rates are high: $10^{3} - 10^{4}$ 1/fs for Xe, and $10^{1} - 10^{2}$ 1/fs for Ar at $\rho = 10^{25}$ cm^{-3}. The 1-electron recombination is predominant but the other recombination rates ($n = 2, 3$) are less by the factor of 10-1000 for both Xe and Ar.

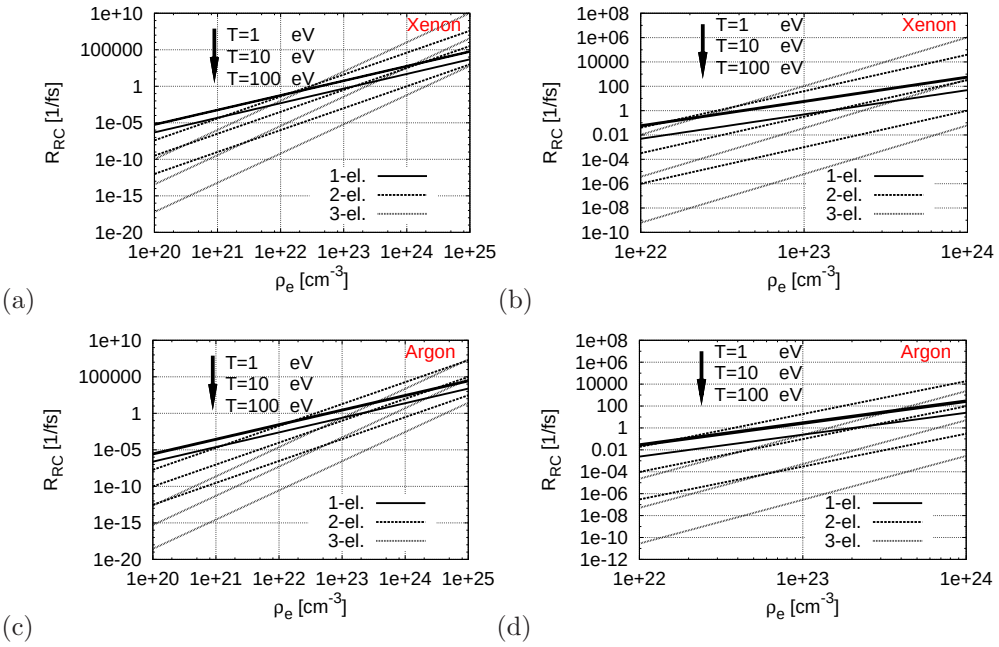

Figure 1.8: Rates for multielectron recombination: 1, 2, 3-electron recombination to ground state as functions of plasma density for a Maxwellian plasma. The results were obtained for: (a) xenon with (b) closeup, and (c) argon with (d) closeup. Arrows show how the rates change with the increasing values of electron temperature, $T = 1, 10, 100$ eV. Curves for $n = 1$ at $T = 1 - 10$ eV are very close to each other.

Discussion and summary

The aim of our study was to estimate the contribution of the multielectron recombination rates ($n > 1$) to the ionization dynamics within dense plasmas.

We derived the MER recombination rates for Maxwellian plasmas built of xenon or argon atoms and ions, using the experimentally determined cross sections for multiple collisional ionization of atoms from their ground state. The maximal experimental uncertainty of the cross section was not exceeding 20%. Correspondingly, we considered the MER recombination to the ground state only. Plasma effects as IP depression, modifications of the cross sections due to the charged many-body environment have not been treated. Rough estimates have shown that the effect of IP depression may be strong at the densities larger than 10^{23} cm^{-3}. The higher Rydberg states then disappear. Therefore our predictions that give the lower limit of the true MER values may closer approach the true values at the increasing plasma density.

We showed that in the $\rho - T$ region relevant for plasmas created after irradiation of Xe and Ar clusters with intense VUV pulses from FEL, MER recombination dominates over the 1-electron recombination. The values of recombination rates ($n = 1 - 3$) are between 10^{-1} to 10^{2} 1/fs for Xe and 10^{-3} to 10^{2} 1/fs for Ar at $\rho = 10^{23}$ cm^{-3}, depending on the temperature, $1 - 10$ eV. In the $\rho - T$ region of ICF plasmas, at $\rho = 10^{24}$ cm^{-3} the 1-electron recombination dominates but the 2- and 3-electron recombination rates are less by factor of 10-1000.

After writing up this paper we became aware of the Ref. [39], where the MER recombination processes have also been treated. Four-body recombination rate, corresponding to 2-electron MER recombination, was calculated there for Ar, using the similar detailed balance treatment as in [35]. In contrast to our treatment, the empirical fits were used for the parametrization of the total ionization cross sections from ground state. The effect of IP depression was not taken into account. The obtained recombination rates together with the double-ionization rate coefficients were included in the plasma kinetics code. Predictions for Maxwellian and non-Maxwellian plasmas were obtained. It was found that the inclusion of the MER effects influenced the average ionization stage of the plasma at electron densities $> 10^{22}$ cm^{-3}. This agrees well with the observations from our model. However, the predictions for non-Maxwellian plasmas obtained in [39] strongly depended on the parametrization of the differential cross section used.

The results from Ref. [39] and our results that estimate the lower limit of the MER rates indicate that the MER rates should be treated in the simulations of processes occurring within ICF plasmas and FEL laser created plasmas. The quantitative validation, how significantly the MER processes contribute to the plasma dynamics requires a dedicated rate equation approach [39], where both competing processes: non-sequential ionization and MER recombination are included. We emphasize also the strong need for the more sophisticated calculations beyond the framework of the simple quantum-mechanical model [35]. In particular, recombination to higher Rydberg states should be treated, taking into ac-

count the effect of IP depression, and the modification of collisional cross sections due to the charged plasma environment. We note, however, that the estimates of IP depression obtained from different models may differ significantly [41], and this will make the predictions obtained model-dependent. Also, possible strong coupling and degeneracy effects for non-ideal and non-classical plasma regime should be included in the analysis. This advanced approach is, however, beyond the scope of the present study.

1.5 Molecular Dynamics model

In this model, both ions and electrons are treated as point charges. The classical Coulomb evolution of this charge system is simulated by molecular dynamics (MD), which is a numerical integration of particle motions over time in phase space. The standard MD algorithm is presented in Appendix A. In this model, there are two kinds of interactions: (i) potential interactions between charged particles; (ii) fast collisions such as photoionization. The former is embedded in MD integration, while the latter is realized by Monte Carlo events in a single MD simulation step.

The structure of the atom is important in the interaction between atoms and electrons, especially in the inverse bremsstrahlung process with a laser field involved. When a free electron approaches close to an atom (or ion), the shells of binding electrons in the atom cannot perfectly screen the positively-charged nucleus inside the atom. The free electron can therefore experience a partial potential from the nuclear charge. Hence, the atomic structure that the electron experiences could be simply modeled as a centrosymmetric potential [5]:

$$\phi(r,q) = -\frac{e}{4\pi\varepsilon_0}\left(\frac{q}{r} + \frac{Z-q}{r}e^{-\alpha_q r}\right), \tag{1.28}$$

where Z is the nuclear charge of the atom, q is charge of the atom, and α_q is a model parameter which is determined by matching the experimental ionization energy of a q-charged ion. The potential approaches a Coulomb potential when the electron is far away from the atom ($r \to \infty$).

When a quasi-free electron stays in an atomic cluster, the electron experiences potential not only from the atom closest to it, but also from the other background atoms. The other moving electrons in the cluster, like plasma electrons, may screen potentials from background atoms to this electron. The screening effect is determined by the Debye length,

$$\lambda_D = \sqrt{\frac{\varepsilon_0 k T_e}{e^2 n_e}}, \tag{1.29}$$

with T_e being the electron temperature and n_e the electron density in the cluster. In following MD simulations, the Debye length is comparable to the atomic size and lies in regime of weakly coupled plasma. The contribution of the screening effect can be approximated as an exponential factor applied to the effective potential (see Eq. 1.7):

$$\phi'(r,q) = \phi(r,q)e^{-r/\lambda_D}. \tag{1.30}$$

The atomic potential with plasma screening effect is used for calculations of the quantum mechanical cross sections of the inverse bremsstrahlung in § 1.3. The realization of the inverse bremsstrahlung process will be presented later.

The classical motions of particles in the model naturally account for the Debye screening effect when all background potentials described by Eq. (1.28) are taken into account. However, the attractive potential in Eq. (1.28) has an infinite depth at $r = 0$, which may cause

an integral problem of singularity in numerical simulations. The potential can be smeared to remove the singularity:

$$\phi(r,q) = -\frac{e}{4\pi\varepsilon_0}\frac{q}{r}\left(1-e^{-\alpha r}\right)\ , \text{ with } \lim_{r\to 0}\phi(r,q) = -\frac{e}{4\pi\varepsilon_0}q\alpha\,, \tag{1.31}$$

where the parameter α is of the same order as α_q. The lost inner atomic structure is not important for classical motion of electrons, because: (i) the structure-sensitive collisions, such as the inverse bremsstrahlung, have been treated separately; (ii) the separated elastic collisions are considered through corresponding experimental cross sections. The repulsive interaction between charged ions or electrons at large distances are described by the standard Coulomb potential.

The other interactions are realized through Monte Carlo events. There are five types of interaction events involved, as mentioned in § 1.2:

- *Photoionization* (PI), sequential ionization by photons;
- *Inverse bremsstrahlung* (IB), with atomic potential and plasma screening effect considered;
- *Collisional ionization* (CI), sequential ionization by impact electrons;
- *Three-body recombination* (RC), the inverse process to CI;
- *Elastic collision* (EL), between atoms (or ions) and electrons.

Each type of Monte Carlo event is assigned a chance to occur determined by the interaction cross sections. The occurring time of an event or appearance of an event in each MD time step are randomly chosen. The MD model integrated with Monte Carlo events enables treatment of probabilistic processes or collisions in the irradiated clusters.

The photoionization probability of a single atom or ion is described by an exponential decay function of exposure time t [44]:

$$P_{PI}(t) = e^{-t/\tau_{PI}}\ , \tag{1.32}$$

with the life time $\tau_{PI} = \hbar\omega/\sigma_{PI}I$. The cross section σ_{PI} is the total PI cross section for a single atom, and I is the laser intensity. The sum of photoionization cross sections from all single atoms in a cluster is estimated to be only several percent of the cluster's transverse section[4]. The ionization probability is assumed to be uniform for all atoms in the cluster. A Monte Carlo event of photoionization occurs at a randomly-chosen time:

$$t = -\tau_{PI}\cdot\ln R\,, \tag{1.33}$$

[4]This assumption is valid for the cluster sizes considered in this work (the numbers of atoms are less than 1000, and relevant PI cross sections see Appendix B). For a cluster of larger sizes at the same density, the total PI cross section might be comparable to its transverse section. In other words, the light may not penetrate through a much thicker cluster, as discussed in the next chapter.

with R a uniform random number in range $(0, 1)$, following the probability distribution in Eq. (1.32).

The next four types of interactions occur during the collisions between electrons and atoms (ions). Electrons are assumed to travel "freely" in potential background between two successive collision events for each electron. This is statistically described by the *mean free path* (MFP) of an electron:

$$L_e = \frac{1}{\rho \cdot \sigma}\,, \tag{1.34}$$

with ρ being the atom (ion) density and σ the collisional cross section. According to Beer's law, the probability of an electron "free" moving in a cluster is:

$$P_e(t) = e^{-x/L_e}\,, \tag{1.35}$$

with x being a traveling distance. The randomly-chosen distance x between two successive collision events can be realized in the same way as Eq. (1.33). The collisional cross section in the cluster is then the total cross section summed over all four types of collisions:

$$\sigma_{tot} = \sigma_{IB} + \sigma_{CI} + \sigma_{RC} + \sigma_{EL}\,. \tag{1.36}$$

The collision event is randomly chosen among these types. The chance of each type of event is proportional to the respective cross section, i.e. σ/σ_{tot}.

Proper estimation of the MFP is critical for a meaningful realization of the Monte Carlo events. In this model, electron temperature in the cluster and average charge of atoms are used for estimations of total cross-sections during each MD simulation step. The cross sections for photoionization, electron–impact ionization and elastic process are obtained from experimental measurements (see Appendix B). The cross sections for inverse bremsstrahlung with both atomic structure and plasma screening effects considered are calculated in § 1.3. The rates for three-body recombination are calculated in § 1.4, and the formulas for corresponding cross sections is presented in Appendix C.

The ionization thresholds of an atom or ion may be modified by the charge background. In this model, the ionization thresholds in environment of charged cluster use same values as those of isolated atoms or ions. There are two reasons for this: (i) it is difficult to calculate reliable ionization thresholds in such complex charge system; (ii) the requirement of energy conservation in ionization events may change actual ionization thresholds indirectly. For example, an impact electron with enough kinetic energy in a possible ionization event may have a too low total energy for releasing a secondary electron due to background charges, and therefore, the event is forbidden by energy conservation. The background charges do influence ionization processes in this model, and modify ionization thresholds in some sense.

At the beginning of a MD simulation, the atomic positions in a cluster are initialized on regular grid points within a sphere volume. The closest distance between atoms (grid points), estimated from experimental cluster density, is 4.33 Å for xenon clusters, and 3.70 Å

for argon clusters. The reasons for this initialization of atomic positions are: (i) the van der Waals potential energy ($\sim 10^{-4}$ eV) among atoms in the gas cluster is much smaller than the Coulomb potential (~ 1 eV) between two singly-charged atoms at same distance, and therefore, the van der Waals interaction can be neglected at the beginning; (ii) Monte Carlo events are more sensitive to statistical properties of the system, such as atom/ion density, than to the individual atom positions.

The FEL pulse is assumed to be temporally rectangular and spatially uniform. The results in § 1.8 show that the simulations mainly depend on photon fluence of the pulse and that this rectangular pulse shape approximation is enough for current simulations. Sufficient simulation time for the first phase is several times longer than the pulse duration which is about 100 fs. After the laser pulse, *photoionization* and *inverse bremsstrahlung* events do not occur in the simulated system. The remaining collision events continue, and the system enters into a local thermodynamic equilibrium (LTE) phase with a balance between electron-impact ionization and recombination events. The populations of electrons and ions inside the cluster can be modified slightly due to cooling of the electron gas. The end of the second phase which occurs on the time scale of a picosecond is beyond the scope of this work.

The MD simulation results statistically fluctuate. To obtain predictions from this MD model, hundreds of independent simulations[5] are performed and then the simulated results are statistically averaged. The error can be estimated by the standard deviation of the average.

In the following two sections, two published papers present simulation results on the spectra of ions and photoelectrons for xenon and argon clusters irradiated by VUV FELs. Simulations were performed with both a Boltzmann method and this MD model.

[5]Here, the "independent" means that random numbers for Monte Carlo events in different simulations are uncorrelated. In practice, different seeds in random number generation are chosen for independent simulations.

1.6 Energetics, ionization, and expansion dynamics of atomic clusters irradiated with short intense vacuum-ultraviolet pulses[6]

Abstract

Kinetic equations are used to model the dynamics of Xe clusters irradiated with short, intense vacuumultraviolet pulses. Various cluster size and pulse fluences are considered. It is found that the highly charged ions observed in the experiments are mainly due to Coulomb explosion of the outer cluster shell. Ions within the cluster core predominantly recombine with plasma electrons, forming a large fraction of neutral atoms. To our knowledge, our model is the first and only one that gives an accurate description of all of the experimental data collected from atomic clusters at 100 nm photon wavelength.

Atomic clusters are excellent objects to test the dynamics within samples irradiated with radiation from short wavelength free-electron-lasers (FELs) [45, 46, 47]. Their physical properties put them on the border between the solid state and the gas phase. Cluster studies are important for planned experiments with FELs in solid state physics, materials science and for studies of the extreme states of matter [48]. Accurate predictions of ionization, thermalization and expansion timescales within irradiated samples, which may be obtained with cluster experiments [3, 22, 4, 21, 49], are also needed for exploring the limits of experiments for single particle diffraction imaging [44, 50, 51, 52, 53, 54].

During the first cluster experiments performed at the FEL facility FLASH at DESY with VUV photons of energy, $E = 12.7$ eV, and power densities up to a few 10^{13} W/cm^2 [3] energetic, highly charged Xe ions were detected. The estimated energy absorption was almost an order of magnitude higher than that predicted with classical absorption models [22, 4, 21], and the ion charge states created were much higher than those observed during the irradiation of isolated atoms in similar conditions. This indicated that at these wavelengths some processes specific to many-body systems were responsible for an enhanced energy absorption.

The physics underlying the dynamics within the irradiated clusters is complex. Several interesting theoretical models have been proposed in order to describe the evolution of clusters exposed to intense VUV pulses [5, 6, 7, 8, 23, 9, 55]. These include: (i) heating of quasi-free electrons due to enhanced inverse bremsstrahlung (IB) [5, 6], (ii) enhanced photoionization within the sample due to a lowering of the interatomic potential barriers [7, 8], and (iii) heating due to many-body recombination processes [9]. Each of these various approaches leads in a different way to a significantly enhanced energy absorption in agreement with the experimental data [3].

In order to evaluate the contribution of various processes to the ionization dynamics, including the enhancement factors proposed in Refs. [5, 6, 7, 8, 9], we have constructed a

[6]This section has been published as *Paper III*: B. Ziaja, H. Wabnitz, F. Wang and E. Weckert, Phys. Rev. Lett. **102** 205002 (2009).

unified model [28, 29] based on kinetic equations. It included the following predominant interactions: photoand collisional ionization, elastic electron-ion and electron-atom scattering, IB heating of quasifree electrons, shifts of energy levels within atomic potentials due to the plasma environment, and shielded electron-electron interactions. IB rates were calculated as in Refs. [5, 6], using the effective atomic potentials. This led to the strong enhancement of these rates, comparing to the approaches that used the pointlike Coulomb potentials, e.g., [14, 15]. The calculated IB rates were included explicitly in the kinetic equations in the form of the additional source terms.

These interactions were discussed in detail in Ref. [28]. We do not include atom-ion, ion-ion and atom-atom collisions to our model, as their rates are small comparing to the electron-ion(atom) collision rates.

Using a nonequilibrium Boltzmann solver, we followed the evolution of Xe clusters of various size irradiated with rectangular shaped VUV pulses of intensity $10^{12} - 10^{14}$ W/cm^2 and pulse duration, between 10 and 50 fs. We found that each physical mechanisms included into the model contributed to the ionization dynamics, however, with differing weights. The total ionization rate within the sample was most strongly affected by the IB heating rate applied. Within the theoretical framework defined above [28] we estimated that (i) many-body recombination (four-body and higher) [9] could contribute only for clusters irradiated at low pulse fluences, and (ii) the plasma environment effects estimated with electron screened atomic potentials were small. This was in contrast to the estimates of Ref. [7] performed with unscreened atomic potentials. Our studies [28, 29] extended the treatment of Ref. [6], where neither the spatial inhomogeneity of the clusters was treated nor the gross movement of electrons. It arises that both effects significantly contribute to the cluster dynamics. The structure of charge created within the cluster was found experimentally to be strongly inhomogeneous [56], and this inhomogeneity was induced by the dynamics of electrons.

The main aim of this Letter is to obtain a complete description of the energetics, ionization and expansion dynamics of irradiated clusters. Our present analysis differs from the analysis in [28, 29] by including the effect of three-body recombination and following the expansion of the cluster until ions begin to leave the simulation box (up to ~ 2 ps). In other words, we now follow the dynamics starting from the geometry of dense, neutral clusters up to a dilute gas of isolated ions, electrons, and neutral atoms.

The three-body recombination is the inverse of the collisional ionization, and this relation is used here in deriving the relevant rates. Including the three-body recombination into our code, we take into account the fact that the first phase of the cluster evolution is nonequilibrium. Therefore, we follow the approach of Ref. [36] and estimate the three-body recombination contribution, assuming an arbitrary electron distribution. This approach is appropriate both for the nonequilibrium and the equilibrium evolution phase. The recombination rates are then estimated, using the microscopic reciprocity of differential cross sections for collisional ionization and recombination [35]. The results from the model are averaged over the spatial pulse profile. Furthermore, they are also cross-checked with independent

molecular dynamics (MD) simulations. This leads to the following observations:

(i) In the previous work [28, 29] the hypothesis was proposed that the dominant contribution to the observed ion spectra may come from the outer shell of the irradiated cluster. In order to justify this hypothesis, the inclusion of the recombination within the cluster, following its expansion and averaging the results obtained over the spatial pulse profile was necessary. Only then could the predictions obtained with the model be compared to those recorded by the time-of-flight detector during the experiment.

(ii) The impact of three-body recombination on the ionization dynamics is very important. In particular, it has changed the estimated ion charge distribution within the ionized cluster. In contrast with the results of Refs. [28, 29] the highest ion charges are now created in the outer shell of the cluster and not within the cluster core. A large fraction of neutral atoms could also be found within the cluster core. The proportion is dependent on the cluster size and pulse fluence.

(iii) Including the cluster expansion has also allowed us to observe the differing expansion dynamics for both small and large clusters.

(iv) We have tested our model with an independent, dedicated molecular dynamics simulation for smaller clusters. The results obtained from both methods are in good agreement. This confirms that our analysis was not biased by our choice of simulation method.

The dynamics within the irradiated clusters depends on the pulse fluence and the cluster size. We have performed simulations of irradiated clusters with parameter values corresponding to those at the first FLASH cluster experiment at 100 nm wavelength [3, 21]. Below we compare the predictions to the experimental data.

The simulations were performed for clusters exposed to single rectangular shaped VUV pulses of a fixed fluence. The temporal VUV FEL pulse shape varies from shot to shot.We accounted for that approximately by performing a number of simulations with different pulse lengths at each value of the fluence. The intensity was set to the fluence divided by the pulse length. For the quoted ranges of pulse duration and a fluence range of 0.05 to 1.5 $\mathrm{J/cm^2}$, the full intensity range was $10^{12} - 1.5 \times 10^{14}$ $\mathrm{W/cm^2}$. The predictions obtained were then averaged over the number of simulated shots. This scheme followed the experimental data analysis [3, 4]. We estimate that the real value of pulse fluence may be up to 1.5 times smaller and up to 2 times larger than that one estimated experimentally. This asymmetry is due to systematic errors in the fluence estimation.

We obtain predictions for two limiting cases: (i) a cluster placed in the center of the focused beam and (ii) the position of the cluster integrated over the approximately estimated spatial profile of the pulse. As we will see later, at higher pulse fluences averaging over the spatial pulse profile has a higher impact on the model predictions compared to the case of a cluster placed in the center of the focused beam. This is due to the strong nonlinear dependence of the ion charge created on pulse fluence, at higher pulse fluences. At lower fluences this dependence is linear.

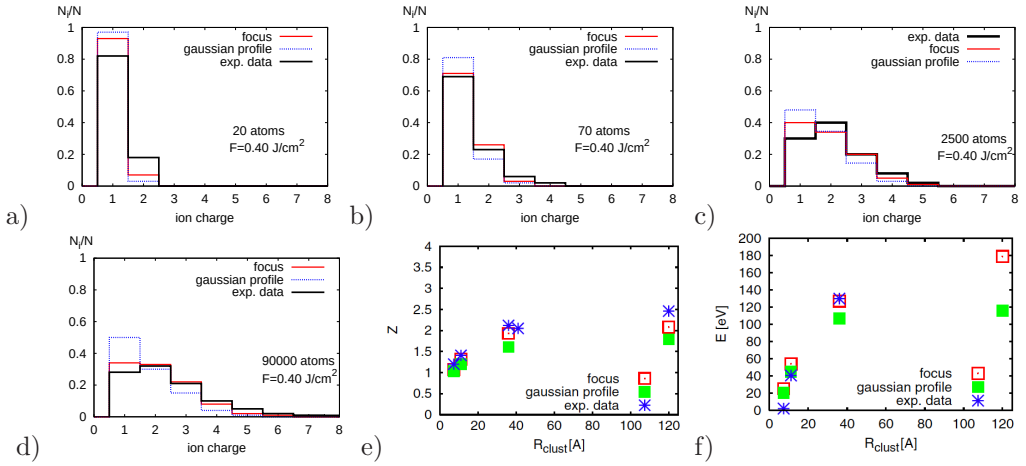

Figure 1.9: Ion fractions, N_i/N, within the irradiated clusters estimated for four various cluster sizes. N_i denotes here the number of Xe^{+i} ions, and N is the total number of ions. We show also: (e) average charge, Z, created within the irradiated cluster, and (f) average energy absorbed per ion, E, as a function of the cluster radius, R. Experimental data, model predictions for clusters placed in the center of the focussed beam and predictions integrated over the Gaussian spatial pulse profile are shown.

First, we will investigate ionization dynamics at different cluster sizes. In Figs. 1.9(a)-1.9(d) we plot the charge state distributions at the end of the expansion phase obtained for four different cluster sizes irradiated with a fixed pulse fluence of 0.4 J/cm^2 . The trend can be understood in the following way. IB is the dominant mechanism of energy absorption within our model. This process heats up the quasifree electrons within the cluster. The hot electrons collide with ions and atoms, producing higher charges and releasing new electrons. These processes compete with the three-body recombination processes that reduce the ion charge and decrease the electron density. After the pulse is over, and the system reaches a local thermodynamic equilibrium (LTE) state, the number of ionization and recombination events saturates, changing slowly with the decreasing temperature within the cluster. We find that during the exposure the cluster forms a shell structure [56] consisting of a positively charged outer shell and a core of net charge equal to zero. Such a shell structure has been previously found by other groups in the context of x-ray irradiation of clusters and biomolecules [7, 57, 58]. The width of these shells depends on the cluster size. The charged outer shell is large within small clusters ($N_{atoms} = 20, 70$), and its Coulomb explosion drives the expansion of these clusters. Within large clusters ($N_{atoms} = 2500, 90000$) the neutral core is large, and after the Coulomb explosion of the outer shell it expands hydrodynamically. Highly charged ions within the core recombine efficiently with electrons. As a result, we observe a large fraction of neutral atoms created within the core, the proportion depending on the cluster size. This fraction is from 15% to 40% of the total number of particles. Within small clusters a large fraction of the electrons released during the ionization processes can leave the clusters early in the exposure. The remaining electrons are not heated efficiently

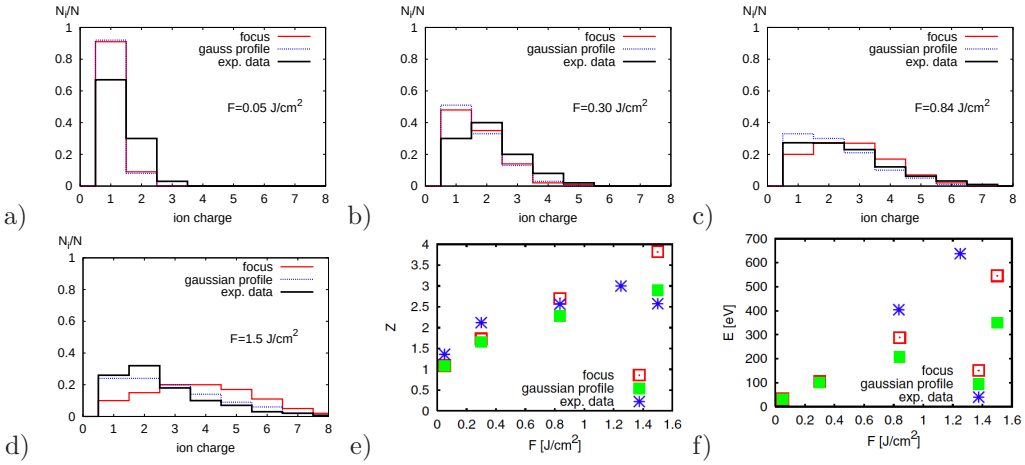

Figure 1.10: Ion fractions, N_i/N, within the irradiated xenon clusters ($N_{atoms} = 2500$). These clusters were irradiated with rectangular shaped pulses of four various fluences. We show also: (e) average charge, Z, created within the irradiated xenon cluster, and (f) average energy absorbed per ion, E, as a function of the pulse fluence, F. Other notations are as in Fig. 1.9.

via IB processes due to their low density within the cluster. Consequently, only low charge states are observed [Figs. 1.9(a) and 1.9(b)]. In contrast, within large clusters of 2500 and 90000 xenon atoms only a small fraction of the released electrons are able to escape from the cluster. The width of the positively charged outer shell is small with respect to the radius of the neutral core. Electrons confined within the core are then heated efficiently. This leads to further collisional ionizations. In Fig. 1.9(c) and 1.9(d) we plot the respective ion fractions. Our predictions are in agreement with the experimental measurements. The trend of the size dependence is correct. At a fixed pulse energy the maximal and average ion charge created increases with the cluster size until it saturates at larger cluster sizes. This is in agreement with the experimental data [Fig. 1.9(e)]. Saturation of the ion charge created within large clusters (irradiated with a pulse of a fixed fluence) is due to the fact that for large enough clusters the energy absorbed from the pulse will not be sufficient for the creation of higher charge states. We also show our estimates for the average kinetic energy per ion, E, [Fig. 1.9(f)]. It increases with the cluster size and saturates for larger clusters.

With the extended Boltzmann solver we were able to follow the different expansion dynamics for large and small clusters (not shown due to limitations of space). In the case of small clusters the expansion was driven by the Coulomb explosion, and ions then quickly filled the whole volume of the simulation box. In the case of a dominating hydrodynamic expansion of the sample, the evolution proceeded shell-after-shell as predicted by earlier simulations [52].

The dependence of the ionization dynamics on pulse fluence has been investigated for Xe_{2500} clusters. Below we show the plots of the ion fractions [Figs. 1.10(a)-1.10(d)]. Higher

pulse fluences lead to the creation of higher charge states within the clusters in accordance with the mechanism described above. At the lower pulse fluences, $F = 0.05 - 0.3$ J/cm^2, the small discrepancy between experiment and our predictions may be due to the fact that an additional energy absorption due the many-body recombination effects within the cold electron plasma can occur [28]. This could then lead to the creation of higher charge states that we do not observe within our model, as manybody recombination [9] was not included into it. At higher fluences, $F = 0.84 - 1.5$ J/cm^2, the ion fractions are in good agreement with experimental data.

The average charge is plotted as a function of pulse fluence in Fig. 1.10(e). With increasing pulse fluence the average charge created increases. The charges calculated are very close to the corresponding experimental values. Also, as expected, the content of neutral atoms found within the cluster decreases at the increasing pulse fluence: from 70% to 5% for fluences, $F = 0.05 - 1.5$ J/cm^2 (not shown).We also show the average kinetic energy per ion as a function of the pulse fluence [Fig. 1.10(f)]. The sparse experimental data do not allow the identification of the trend of the fluence dependence, i.e., whether it is linear or nonlinear. Our predictions slightly underestimate the experimental predictions for ion energy at high fluences but stay within the error limit given by the experimental uncertainty of fluence estimation.

In summary, we used a microscopic Boltzmann model to investigate dynamics within atomic clusters irradiated by single VUV pulses. The predictions obtained at various cluster sizes and pulse fluences were found to be in good overall agreement with experimental data considering the uncertainty of the pulse fluence estimation. The results obtained have been successfully cross-checked with MD simulations showing that they are not biased by the choice of our particular simulation method. Because of limitations of space we do not discuss theMD results here. The present analysis shows that recombination contributes significantly to the ionization dynamics. As expected, the recombination has the highest impact within the cluster core where the electron density is highest. This indicates that the ions detected during the experiment originate mainly from the outer region of the cluster [56]. We found a large fraction of neutrals exist within the core resulting from the recombination, the proportion depending on the cluster size. This prediction is especially important, as neutral fragments can be detected in an experiment only with a great difficulty. If we ignore them, the total energy absorption due to the laser-cluster interaction may be extensively overestimated.

In conclusion, we find that formation of high charge states and the strong absorption of VUV radiation is quantitatively understood within the framework of our model.

1.7 Emission of electrons from rare gas clusters after irradiation with intense VUV pulses of wavelength 100nm and 32nm[7]

Abstract

Kinetic Boltzmann equations are used to describe electron emission spectra obtained after irradiation of noble-gas clusters with intense vacuum ultraviolet (VUV) radiation from a free-electron-laser (FEL). The experimental photoelectron spectra give a complementary and more detailed view of nonlinear processes within atoms and clusters in an intense laser field compared to mass spectroscopy data. Results from our model obtained in this study confirm the experimental and theoretical findings on the differing ionization scenarios at longer (100 nm) and shorter (32 nm) VUV radiation wavelengths. At the wavelength of 100 nm the thermoelectronic electron emission dominates the emission spectra. This indicates the plasma formation and the inverse bremsstrahlung (IB) heating of electrons inside the plasma. This effect is clearly visible for xenon (with the fitted temperature of 6-7 eV), and less visible for argon (with the fitted temperature of 2-3 eV). The two-photon-ionization rate for argon that initiates the cluster ionization, is much lower than the singlephotoionization rate for xenon. Also, more of the photoelectrons created within an argon cluster are able to leave it, as they are more energetic than those released from a xenon cluster. Therefore, the IB heating of plasma electrons in argon is less efficient than in xenon, as the density of the electrons remaining within the cluster is lower.
At a wavelength of 32 nm the dominant ionization mechanism identified from the electron spectra of argon clusters is the direct multistep ionization. The signature of the thermalization of electrons is also observed. However, as the heating of electrons due to the inverse bremsstrahlung process is weak at these radiation wavelengths and pulse fluences, the increase of the electron temperature with the pulse intensity is mainly due to the increasing photoionization rate within the irradiated sample.

Introduction

Studies performed with atomic clusters exposed to intense short wavelength radiation from free-electron-lasers (FELs) [19, 49, 3, 4, 56, 59, 60] and to higher harmonic radiation [61] reveal interesting information on the ionization dynamics of the irradiated samples. These studies are important for planned experiments with FELs in solid state physics, materials science and for studies of the extreme states of matter [48, 62, 63]. Accurate predictions on the ionization, thermalization and expansion timescales that can be obtained with cluster experiments are also needed for exploring the limits of experiments on single particle diffraction imaging [44, 50, 51, 52, 53, 54].

Time-of-flight (TOF) mass spectroscopic studies performed at 100 nm radiation wavelength demonstrated a strong energy absorption within clusters, compared to absorption by single atoms. Coulomb explosion of Xe and Ar clusters resulting in emission of multiply charged ions with keV kinetic energies was recorded, using mass spectroscopic methods [3, 4, 21]. In contrast, the TOF ion spectra of Ar recorded at 32 nm wavelength exhibited

[7]This section has been published as *Paper IV*: B. Ziaja, T. Laarmann, H. Wabnitz, F. Wang, E. Weckert, C. Bostedt and T. Möller, New Journal of Physics **11** 103012 (2009).

rather narrow peaks, showing that Ar fragments do not carry significant kinetic energies [49]. This indicated a less efficient ionization mechanism.

The photoemission spectroscopy studies performed in [19, 49] gave a complementary and more detailed view on ionization of atoms and clusters in an intense laser field, compared to the results from mass spectroscopy. At a peak intensity of $\sim 4.4 \times 10^{12}$ W cm^{-2} and average pulse duration of 100 fs, the kinetic energy distribution of emitted electrons strongly decreased at kinetic energies of 30-40 eV. A characteristic electron temperature below 10 eV was obtained. Simulations with a time-dependent Thomas-Fermi model supported the description of electron spectra as resulting from the thermoelectronic emission from the plasma.

Photoelectron studies performed at 32 nm wavelength [49] suggested a differing ionization dynamics within the irradiated clusters that is driven by a direct multistep photo- and collisional ionization. The inverse bremsstrahlung (IB) heating of the nanoplasma is of minor importance at these short radiation wavelengths. Non-dynamic Monte Carlo simulations were performed for 32 nm wavelength in order to support this hypothesis [49]. Here we obtain predictions for the photoemission spectra, using the comprehensive theoretical framework of the kinetic Boltzmann model [27, 28, 29, 43]. Analysis of ionization dynamics at similar photon energies was also performed in [64, 65]. So far, our model has been successful in reproducing the mass spectroscopic results obtained from the first cluster experiment at FLASH [3, 4] performed at 100 nm wavelength. Below we describe our results on the electron emission spectra in detail.

Experimental scheme and simulations

First, we describe briefly the experimental scheme [19, 49]. The rare gas clusters of Xe, Ar were prepared in a supersonic gas expansion. The average cluster size was tuned by varying the stagnation pressure. The full-width at half-maximum of the size distribution is then approximately equal to the average cluster size. FEL radiation was focused on the cluster beam, using an elliptical mirror at grazing incidence. Pulse duration was estimated indirectly with statistical and spectral methods. In case of irradiation with 100 nm radiation, the estimated pulse length was $\sim$100 fs. In the case of irradiation with 32 nm radiation, the pulse length was $\sim$25 fs. In both cases the peak intensity was up to $\sim 10^{13}$ W cm^{-2}.

The electrons generated during the laser cluster interaction were detected with the microchannel plate of a TOF spectrometer. Kinetic energies of electrons ranging from a few electron volts up to a few tens of electron volts could be analysed. The measured electron distribution curve was converted into kinetic energy spectra [19, 49] and corrected with respect to the calculated transmission of the spectrometer. The electron spectra were obtained by averaging the single-shot spectra over many laser shots. Due to the strongly varying transmission of the spectrometer towards low kinetic energies, the line shapes could not be properly evaluated at energies below 5 eV.

Our theoretical simulations were performed for clusters exposed to single rectangular shaped vacuum ultraviolet (VUV) pulses of fixed fluence. The fluence was a product of the experimentally recorded average pulse intensity and of the pulse length.We obtained predictions for the position of the cluster integrated over the approximately estimated Gaussian spatial profile of the pulse, along the lines of the experimental conditions. For the theoretical simulations we have used a unified Boltzmann model [28, 29] based on kinetic equations. It included the following interactions: photo- and collisional ionization, threebody recombination, elastic electron-ion and electron-atom scattering, IB heating of quasifree electrons, shifts of energy levels within atomic potentials due to the plasma environment, and shielded electron-electron interactions. IB rates were calculated as in [5, 6], using the effective atomic potentials. The calculated IB rates were included explicitly in the kinetic equations in the form of the source terms. These interactions and further details of the model were discussed in [28].

Our model follows the full dynamics of irradiated clusters starting from the nonequilibrium ionization phase up to the semi-equilibrium expansion phase. It treats all relevant interactions within the irradiated sample. It gives a complete, consistent description of the cluster evolution. This is the advantage of this model when compared to the simplified models used for the simulations in [19, 49]. The hydrodynamic Thomas-Fermi model [66] used in [19] described only the dynamics of small argon clusters Ar_{55} irradiated with 100 nm radiation, whereas the experimental data were obtained for Ar_{300} and Xe_{70} clusters. This model assumed the full single ionization of the sample at the initial state, so photoionization was not treated there. In the framework of this hydrodynamic model the non-equilibrium phase of sample evolution was neglected. Also, the frozen core approximation was used, i.e. the positions of ions were fixed during the simulations.

Dedicated simulations performed in order to describe experimental results of [49] were nondynamic Monte Carlo simulations. They were assuming: (i) statistical photoionization of the sample constituents; (ii) instantaneous escape of electrons with an asymptotic kinetic energy (only direct ionization events with positive kinetic energy were accepted) and (iii) no motion of atoms/ions during the pulse (no other processes were included). This simulation scheme just tested the hypothesis that the direct multistep ionization dominates the electron spectra.

Ionization dynamics at 100 nm

Predictions obtained with other theoretical models [5, 6, 67, 8, 23, 9, 55] and with our model [27, 28, 29, 43] demonstrated that a heating mechanism within a many-body system irradiated with VUV radiation leads to the fast formation of an electron-ion plasma. Enhanced IB [5, 6] was among the potential mechanisms of the plasma heating. As in [5, 6], we apply this plasma heating mechanism in our model.

Shortly after the pulse is off, the plasma evolves towards a local thermodynamic equilibrium (LTE). The electron emission spectrum for xenon gives a clear indication that the

heating of electrons was efficient and fast electron thermalization took place: the full emission spectrum can be well fitted by the Maxwell-Boltzmann (M-B) distribution (figure 1(a)). The experimentally estimated temperature of $T = 7.1$ eV is in good agreement with the prediction from our model, $T = 6.5$ eV (figure 1(a)). The photoelectron peak due to single photoionization of neutral xenon atoms (<1 eV) cannot be properly identified as it shows up below the spectrometer transmission limit of 5 eV (experimental data) and overlaps with the peak of the M-B distribution (model predictions).

In the argon spectra the distinct two-photon-ionization peak at energies ∼10 eV is clearly visible (figure 1(b)). This two-photon-ionization mechanism initiates the (single) ionization of the neutral Ar cluster, as the photon energy (13 eV) is below the threshold for the single photoionization (15.8 eV). The two-photon single ionization rate is about 40-80 times smaller than the rate for the single photoionization of xenon at the considered pulse intensity $\sim 4 \times 10^{12}$ W cm^{-2}. Also, at this pulse intensity the resonant excitation does not contribute significantly to the total heating rate, and thus can be neglected [21]. Therefore, the ionization in argon progresses much slower than in case of xenon. Also, more energetic photoelectrons in argon ($E_{kin} = 10$ eV), compared to xenon ($E_{kin} < 1$ eV) are more likely to escape from the irradiated cluster. As a result, a dilute plasma of quasi-free electrons is created inside the Ar cluster, and therefore the IB heating within argon is much less efficient than that in xenon.

Due to the presence of the large photoelectron peak at 10 eV and also to the additional small peak at 23 eV, which is presumably due to single-photon ionization of neutral argon atoms by third harmonic of FEL radiation [19], fitting the full M-B distribution to the argon data is difficult (figure 1(b)). The final M-B fit to the experimental data reveals the photoelectron temperature, $T = 3.5$ eV, and is in good agreement with the predictions on photoelectron spectra from our model, $T = 2.8$ eV. Our photoelectron temperature estimates are lower than those obtained in [19], where the data from the region below 5 eV have been also used for fitting, and an asymptotic exponential fit was applied, instead of the full M-B distribution [19] that is now fitted to the data.

Finally, we mention that the additional small peaks for argon which are presumably due to the ionization of neutral atoms by third harmonic of FEL radiation [19] cannot be obtained within our model, as we did not include the irradiation by the third harmonic there.

We show also the results from the model on: (i) the total electron temperature in the whole simulation box (measured after the thermalization of quasi-free electrons within the cluster and after the escape of the photoelectrons from the simulation box), (ii) the average charge state formed inside the cluster, and (iii) the estimated average energy per ion, as functions of fluence in the range 0.05-0.5 J cm^{-2} (figure 3). For the considered pulse length of 100 fs this corresponds to pulse intensities in the range $5 \times 10^{11} - 5 \times 10^{12}$ W cm^{-2} . These predictions confirm the above dynamics scenarios for xenon and argon. The total electron temperature for argon clusters is lower than the temperature for xenon clusters due to the

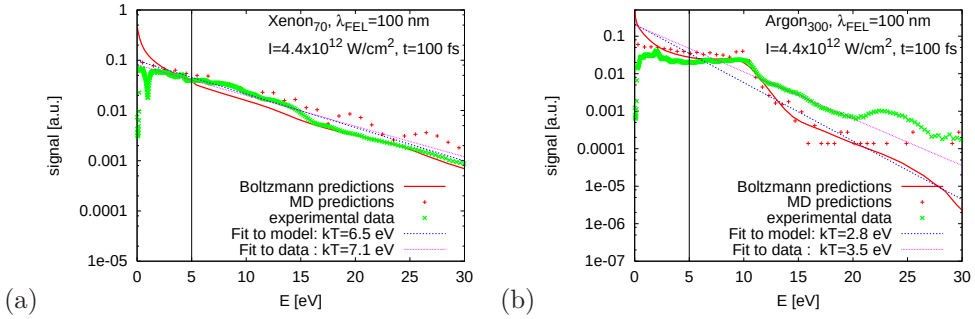

Figure 1.11: Electron emission spectra for: (a) Xe_{70}, and (b) Ar_{300} clusters obtained after their irradiation with FEL pulses ($\lambda_{\mathrm{FEL}} \sim 100$ nm) of average duration of 100 fs and pulse intensity, 4.4×10^{12} W cm^{-2}. Logarithmic scale is used in order to facilitate the temperature fits. We show also the results from our MD simulations. The vertical line at 5 eV shows the data cut off.

less efficient IB heating within the argon cluster. The density of the photoelectron plasma in the argon cluster is lower, due to the slow two-photon-ionization rate of argon and the higher escape rate of energetic photoelectrons from argon clusters. The lower electron temperature results in a lower average charge state generated within the argon cluster, compared to case of xenon clusters, and finally in a lower average ion energy. These quantities increase sublinearly with the pulse fluence, and saturate at higher pulse fluences.

The results obtained with Boltzmann model were cross checked with our molecular dynamics (MD) simulations, showing that they are not biased by the choice of the particular simulation method.

Ionization dynamics at 32 nm

Analysis of the photoelectron spectra at 32 nm performed in [49] indicated that the direct multistep ionization may be the dominant ionization mechanism at this radiation wavelength. Our predictions confirm this hypothesis. After performing dedicated simulations at the highest pulse intensities, we found out that the IB heating contributes to the total energy absorption by argon clusters only by the order of 2% at most at this particular wavelength. These findings are in compliance with recent independent MD-calculations [68].

The direct multistep ionization process is initiated by single photoionization of Ar atoms and indicated in the emission spectra by a pronounced 3p photoionization peak at $\sim$ 22 eV. Other processes follow the photoionization, i.e. (i) photoionization of Ar^{+1}, (ii) the escape of photoelectrons from the cluster, (iii) thermalization of quasi-free photoelectrons within the plasma, (iv) creation of secondary electrons during collisions of photoelectrons with ions/atoms within the cluster [28, 29] and (v) collisional (three-body) recombination [43].

With the increasing number of photoelectrons emitted, the attractive Coulomb field inside the cluster grows. It reduces the kinetic energy of subsequently emitted electrons and

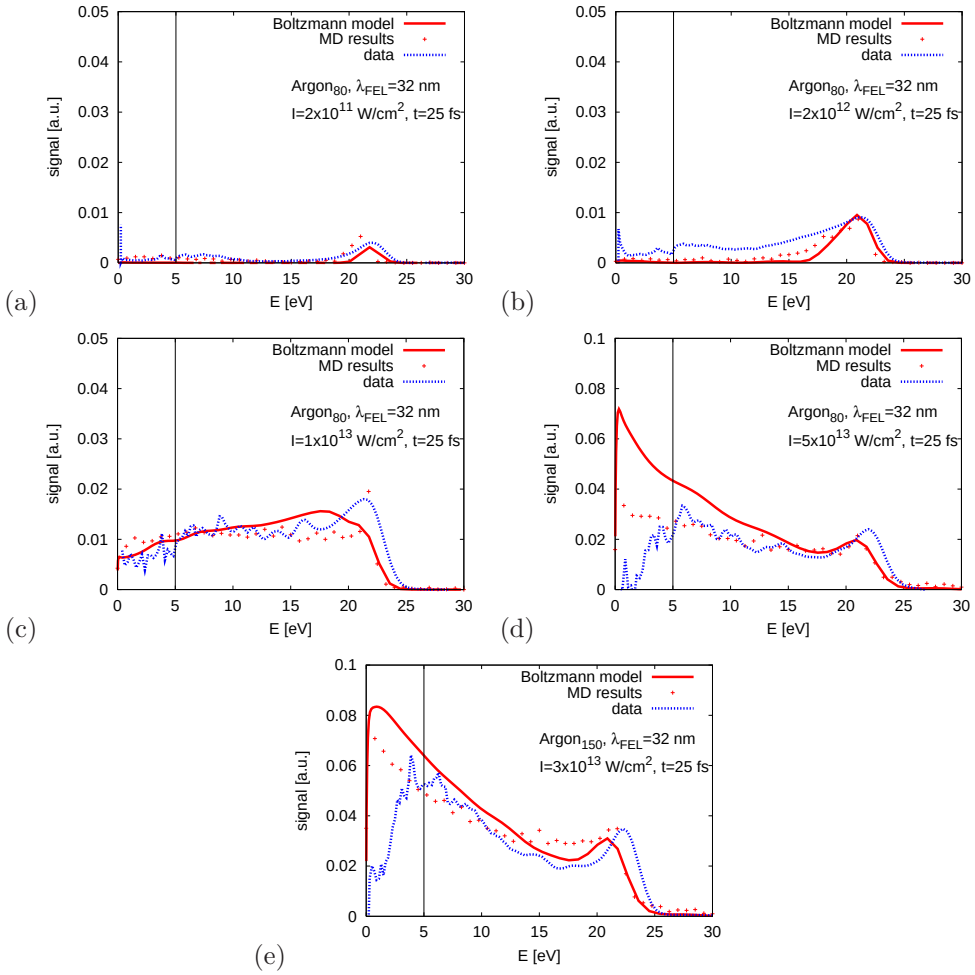

Figure 1.12: Electron emission spectra for: (a-d) Ar_{80}, and (e) Ar_{150} clusters. Clusters, Ar_{80} were irradiated with single FEL pulses ($\lambda_{\mathrm{FEL}} = 32$ nm) of intensities in the range of $0.02 - 5 \times 10^{13}$ $\mathrm{W\,cm^{-2}}$ and the average pulse duration of 25 fs. Cluster, Ar_{150}, was irradiated with a FEL pulse of intensity, 3×10^{13} $\mathrm{W\,cm^{-2}}$. We show also the results from our MD simulations. The vertical line at 5 eV shows the data cut off.

eventually prevents further electron emission, leading to the generation of a thermally equilibrated nanoplasma. The contribution of thermalized electrons observed in photoemission spectra increases with time, and, as expected, electron temperature increases with increasing pulse intensity (figure 2). However, as the heating of electrons due to the IB process is negligible (2% effect), the increase of the electron temperature with the pulse intensity is mainly due to the increasing photoionization rate within the irradiated sample.

The predictions obtained from our model for: (i) the total electron temperature inside the whole simulation box (measured after the thermalization of electrons within the cluster and after the escape of the photoelectrons from the simulation box), (ii) the average charge state created and (iii) the estimated average energy per ion, in the argon clusters Ar_{80} and Ar_{150} support the above scenario (figure 3). These predictions were obtained for fluences in the range $0.005 - 1.25$ J cm^{-2}. For the considered pulse length of 25 fs this corresponds to the pulse intensities in the range $2 \times 10^{11} - 5 \times 10^{13}$ W cm^{-2}.

At a low pulse fluence electrons are produced almost solely during the photoionization process. These photoelectrons can then escape from the cluster. The escape of photoelectrons increases the potential energy of the system. The total electron temperature recorded after the time longer than the electron thermalization time and photoelectron escape time is low, as almost all photoelectrons have left the cluster and the simulation box by that time.

With the increasing pulse fluence more photoelectrons are released. They can escape from the cluster until the attractive Coulomb field of the cluster becomes so large that it prevents further electron emission. This leads to the generation of a thermally equilibrated nanoplasma, as has been observed also in recent MD calculations [49, 68]. More electrons can escape from the larger clusters, creating higher potential energy within the system. This is reflected by a stronger increase of the estimated average energy per ion and of the total electron temperature with the pulse fluence for Ar_{150} clusters than for Ar_{80} clusters. In contrast, the average charge state created is not cluster-size dependent (figure 3), as it was created mainly during photoionization. As in case of irradiation with 100 nm wavelength, the dependence of the total electron temperature, the average charge state and the average energy per ion on the pulse fluence is sublinear, and saturates at higher pulse fluences.

Performing our studies at 100 nm and 32 nm, we restricted ourselves only to the cluster sizes and FEL pulse parameters that were investigated experimentally. This was done in order to test the predictivity and accuracy of our model. As differing energy absorption processes are predominant at different wavelengths, and the ionization dynamics is a nonlinear function of pulse fluence (figure 3), the comparison of the results obtained at 100 nm and 32 nm is not straightforward. The photoionization rate for argon at 100 nm is five times smaller than at 32 nm but the IB heating, which is negligible at 32 nm, contributes significantly to the energy absorption at 100 nm. In contrast, more photoelectrons can escape from argon clusters at 32 nm, as they are more energetic than those released from clusters at 100 nm. This greatly increases the potential energy within the clusters at 32 nm. Due to these competing processes, the net energy absorption within the investigated clusters that is

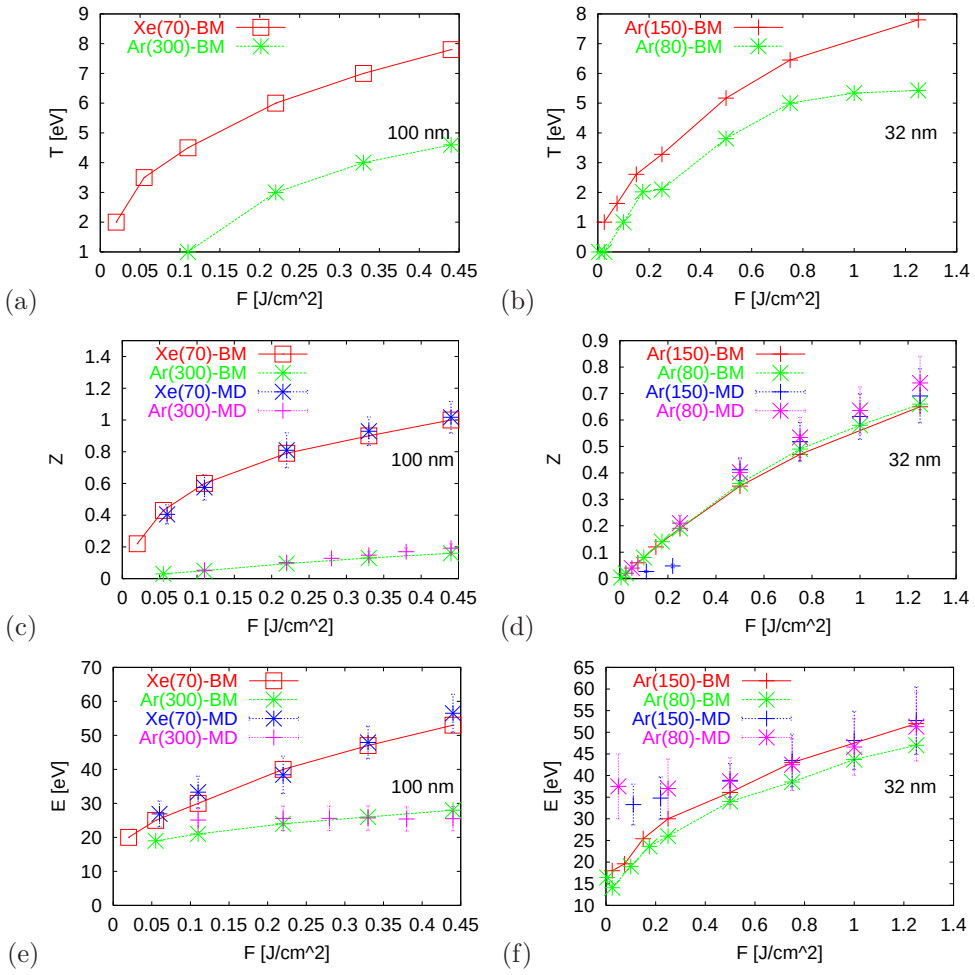

Figure 1.13: (a) Temperature of electrons inside the whole simulation box after the electron thermalization and after the escape of photoelectrons from the simulation box, (c) average charge state created within a cluster, and (e) estimated average energy per ion as functions of fluence at 100 nm wavelength for Xe_{70} and Ar_{300} clusters. Plots (b), (d) and (f) show the same parameters estimated at 32 nm for Ar_{150} and Ar_{80} clusters. We show both the results obtained with Boltzmann model (BM) and our MD code (MD).

reflected by the estimated average energy per ion (figure 3(e) and (f)), does not differ much for the case of irradiation with 100 nm and 32 nm wavelength.

In summary, our simulations performed within the framework of the Boltzmann model that included all predominant interactions and followed the non-equilibrium and equilibrium dynamics of irradiated samples, confirm the differing ionization scenarios at irradiation of atomic clusters with short- and long-wavelength VUV radiation as posed in [19, 49]. The physical mechanisms contributing are now understood and explained quantitatively. The results obtained have been successfully cross-checked with MD simulations by the Rostock group [68] and our own results showing that they are not biased by the choice of the particular simulation method. The MD results [68] are prepared for publication. All of the experimental electron emission spectra recorded at 100 nm and at 32 nm are now quantitatively reproduced and comprehensively understood within the framework of our kinetic model.

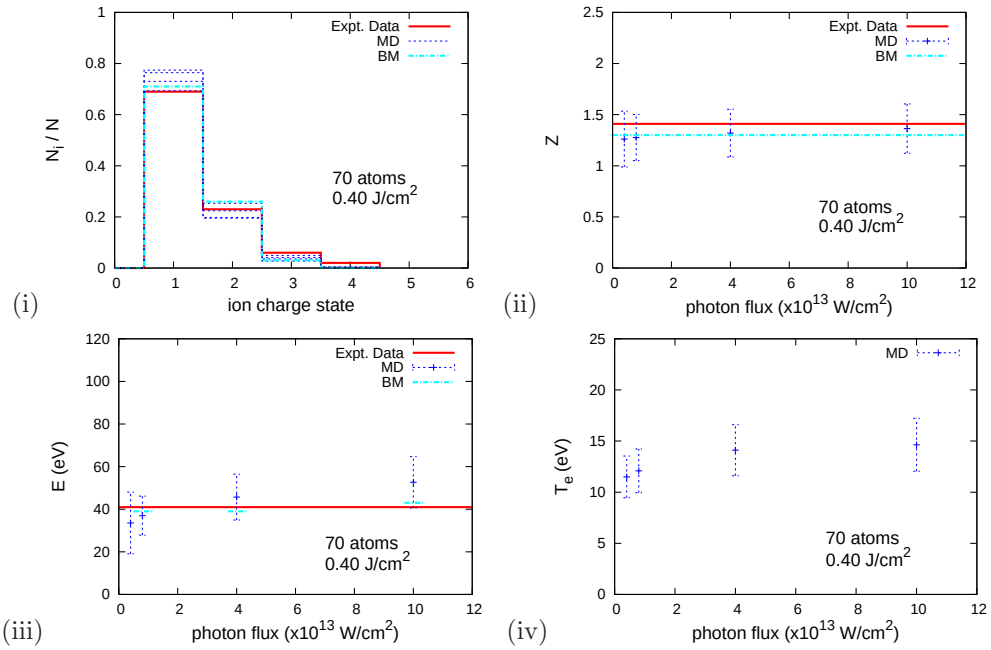

Figure 1.14: MD simulations of Xe_{70} clusters irradiated by FELs at 100 nm wavelength: (i) ion fractions N_i/N; (ii) averaged ion charge Z; (iii) energy absorption per ions E; (iv) electron temperature inside the clusters T_e . Both the experimental data and the results from the Boltzmann model (BM) are presented for comparison. The photon fluence in pulses is fixed at 0.40 J/cm^2 with variable pulse lengths (i.e. 100/50/10/4 fs for $0.4/0.8/1.0/10\times10^{13}$ W/cm^2 respectively). Note that the relevant experimental data in Fig. 1.1a were obtained at laser intensity 0.8×10^{13} W/cm^2 with 50 fs long pulses.

1.8 Results of the MD model

This part presents the MD simulations mentioned at the end of the published *paper III* (§ 1.6). The paper uses a Boltzmann model (BM) to simulate irradiated xenon clusters with variable cluster sizes and laser intensities. A program was developed for the MD model in § 1.5, but it was not optimized. Therefore, it is not suitable for large size clusters beyond 1000 atoms. Here, only the results of xenon clusters with 70 atoms are presented as a typical example, which corresponds to Fig. 1.9b in the paper.

The simulated Xe_{70} clusters are irradiated by the FELs at 100 nm wavelength. The laser intensity changes, but the photon fluence is fixed at 0.40 J/cm^2 . The pulse lengths in the simulations are between 4 fs and 100 fs, which corresponds to different rectangular pulse shapes. The results shown in Fig. 1.14 are recorded shortly after the end of irradiation (totally two times of the pulse lengths) in single simulations. The relevant physical quantities, such as relative population of ion charge, average charge of ions and absorption energy, are plotted with reference values from both the experiments and BM predictions. Error bars are the standard deviations of the predictions from 100 independent MD simulations in each

case of pulse length.

As shown in Fig. 1.14, the simulations are not sensitive to the pulse shapes at fixed photon fluence. The results in the MD model agree well with that in the BM and the experimental data in the error range. The electron temperature inside clusters is around 15 eV shortly after the irradiation.

The Boltzmann model, constructed by Ziaja et al. [27, 28], is a simulation model based on the Boltzmann equation to study the problem of irradiated atomic clusters. The system in the Boltzmann model is described by the particle density function $\rho(\mathbf{r}, \mathbf{v}, t)$ in phase space. The number of phase dimensions is reduced to two, r and v , in the BM with consideration of spherical symmetry. The numerous equations of particle motion are substituted with the Boltzmann equation. This reduction allows the computational performance of the method to be much higher than the MD codes, where the computation requirements scales with the square of particle number. In this work, the MD code is not optimized and is limited to 1000 atoms. The Boltzmann approach has a basic advantage that it does not scale with number of particles directly.

Another advantage is that the predictions of physical quantities from Boltzmann simulations have no value fluctuations. While fluctuation error is inevitable in MD simulations due to statistics based on individual particles, and an additional uncertainty is induced by Monte Carlo events. In each parameter case, more than 100 independent simulations were performed, and the measured quantities were calculated and averaged with corresponding standard deviations.

To sum, the MD model presented here uses the same cross sections as the Boltzmann model. The MD model can only simulate the cases of small clusters. In these cases, the two models agree with each other as illustrated by the above simulation results.

1.9 Summary and outlook

The high charge states and strong absorption of atomic clusters with the VUV radiation are quantitatively understood. The predictions of the MD model and the Boltzmann model are in agreement with all the experimental data obtained for irradiated clusters at 100 nm and 32 nm. The simulations show that the dominant mechanism, contributing a large amount of photon absorption in the xenon clusters at 100 nm wavelength is the enhanced IB effect. The enhanced IB effect becomes weak at 32 nm wavelength, and vanishes at shorter wavelengths. Then the dominant process is direct photoionization of electrons followed by collisional ionization.

From the Boltzmann model [29], we learn that a net neutral core with ions and slow electrons exists during the Coulomb explosion phase, while ions in outer shells escape quickly from the cluster. This is a good indication for imaging experiments. The neutral core could be the measured sample, while the outer shell is sacrificed as a tamper layer proposed in

[53, 69, 70]. The structure, made of light elements, possibly survives during an intense pulse at the sacrifice of the tamper layer. The idea has been tested by recent experiments on doped noble gas clusters [56]. The diffraction effect from the proposed tamper layer in single particle imaging is discussed in § 5.

Chapter 2

Imaging of atomic clusters

2.1 Introduction

Ultrafast imaging techniques are useful tools to study the dynamics of molecular and condensed matter systems. Currently, most dynamical information is deduced from spectroscopy experiments [71], for example, the time scale of photoelectrons escaping from conduction band of metal [72]. In the preceding chapter, the measured spectra of ions and photoelectrons measured were used for discussions and comparison with simulations of the dynamics within atomic clusters (noble gas clusters) irradiated by FELs. The spectroscopy experiments revealed an integration of the dynamics over temporal and spatial dimensions. In contrast, imaging techniques enable us to see structural changes in the irradiated clusters in real space and real time. In this chapter, *coherent diffractive imaging* (CDI) with FELs is applied to extend the study of dynamics within irradiated clusters.

CDI is an extension of X-ray crystallography. In contrast to requiring identical copies of a cell on a periodic lattice (known as a crystal), CDI images just single cell (or particle). Hence, it has an alternative name: *single particle imaging* (SPI). One of its most important features is that it is lensless between sample and detector, which enables CDI to avoid the diffraction limit of X-ray microscopes based on the use of objective lenses. It was firstly demonstrated with a synchrotron source [73], and has been widely applied in last ten years, such as: deformation of a nanocrystal [74], a 3D artificial structure [75], a freeze-dried yeast cell [76, 77] and a 3D human chromosome [78]. Even a table-top laser (high harmonic generation) produces enough photons that can be used as a CDI source [79]. A remarkable spatial resolution of around 5 nm was achieved by CDI using a synchrotron X-ray source [80].

The emergence of FELs, such as FLASH [1], opens new opportunities to apply CDI. The high coherence [81] and extreme intensity of FELs potentially enables CDI to achieve a higher spatial resolution than at synchrotron sources. The FEL pulses are so intense that

they can destroy most specimens; however, the pulses are ultrashort on the femtosecond scale, which enables FELs to image an object before its destruction [54]. The resolution currently achieved by CDI with FELs such as FLASH is mainly limited by the available wavelength range which is in the soft X-ray regime [82]. Using new hard X-ray FEL facilities such as LCLS [83] in future, CDI may reach spatial resolution at the atomic scale [71].

However, dynamics simulations [44, 58, 57, 84, 70] show that the problem of radiation damage during FEL imaging pulses is prominent when CDI enters the range of atomic resolution. It limits high resolution CDI with FELs, especially for biological particles (such as cells, macromolecules and proteins) which are of great interest in structural biology. In biological samples, the main component elements, such as carbon, are light and very sensitive to the radiation damage. Furthermore, there is the significant problem of low signal-to-noise ratio signals in X-ray CDI of biological samples, which will be discussed in the next chapter. The latter problem limits the direct experimental study of the radiation damage in CDI of single biological particles.

The effect of radiation damage of polystyrene nano-balls within picoseconds has been investigated through the time-delay holography [85]. The single FEL pulses traverse the balls triggering a damage, and are reflected back onto the balls by a mirror to probe the damage. An expansion of 6 nm within 350 fs was observed in the 140-nm-diameter balls with 25 fs exposure to single pulses of soft X-ray FELs at 10^{14} W/cm^2 . Since the elemental constitution in polystyrene is carbon and hydrogen, the observation is meaningful for imaging biological samples. The arrangement of these spherical particles on single imaging windows was applied in these experiments to increase the diffraction signals, which are averaged effects over individual particles. The sizes of the balls, which serve as starting points of reference sources, limit the accuracy of the measured expansions in a holographic point of view. Hence, further experimental study is necessary to understand the details of the effect of radiation damage in single particles. It is critical to clarify the imaging limit of high resolution CDI.

Atomic clusters, as a simple model of molecules, are unique objects for study of damage dynamics in CDI experiments with FELs. Noble atoms such as xenon have a much stronger photon-scattering ability than carbon. This enables CDI to image single atomic clusters of nanometer sizes. Xenon atoms are also much heavier than carbon, and this leads to a slow damaging expansion, which is easier for imaging experiments to follow. Atomic clusters have a loose-bound structure and a quasi-uniform density, which simplifies the model of chemical bounds or conformation motions inside biological particles. The model simplifications improve computational capability of the dynamics simulations, which may explain and extend the CDI results from irradiated atomic clusters. The CDI study of single atomic clusters may reveal important features in the damage dynamics of single bio-particles with FEL radiation, which is difficult to realize in CDI experiments. Moreover, it covers many other interests, for example, on the interaction between solids and FELs due to the solid-like density in central area of a cluster (Ref. [45], p. 268).

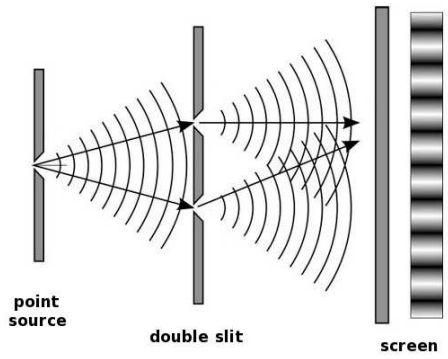

Figure 2.1: Sketch of Young's double-slit experiment. It includes all elements of CDI: coherent light wave (from the point source), 1D object of single spatial frequency (the double-slit), and proper sampling on the screen (to see the periodic pattern in the far field). The periodic pattern is connected to the object by a direct Fourier transform. The challenge for CDI is to determine the structure of the object from the measured pattern in which the diffracted wave's intensity is recorded while its accompanying phase is not.

The first single-shot CDI experiments of atomic clusters with sizes of around 100 nm were performed at FLASH. This chapter presents the analysis of the measured diffraction pattern data. As a primary step in the broader context of radiation damage study, the analysis is focused on reliable reconstructions of the cluster objects from the CDI data. The diffraction theory and related methods are applied to extract interesting information from the pattern data. In the single-shot imaging experiments, the effects of radiation damage, photon transmission and diffraction are coupled together in the irradiated clusters. The separation of the radiation damage effect is challenging and is very interesting for further study on complicated dynamics of radiation damage with FELs. This work was directed by Prof. Henry Chapman at Center for Free-Electron Laser Science (CFEL), and was in collaboration with Prof. Thomas Möller's experimental group in Technishe Universtät Berlin.

This chapter is organized as follows. § 2.2 introduces the formulation, the phase problem and its solution in CDI. § 2.3 presents an analysis of the experimental diffraction pattern data. Then detailed discussions follow in § 2.4, and finally a short summary is presented in § 2.5.

2.2 Coherent diffraction imaging

The phenomenon of coherent diffraction has a long history of revealing the nature of light waves. It is demonstrated by the famous Young's double-slit experiment, and is well described by diffraction theory. The experiment contains all of the elements of today's CDI experiments (Fig. 2.1), but the related physical problems are quite different. The former is

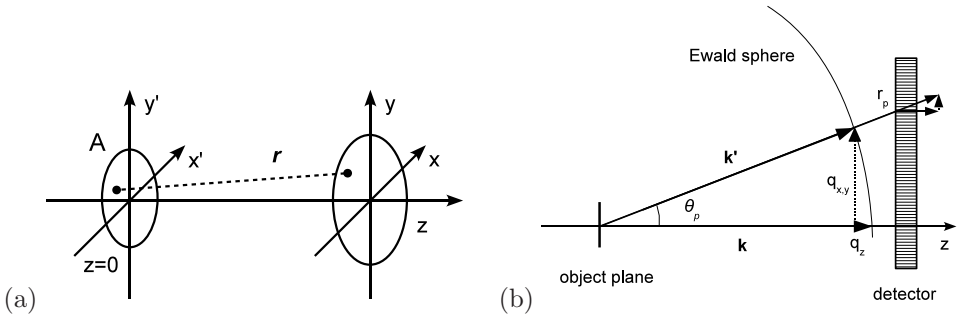

Figure 2.2: Geometries of light wave propagation and its measurement. (a) light wave propagates from a 2D aperture A in $z = 0$ plane to z plane. The aperture is transparent inside and totally opaque outside. The light wave at (x, y) in z plane is sum of propagations from each point (x', y') inside the aperture with relative distance $\mathbf{r}$. (b) A pixel ($\mathbf{r}_p$) on the detector observes intensity of a light wave forward scattered by a small aperture/object (comparing to pixel size of the detector) at scattering angle θ_p . Its wave vector is $\mathbf{k}$ before being scattered and $\mathbf{k}'$ after scattered. The Ewald sphere is a sphere with radius $|\mathbf{k}|$. The outgoing wave vector satisfies $|\mathbf{k}'| = |\mathbf{k}|$ in elastic scattering, and is on the Ewald sphere. The two geometries are connected by the scattering angle θ_p .

the forward problem to explain diffraction patterns from the structure of an illuminated object; the latter is an inverse problem to solve object's structure from the measured patterns. The idea of CDI was firstly mentioned by David Sayre (1952) [86] with the inspiration of introducing the Nyquist-Shannon sampling theorem [87] into X-ray crystallography. Important progress followed (1970s) in the algorithms helping to solve the phase problem in CDI [88, 89]. The CDI method was then experimentally demonstrated in 1999 [73].

In this section, a formulation of diffraction theory in the far field is introduced to understand the formulas of CDI, which is important for the discussions in § 2.4. The phase problem in CDI and its solutions are then briefly presented and further details may be found in the next section of data analysis.

2.2.1 Far field diffraction

Light, as a classical electromagnetic wave in media, is described by Maxwell's equations. Analytic vector solutions to these equations are difficult to obtain except in some cases of regular boundary conditions. For instance, the solution of light scattered by a uniform sphere is given by Mie theory (see § 2.4.3). In general, an approximation of a scalar wave function is employed when the spatial scale in a problem is much larger than the wavelength of light. Then Maxwell's equations can be reduced to scalar forms, which are more easily manipulated.

In the scalar approximation a light wave $U(x, y, z)$ propagating from aperture A in the $z = 0$ plane to z plane, as shown in Fig.2.2a, follows the *Huygens-Fresnel principle* (Ref. [90],

§ 4.1.2):

$$U(x,y,z) = \frac{1}{i\lambda}\int_A U(x',y',0)\frac{e^{i\frac{2\pi}{\lambda}r}}{r}\left(\frac{z}{r}\right)\,dx'dy'\,, \tag{2.1}$$

where λ is the wavelength, and the point-to-point distance $r = \sqrt{(x-x')^2+(y-y')^2+z^2} \gg \lambda$. The light wave at each point in the aperture propagates as spherical wave $e^{i\frac{2\pi}{\lambda}r}/r$ with component contribution along propagation direction (i.e. z/r factor). To simplify this equation, we assume the *Fresnel approximation*, i.e. the first order of the Taylor expansion about $r = z(1+\rho^2/2z^2+\cdots)$, where $\rho = \sqrt{(x-x')^2+(y-y')^2} \ll z$. The condition $\rho \ll z$ requires that the propagation is in forward direction within small divergent angle. This leads to the *Fresnel diffraction* formula:

$$U(x,y,z) = \frac{e^{i\frac{2\pi z}{\lambda}}}{iz\lambda}\int_A U(x',y',0)e^{i\frac{\pi}{z\lambda}[(x-x')^2+(y-y')^2]}\,dx'dy'\,. \tag{2.2}$$

The denominator r^2 in the integral (Eq. 2.1) is approximated by z^2. In the limit of the *far field approximation*: $z \gg r'^2/\lambda$ with $r'^2 = x'^2+y'^2$, the r'^2-related phase term in the exponent is neligible[1]. Hence, we obtain the *Fraunhofer diffraction* formula:

$$U(x,y,z) = \frac{e^{i\frac{2\pi z}{\lambda}}}{iz\lambda}e^{i\frac{\pi}{z\lambda}(x^2+y^2)}\int_A U(x',y',0)e^{-i\frac{2\pi}{z\lambda}(xx'+yy')}\,dx'dy'\,. \tag{2.3}$$

Elastic scattering is implicitly assumed in this diffraction theory: there is no change of wave number between incoming and outgoing waves, i.e. $|\mathbf{k}'| = |\mathbf{k}| = 2\pi/\lambda \equiv k$. All outgoing wave vectors constitute a sphere in reciprocal space, called the *Ewald sphere* (see Fig.2.2b). We are interested only in the small angle region of the forward scattering where the Fresnel approximation in Eq. (2.2,2.3) is valid. With the paraxial approximation in this region, the wave-vector transfer $\mathbf{q} \equiv \mathbf{k}' - \mathbf{k}$ can be written as (see Fig.2.2b):

$$\begin{aligned}
&q_{x,y} = k'_{x,y} = k\sin\theta_p \simeq k\tan\theta_p = kr_p/z \propto r_p\,,\\
&q_z = -k(1-\cos\theta_p) = -2k\sin^2(\theta_p/2) \simeq -k\theta_p^2/2 \simeq -q_{x,y}^2/2k\,,\ \text{or}\\
&\qquad q_z = \sqrt{k^2-q_{x,y}^2} - k \simeq k(1-q_{x,y}^2/2k^2) - k = -q_{x,y}^2/2k\,.
\end{aligned}$$

The subscript p denotes a pixel, and r_p denotes the radial position of this pixel on the detector. Note that q_z is negative. The second phase term in Eq.(2.3) becomes:

$$ik(x^2+y^2)/2z = ikz\tan^2(\theta_p)/2 \simeq ikz\theta_p^2/2 \simeq -iq_z z\,.$$

Therefore, Eq.(2.3) can be rewritten in a simple form as:

$$U(q_x,q_y,z) = \frac{e^{ikz}}{iz\lambda}e^{-iq_z z}\int_A U(x',y',0)e^{-i(q_x x'+q_y y')}\,dx'dy'\,. \tag{2.4}$$

[1] In the Fresnel diffraction regime ($z \le r'^2_{max}/\lambda$), the r'^2-related phase term is not negligible. The following derivations remain useful in this case [91]. A technique is to treat $U(x',y',0)\,e^{i\pi r'^2/z\lambda}$ as $U(x',y',0)$ in Eq. (2.2), and to separate the phase term later to obtain the true wavefield when needed.

The integral on right-hand side turns into an exact 2D Fourier transform of the aperture A. The first phase term before the integral, e^{ikz}, is x-y (the detector) plane independent, and therefore, is a trivial term. The second phase term, $e^{-iq_z z}$, depends on the x-y plane, and is a standard wave propagator along the z-direction in free space[2]. It is responsible for the defocus phenomenon which will be discussed later in § 2.4.1. It is also used for simulations of wave propagation in the *multislice method*, which is discussed in § 2.4.4. The two phase terms vanish in the measured diffraction intensity $|U(x, y, z)|^2$.

In Fig. 2.2b, a pixel, r_p, on the detector corresponds to $|\mathbf{q}| = 2k\sin(\theta_p/2)$ on the Ewald sphere, not to its component $q_{x,y} = k\sin\theta_p$, which is equal to $|\mathbf{q}|$ only in the paraxial approximation: $\sin(\theta_p/2) \simeq (\sin\theta_p)/2$. Therefore, the measured intensity may contain some limited q_z information about an experimental aperture due to the curvature of the Ewald sphere at large scattering angle[3]. Furthermore, the pixel r_p measures the z-component of the diffraction intensity at its position, and needs a correction factor of $1/\cos\theta_p$ at large θ_p.

Eq. (2.4) may be generalized to cases of 2D or 3D objects. According to Babinet's principle (Ref. [94], § 2.3.18), a 2D opaque object, complementary to the aperture A, produces the same diffracted intensity except at the origin. So far, we have discussed only the pure diffraction effect (from sharp border of a 2D aperture). For further generalization that takes into account the transmission of light in an object, we need to introduce some results from scattering theory.

In scattering theory, an incident plane wave $\psi^{(i)}(\mathbf{r}) = e^{i\mathbf{k}_i\cdot\mathbf{r}}$ elastically scattered by a potential $\varphi(\mathbf{r})$ is described by the scalar wave equation:

$$(\nabla^2 + k^2)\psi(\mathbf{r}) = -4\pi\varphi(\mathbf{r})\psi(\mathbf{r})\,. \tag{2.5}$$

A general solution to this differential equation is (Ref. [95], § 13.1.1)

$$\psi(\mathbf{r}) = \psi^{(i)}(\mathbf{r}) + \psi^{(s)}(\mathbf{r}) = \psi^{(i)}(\mathbf{r}) + \int G(\mathbf{r}-\mathbf{r}')\varphi(\mathbf{r}')\psi(\mathbf{r}')d\mathbf{r}'\,, \tag{2.6}$$

with $\psi^{(s)}$ the scattered wave and $G(\mathbf{r}, \mathbf{r}') = e^{ik|\mathbf{r}-\mathbf{r}'|}/|\mathbf{r}-\mathbf{r}'|$ the Green's function. The solution may be expanded in iterative form as the Born series:

$$\begin{aligned}\psi^{(s)}(\mathbf{r}) &= \psi^{(1)}(\mathbf{r}) + \psi^{(2)}(\mathbf{r}) + \cdots \\ &= \int G(\mathbf{r}, \mathbf{r}')\varphi(\mathbf{r}')\psi^{(i)}(\mathbf{r}')d\mathbf{r}' + \int G(\mathbf{r}, \mathbf{r}')\varphi(\mathbf{r}')\psi^{(1)}(\mathbf{r}')d\mathbf{r}' + \cdots\end{aligned} \tag{2.7}$$

[2] In the paraxial (or Fresnel) approximation, this equals: (i) $e^{ik(x^2+y^2)/2z}$, which is called the *Fresnel propagator* (in real space); or (ii) $e^{-iz(q_x^2+q_y^2)/2k}$ when moved to the left-hand side of Eq. (2.4) (in reciprocal space). The latter is the main part of the Fourier transform of (i) (refer to Eq. 2.18). Note that the wave propagates from $z_1 = 0$ to $z_2 = z$ and the z can be substituted for $\Delta z = z_2 - z_1$.

[3] Miao et al. [92] suggested a method, so-called "ankylography", to recover the q_z information by mapping a single diffraction pattern from the detector plane to the Ewald sphere. Both the non-uniform sampling and some constraints used in the literature were not well proved [93]. Extraction of the limited q_z information is still an open question.

The n-order contribution $\psi^{(n)}$, derived from $n-1$ order by propagation with the Green function, considers the effect of the light being scattered n times. If the scattering potential is very weak, i.e. single scattering process dominates, the Born series except the first order can be omitted. This is known as the *first Born approximation*. Its validity is limited by an estimated maximum phase shift [96]:

$$ka \cdot \left| \frac{4\pi\varphi(\mathbf{r})}{k^2} \right|_{max} < 2\pi c\,, \tag{2.8}$$

where a is the typical radius of the potential and c is a constant around 0.2. In the far field ($|\mathbf{r}| \gg |\mathbf{r}'|$), $|\mathbf{r}-\mathbf{r}'| \simeq r - \hat{\mathbf{r}}\cdot\mathbf{r}'$, the scattered wave in the Born approximation becomes

$$\psi^{(s)}(\mathbf{r}) = \frac{e^{ikr}}{r} \int \varphi(\mathbf{r}') e^{i\mathbf{q}\cdot\mathbf{r}'} d\mathbf{r}'\,, \tag{2.9}$$

with $\mathbf{q} = k\hat{\mathbf{r}} - \mathbf{k}_i \equiv \mathbf{k}_s - \mathbf{k}_i$. The integral on the right-hand side, called the *scattering amplitude*, is a Fourier transform of the potential. When the light wave is scattered by a *weak* 3D object (*weak* means transparent to the light with small phase variance as it will be defined soon), the amplitude of the potential function $\varphi(\mathbf{r})$ is proportional to its electron density. Within the range of small angle forward scattering (paraxial approximation), the factor of the spherical wave before the integral has the form:

$$\frac{e^{ikr}}{r} \simeq \frac{1}{z} e^{ikz(1+\rho^2/2z^2)} \simeq \frac{ikz}{z} e^{ikz\theta_p^2/2} \simeq \frac{ikz}{z} e^{-iq_z z}\,.$$

If the object is thin in the z direction, the Fourier transform in Eq. (2.9) can be reduced to a 2D representation:

$$\psi^{(s)}(q_x, q_y, z) = \frac{e^{ikz}}{z} e^{-iq_z z} \int \tilde{\varphi}(x', y') e^{i(q_x x' + q_y y')} dx' dy'\,, \tag{2.10}$$

where $\tilde{\varphi}(x', y') = \int e^{iq_z z'} \varphi(\mathbf{r}') dz'$ is the 2D transmission projection of the weak object. For a pure 2D object $\varphi(x', y') = \varphi(\mathbf{r}')\delta(z')$, the equation (2.10) has exactly the same form as Eq. (2.4). Note that Eq. (2.9) is not limited by the requirement of small angle scattering.

A 3D object may be regarded as a medium with the same volume that the incident plane wave penetrates. This is described by the Helmholtz equation

$$(\nabla^2 + n^2 k^2)\psi = 0\,, \tag{2.11}$$

with the refractive index of the medium $n = c/v = \sqrt{\varepsilon\mu/\varepsilon_0\mu_0} = \sqrt{\varepsilon}$. If the dielectric medium is homogenous, i.e. $\varepsilon(\mathbf{r}) = const.$, the wave solution for the medium is simply a planar wave: $e^{in\mathbf{k}\cdot\mathbf{r}}$. This solution will be used for later discussion in § 2.4.2. If the permittivity $\varepsilon(\mathbf{r})$ is not spatially uniform, the equation can be solved as the scalar wave equation Eq. (2.5) with

$$\varphi(\mathbf{r}) = \frac{k^2}{4\pi}\left(n^2(\mathbf{r}) - 1\right) = \frac{k^2}{4\pi}\left(\varepsilon(\mathbf{r}) - 1\right)\,. \tag{2.12}$$

Note that the scalar wave approximation in Eq. (2.11) implicitly assumes (Ref. [95], § 13.1.1): the variation of $\varepsilon(\mathbf{r})$ is relatively flat on the scale of the wavelength. The complex index of refraction $n = 1-\delta+i\beta \equiv 1+\delta n$. For a weak object $|\delta n| \ll 1$, $n^2 \simeq 1+2\delta n$. The scattering potential

$$\varphi(\mathbf{r}) = \frac{k^2}{2\pi}\,\delta n = \frac{k^2}{2\pi}\,(-\delta(\mathbf{r}) + i\beta(\mathbf{r}))\ . \tag{2.13}$$

corresponds to a complex object. The real part leads to a phase shift of the incident wave, and the imaginary part to absorption. When the size condition derived from Eq. (2.8) is satisfied,

$$a < a_0 \equiv \frac{\lambda c}{2|\delta n(\mathbf{r})|_{max}}\,, \tag{2.14}$$

the object is called *optically thin* (or *weak*), which is the requirement for the first Born approximation. The condition is usually satisfied in the hard X-ray regime where relative refractive index of matter is quite small.

For an optically thick object, the multiple scattering process is dominant, and structural information about the object which the scattered photons carry is no longer straightforward. Instead of the object is the *exit surface wave* of the illuminating light after interaction with the object. This occurs to objects with strong phase variance, also to those with strong absorption where light may not penetrate. This situation occurs often in the soft X-ray regime where absorption edges of atoms are often probed. A simulation tool of the exit surface wave is the *multislice method*, which assumes a single scattering process is dominant in each slice of the object along the illumination direction. This assumption is valid when the thickness of each slice approaches the infinitely small. In the current work, the relevant wavelength is in the soft X-ray regime (13.8 nm). Further datails about the multislice method are discussed in § 2.4.4.

This section has shown the formulas: Eq. (2.4) for 2D and Eq. (2.9) for 3D, which are derived for the coherent diffraction imaging in the far field. A Fourier transform connects the object (or exit surface wave) in real space to the diffracted intensity measured in reciprocal space. The assumption of plane waves in their derivations requires a monochromatic and coherent light source[4], which can be extended to matterwaves such as electron diffraction and neutron diffraction. This work is focused on CDI with an FEL source.

2.2.2 Phase problem

Since only the photon intensity is recorded by a detector, such as a charge-coupled device (CCD), the phase information contained in the wavefront at the detector plane is lost[5],

[4]Polarization of the light is not necessary. The Thomson scattering from a single electron contributes a polarization factor to the scattered intensity: $\cos^2\theta_p$ for linear polarization perpendicular to the beam; 1 for parallel to the beam; and $(1+\cos^2\theta_p)/2$ for the unpolarized case.

[5]Some imaging techniques like holography or grating interferometry, with the benefit of a known structure reference (such as a point, line, or phase grating), can encode the phase information of objects into the measured intensity on a detector. These techniques are beyond the scope of this work.

and hence the object cannot be recovered directly by an inverse Fourier transform of the measured data, as indicated by Eq. (2.4,2.9). This problem is called the *Phase Problem*. The missing phases could be retrieved if the measured intensities are correctly sampled [97, 98]. This is related to the following sampling theorem.

The Nyquist-Shannon sampling theorem [87] states that a 1D signal with maximum frequency B can be completely determined by sampling at the Nyquist rate ($2B$) or larger. If we use sampling rate $2B' < 2B$, then the information at high frequencies $f > B'$ will be lost, and be transfered into artificial low frequencies, known as "aliasing". It is straightforward to extend this treatment to the 2D or 3D case: the minimum sampling factor (sampling rate over maximum frequency) is two for each dimension.

Sayre [86, 99] pointed out the possibility to image a single unit cell in crystallography through the proper sampling of a continuous diffraction intensity in reciprocal space. Assume that a 2D complex object has a size of $M \times M$ pixels, corresponding to $2M^2$ independent real elements. In CDI, its diffraction pattern is measured with resolution size $N \times N$. The ratio of pattern size over object size $\alpha = N^2/M^2$ is called the *oversampling* factor. This factor may be estimated directly from a diffraction pattern by observing its inverse Fourier transform (i.e. autocorrelation) [100]. The phase problem, in a sense, is a problem to solve $2M^2$ independent variables of real values from N^2 real equations indicated by the Fourier transform in Eq.(2.4). For the problem to be solvable, an overdetermining condition $\alpha > 2$ is necessary[6]. This oversampling factor is important in the phasing process. Normally, a pattern sampled with the Nyquist rate satisfies the oversampling condition ($\alpha = 2^n$ for n-D case). If a diffraction pattern is undersampled, it is still possible to retrieve phases after interpolating the measured pattern to a larger resolution size required[7] [98]. However, such a phase retrieval based on the undersampled pattern may induce some unreliable features in a reconstructed object due to the missing of low spatial frequencies (i.e. high frequencies in reciprocal space), as the sampling theorem says[8].

The phase problem is to solve an object from measured intensity pattern. It is an *ill-posed* inverse problem in diffraction theory, because it has an unknown number of independent variables (i.e. M^2) and no unique solution (some global uncertain degrees, refer to § 2.3.2). A solution to the *analogical* (and nonlinear) equations mentioned above might be mathematically acceptable, but should be physically unacceptable due to the noises presented in the measurements [101]. A physical solution is always an approximate one and requires sufficient

[6] In practice, it depends on size of the object support, missing data in beamstop or pattern defects, etc. On the other hand, some global degrees of freedom of reconstructed object are uncertain, such as constant phase, or conjugation, which will be discussed later.

[7] The interpolation does not change maximum scattering angle in the pattern, which determines the object resolution in real space (i.e. M^2 is unchanged). Therefore, the oversampling ratio α can increase in this way.

[8] The cases with oversampling ratios less than 2^n (but larger than 2) for n-D objects have been discussed in [97]. It may be possible for certain distribution of spatial frequency in 2D or 3D objects. It could be interesting to compare consistence of information contained in a diffraction pattern recorded with different oversampling ratios.

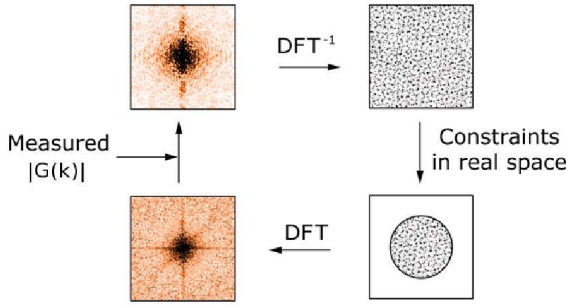

Figure 2.3: Basic iterative algorithm for phase retrieval. Constraints in real space are: object support, real and positive values of object, etc. In reciprocal space, generating phases are kept, but amplitudes are replaced by the measured ones as constraints.

and consistent information contained in the pattern. The pattern should be of high signal-to-noise ratio and proper oversampling. The *prior* knowledge or constraints from physical considerations do help to approach the physical solution. The methods to solve the phase problem are introduced in the following part.

2.2.3 Phasing method

To retrieve the missing phases is a nonlinear optimization problem. It may be solved through an iterative method: to find out the solution that best fits all constraints in both *direct* and *Fourier space*.

Before introducing the method, the meanings of some items will be clarified. In following discussions, the phases of *real space* and *reciprocal space* are used instead of *direct space* and *Fourier space* respectively. A *support* of an object is a binary matrix defining which pixel belongs to the object. It is a physical constraint in real space and can be pre-defined or achieved from an algorithm which will be mentioned soon. A *beamstop* is zero-intensity area in centre of a measured diffraction pattern where the incident laser beam is stopped to protect the detector. A *mask* is a binary matrix defining which pixel is reliable in the pattern. It defines where the constraint of measured intensity should be applied in reciprocal space. In numerical processing of images, the discrete Fourier transform (DFT) is used instead of its continuous form in the formulation above.

The iterative method, as illustrated in Fig.2.2.3, works back and forth in real and reciprocal space and approaches the solution that best satisfies all defined constraints. The basic algorithm is:

(1) apply random phases to the measured diffraction amplitude;

(2) generate corresponding complex-value object via inverse DFT of the new complex-value pattern;

(3) apply constraints in real space: reduce nonzero pixels outside object support to zero; or reduce imaginary part or negative values inside object (depending on type of object in problem), and so on;

(4) generate complex-value pattern via DFT of the new object after being constrained;

(5) apply modulus constraints in reciprocal space: replace the amplitude with measured one in masked (reliable) pixels, and keep the phases for next iteration;

(6) repeat steps (2-5) to obtain proper phasing results within acceptable errors.

There are some detailed algorithms used in the step (3): Error Reduction (ER) [88], Hybrid Input-Output (HIO)[89], Relaxed Averaged Alternating Reflectors (RAAR) [102]. These algorithms only present different ways to reduce the pixels that dissatisfy support constraint in real space:

$$g_{n+1}^{\mathbf{ER}}(x) = \begin{cases} P_{_M}\, g_n(x)\,, & x \in S\,; \\ 0\,, & x \notin S\,. \end{cases} \tag{2.15}$$

$$g_{n+1}^{\mathbf{HIO}}(x) = \begin{cases} P_{_M}\, g_n(x)\,, & x \in S\,; \\ (I - \beta P_{_M})\, g_n(x)\,, & x \notin S\,. \end{cases} \tag{2.16}$$

$$g_{n+1}^{\mathbf{RAAR}}(x) = \begin{cases} P_{_M}\, g_n(x)\,, & x \in S\,; \\ [-\beta I + (1-2\beta) P_{_M}]\, g_n(x)\,, & x \notin S\,. \end{cases} \tag{2.17}$$

The $g_n(x)$ is an estimated object at the nth iteration, S the support, and β a feedback parameter (with an experience value of around 0.9). The operator $P_{_M} \equiv \mathcal{F}^{-1}\mathcal{P}_{_M}\mathcal{F}$, with Fourier transform $\mathcal{F}$, is the projection operator in real space, after applying the modulus constraint $\mathcal{P}_{_M}$ in reciprocal space. In this work, both algorithms HIO and RAAR are applied separately in combination with ER (one ER iteration every 20 iterations of HIO/RAAR). There are some other similar algorithms that are not used in this work: Hybrid Projection Reflection (HPR) [103], Charge Flipping (CF) [104, 105] and Difference Map (DM) [106]. The convergence behavior of all these algorithms during iterations is quite different and depends on problems [107].

Usually the support constraint of an object is fixed during iterations. It can be estimated from the autocorrelation image, or a *priori* knowledge of the object's shape. The estimated support may be loose or inaccurate, and limits the reconstruction quality (e.g. defocused object is obtained as discussed in § 2.4.1).

The "Shrinkwrap" algorithm [108] iteratively generates a tight support. It begins with an initial support, estimated from the autocorrelation images (direct inverse Fourier transform

of diffraction pattern), or even a simple rectangular support. During the iterative procedure, a new support is estimated by the amplitude of a new object above a constant ratio threshold, and updated every certain numbers of phasing iterations. To generate the new support, the amplitude is blurred through a convolution with a Gaussian kernel which has, typically, a decreasing width as the number of iterations increases. The support may gradually shrink to a compact and stable one. This tight support can be used as a fixed support for further fine reconstructions.

The support generated from this process depends on the quality of the pattern data. Information about the shape of an object could be lost due to a large beamstop or very noisy pixels at area of low spatial frequency. Its advantage is to avoid the requirement of a prior knowledge of the object shape, and to improve the reconstruction quality. However, this becomes difficult in the case of an object with low border-contrast or a dilute density.

The solutions obtained from the iterative method are not unique. There are some global uncertainties due to the limited information in the diffraction patterns measured (see § 2.3.2). Furthermore, some solutions may correspond to local minimums to all constraints, and therefore, they are not the best solutions. It is difficult to define the global minimum for a solution in such a complex and nonlinear phase space. A practical way is to compare the solutions from many independent phase retrievals. Reliable solutions can be achieved statistically by average of these independent phasing results with respective confidences. In this post-processing, the trivial inconsistencies among independent results need to be removed before a meaningful average, as discussed in § 2.3.2. Finally, the reconstructed object images are obtained through inverse Fourier transform of the retrieved complex diffraction pattern.

Iterative methods to solve the phase problem have been applied successfully in many important single particle imaging experiments [73, 77, 75, 54, 78].

2.3 Imaging of atomic clusters

2.3.1 Imaging experiments

The first cluster imaging experiments have been performed at the FLASH facility at DESY by Prof. T. Möller and collaborators, who kindly provided the unpublished data to the author for the purposes of this analysis. The atomic clusters, the size of which is controlled by gas pressure, were injected into the focus area of a linearly-polarized Free Electron Laser (FEL) beam (Fig.2.4). After each FEL pulse, the diffraction signals scattered from the clusters were recorded by a detection system. In the detection system, a microchannel plate (MCP) and a phosphor screen were applied to transfer the recorded VUV photon signals into visible light which a charge-coupled device (CCD) camera can detect. The FEL pulses were so intense that the camera pixels aligned with the direct beam usually needed a beamstop on front for protection. In Fig.2.4, a planar mirror with a small central hole was applied to protect the CCD camera, and the beam passing the hole was stopped by a beam dump.

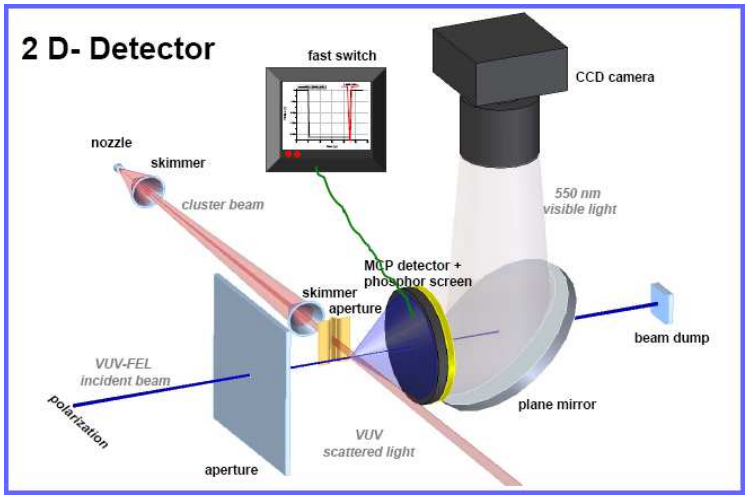

Figure 2.4: Setup of the cluster imaging experiments (illustration provided by T. Möller). The single VUV FEL pulses interact with the incoming beam of cluster objects. The signals of forward scattered photons are transfered into visible light before being recorded by the CCD camera.

Table 2.1: Parameters for the single-shot imaging experiments.

gas cluster	xenon
cluster diameter	50−150 nm
wavelength	13.8 nm
pulse duration	10 fs
focus intensity	$10^{12} - 10^{14}$ W/cm^2
sample-detector distance	23.58 mm
size of a pixel on detector	0.124 mm
number of pixels on detector	696×520

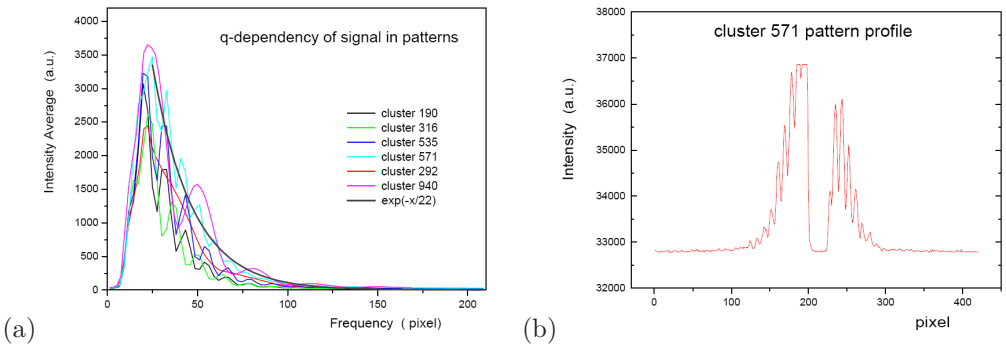

Figure 2.5: The quality of the diffraction pattern data: (a) q-averaged pattern intensity with minimum value subtracted, and (b) a central profile of `cluster 571`.

The parameters used in the experiments are listed in Tab. 2.1. The sizes of cluster objects are 3 to 11 times as long as the FEL wavelength which is 13.8 nm. The single pulses are ultrashort (ten femtoseconds) and very intense (10^{12-14} W/cm^2) within focus spot of tens micrometers. The maximum scattering angle in the measurements is 48° at middle edge of the detector. The diffraction patterns measured in the experiments are of good quality. The number of clearly-defined fringes can be up to 8 (`cluster 571`) as shown in Fig. 2.5(a) and Fig. 2.7. These intact fringes contain information for the reconstruction of the objects. However, from the central profile of a single pattern in Fig.2.5(b), we can see a very large background, almost 90%, which may come from the complex detection system. After subtracting a background intensity estimated by the minimum value, as Fig. 2.5(a) shows, the patterns have rare counts outside the radius of 100 pixels, corresponding to the effective scattering angle of around 25°.

Here, only three typical patterns are chosen for reconstruction (Fig.2.7): `cluster 571/940/292`. Since the effective scattering angle is small, the pattern size 420×420 is chosen for `cluster 571`, and 340×340 for `cluster 940/292`. The oversampling ratios estimated from autocorrelations in these cases are larger than ten in each dimension. This can be verified from the pixel sizes of reconstructed objects (Fig. 2.12-2.14). The phasing method mentioned in § 2.2.3 is applied to retrieve the phases of these patterns.

2.3.2 Phase retrieval process

This part will present several questions existed in the phasing processes of the chosen diffraction patterns. A complete phasing process in this work, as illustrated by a flowchart in Fig. 2.6, generally includes following steps: (i) subtract background signals, and prepare a mask for the diffraction pattern; (ii) determine the guess of initial object support from the object autocorrelation (inverse Fourier transform of the diffraction pattern, and area of its amplitude above a threshold is a rough guess of support, which is generally two times larger

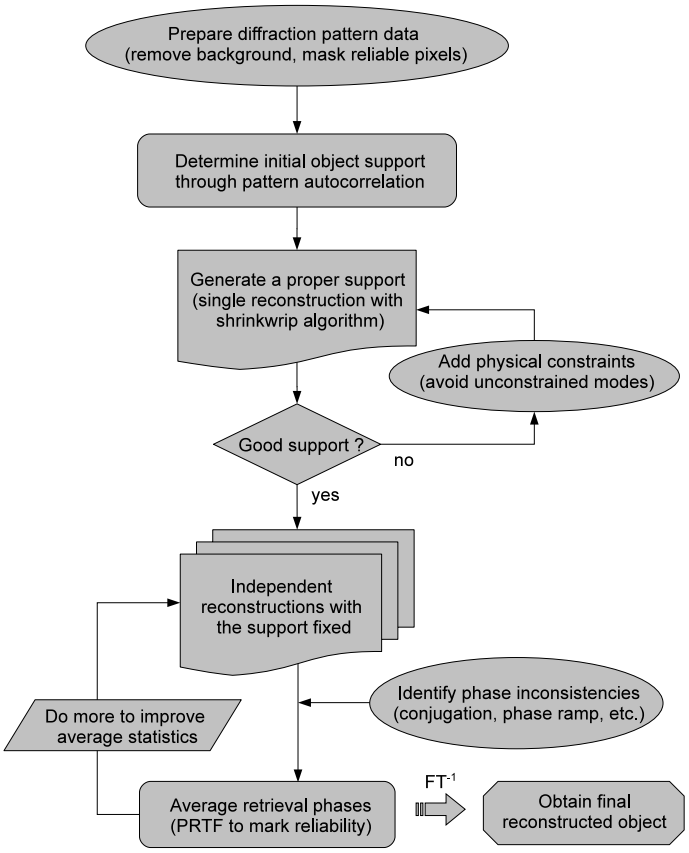

Figure 2.6: Flow chart of a complete reconstruction process for a diffraction pattern. The independent reconstructions are applied to achieve a statistically reliable result, which is described by a phase retrieval transfer function (PRTF, see § 2.3.3). The oval parts are discussed as subtopics in the text.

than object in each direction due to the property of autocorrelation); (iii) use the iterative phasing method and the "Shrinkwrap" algorithm to generate a tight support of object, and probably need physical constraints to improve the support; (iv) use the iterative method with the fine support fixed to retrieve phases for the diffraction pattern, many times and independently; (v) average the independent phasing results to obtain a complex diffraction pattern with statistical confidence, which is defined by a phase retrieval transfer function (PRTF, see § 2.3.3); and (vi) the final reconstructed object is an inverse Fourier transform of the complex diffraction pattern. Here, only specific issues in the steps (i, iii, v) are concerned. These issues are presented as subtopics (see the ovals in the flowchart): (1) for step (i); (2) for step (iii); and (3-5) for step (v).

Before the subtopics, a few words about the step (iv, v) will help to understand the context of the (3-5). The strategy behind the two steps is to "sample" solution space (randomly) by independent reconstructions, and obtain statistically best solution by averaging over the "sampling points" (uniform) in solution space. The more the "sampling points", the more reliable the averaging solution. The independence in reconstructions is realized through uncorrelated start points of initialized phase in the iterative method. Before averaging over the independent phase results, some inconsistencies and uncertainties among these phase results need to be identified. Otherwise, the average becomes meaningless. The

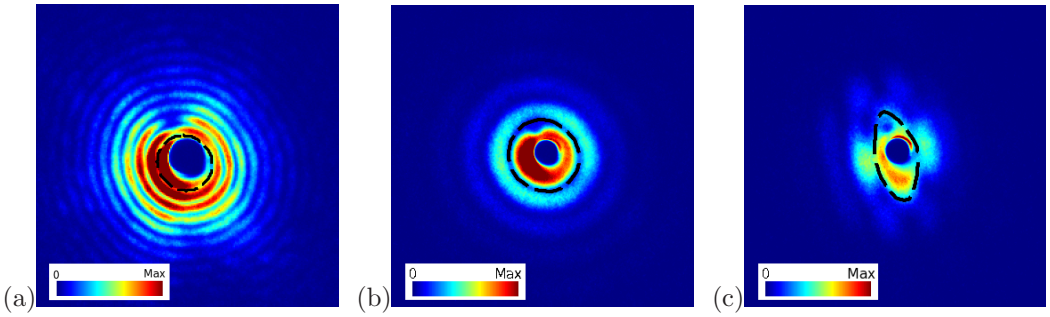

Figure 2.7: Diffraction patterns from cluster imaging experiments. (a-c) correspond to `cluster 571/940/292` with background subtracted. Central holes are beamstops. Dashed black closed-curves indicate unreliable area in the patterns.

(3-5) discuss the relevant inconsistencies. Some global degrees of freedom are still uncertain: a overall constant phase, absolute position of object and conjugation state of object, etc. These uncertainties lead to non-unique solutions in the complete phasing processes. Fortunately, these uncertainties do not compromise the structural information about the objects in the reconstruction results. The statistical confidence of the final phase result after averaging is defined by PRTF in the next part.

(1) Pattern preparation

Signals from the experimental background may lead to the nonzero minimum in the measured pattern (Fig.2.5b). The background that has to be subtracted can be estimated by an additional measurement when beam is switched off (known as dark image), or simply by the minimum value in the pattern (as used here). Due to the high laser intensity near the beam axis, a beamstop is applied to avoid detector damage, and therefore there is no photon counting in this pixel area. In some pixels, photon counting is probably saturated, i.e. it exceeds the counting (dynamic) range, and is then not reliable. These pixel areas, along with defect speckles or fringes, have to be excluded in a pattern *mask*, a binary matrix which defines the reliable counting area (Fig.2.7). Since the effective scattering angle is small ($\sim 25°$), the scattering-angle-related corrections of the pattern intensity are not considered, such as the linear polarization factor of FELs and component measurement on the detector, which are mentioned in § 2.2.1.

(2) Unconstrained modes

In the step (iii), a problem of the unphysical modes appears in a reconstructed object, which aims to generate a tight support. It comes from the limited constraints in reciprocal space due to large size of beamstop. A Gaussian mode $g(x) = e^{-x^2/2\sigma_x^2}$ in Fourier space

becomes: (for simplify, only 1D formula is shown in following part.)

$$G(k) = \int g(x)\, e^{ikx}\, dx = \sqrt{2\pi}\sigma_x e^{-\frac{k^2}{2}\sigma_x^2} \propto e^{-\frac{k^2}{2\sigma_k^2}}\,, \tag{2.18}$$

where $\sigma_x \cdot \sigma_k = 1$. The Gaussian mode remains mainly in 1σ area of radius σ_x in real space and σ_k in reciprocal space. During phasing iterations, the constraints of object support and pattern mask work only on pixel area outside the object support in real space and the beamstop in reciprocal space. When the support or beamstop is large, the Gaussian mode, probably together with a finite number of higher-order harmonic modes, may survive under the constraints. The eigenstates of these modes can be simulated given certain shapes of the support and the beamstop [77]. In practice, the condition for the existing modes in 2σ area can be estimated as[9]

$$S_x \cdot B_k \gtrsim \frac{2N}{\pi}\,, \tag{2.19}$$

with pixel radius of support S_x, pixel radius of beamstop B_k, and pattern resolution size $N \times N$. In our example of `cluster 571` (Fig.2.8), $S_x \cdot B_k \cdot \pi/2N \simeq 1.8$, the condition is satisfied[10]. The cluster object may contains at least one unphysical Gaussian mode. Due to the limit of constraints mentioned above, the weight coefficients of these unphysical modes in a reconstructed object can be arbitrary, and mixed with ones which constitute the realistic object. Hence, it is difficult to subtract all of the unphysical parts of the modes from the phasing result. Authors in [77] suggested an artificial way to reduce such uncertainty by minimizing the object variance from the complex average in the support. But a better solution may be to include finer constraints from physical considerations.

Here, a *priori* knowledge is applied in order to avoid the unexpected modes. The atomic clusters are *optically thick*, and only few photon penetrates through central part of a cluster object. The amplitude nearby the object's center should be close to zero, causing a ring structure (see § 2.4.2). A central hole, with a size smaller than the expected ring structure (Fig.2.8c), is added to the support obtained from the "Shrinkwrap" algorithm. The ring structure of the support can significantly reduce the unphysical mode effect in the reconstructions (Fig.2.12).

(3) Complex conjugation

This issue, together with following (4,5), is critical for meaningful average in the post-phasing step (v). When an object is complex, its conjugation changes only the diffraction

[9] The condition results from $\sigma_x \cdot \sigma_k = 1$, and depends on the definition of Discrete Fourier Transform (DFT). Usually, in the `fft` (Fast Fourier Transform) or `fftw` programs, its 1D form is defined as $F(k) = \frac{1}{N}\sum_x f(x)\, e^{-i2\pi kx/N}$. It corresponds to $\sigma_x \cdot \sigma_k = N/2\pi$.

[10] It is possible to break the mode condition by cutting the pattern to low scattering angle, i.e. low spatial resolution, and binning pixels to decrease oversampling rate; because $S_x \propto 1/d_m = 2\sin(\theta_m/2)/\lambda \propto \tan(\theta_m/2) \propto N$, and $B_k \propto N$ (with d_m maximum spatial resolution and θ_m maximum scattering angle). But here it is impossible due to small number of pixels inside the object.

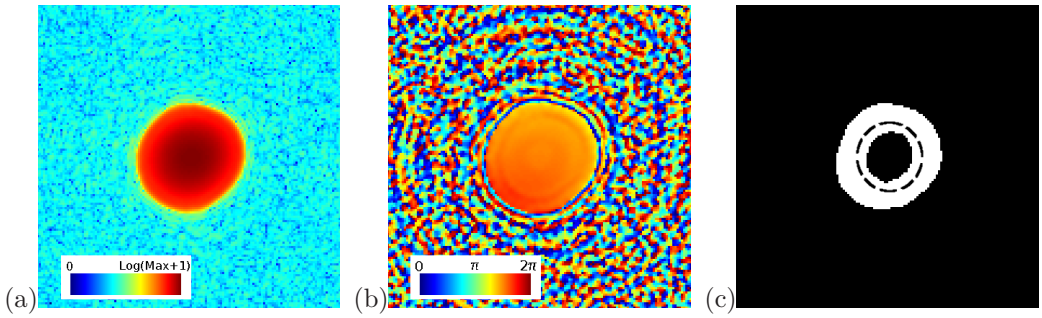

Figure 2.8: A reconstruction result of `cluster 571` with modes. (a) object amplitude, containing at least one Gauss mode. (b) object phase, which is almost flat. (c) modified support (white area) with a priori knowledge to reduce possible modes. The size of the inner removed range is smaller than the expected attenuation area indicated by the dashed circle. The reconstruction results based on this new support are shown in Fig.2.12.

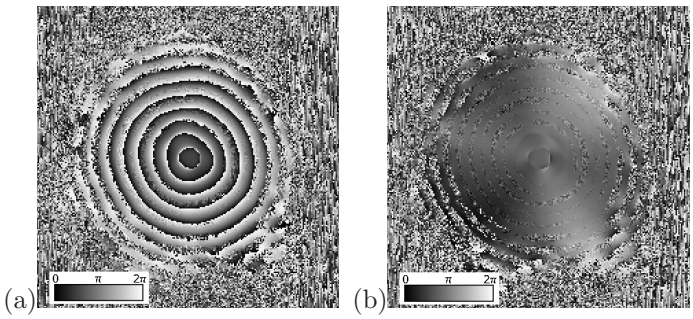

Figure 2.9: Conjugation relation between two independent phasing results. (a) phase difference between them: phase circle structure comes from 2π modulation, and corresponds to the doubled single phasing result. (b) their phase average, equal to phase difference after conjugating one of them.

phase, not the diffracted intensity, in reciprocal space. Therefore, diffraction patterns cannot recognize if it is the object measured or its conjugation. The uncertainty of complex conjugation permits a reconstruction result chosen as a reference without consideration of its conjugation state. Retrieval phases in another independent reconstruction may be conjugated with the reference, as showed by the phase difference in Fig.2.9. The conjugation has to be reduced before averaging with the reference. Practically, an additional point reflection in real space is necessary before averaging the objects, because

$$\tilde{g}(x) \equiv \int G(k)^* \, e^{ikx} dk = \left(\int G(k) \, e^{ik(-x)} dk \right)^* = g(-x)^* \, . \tag{2.20}$$

The conjugation state of object is one of global uncertainties in the reconstructions.

(4) Phase vortices

In some cases, phase difference has a vortex structure centered at zero frequency (Fig.2.10).

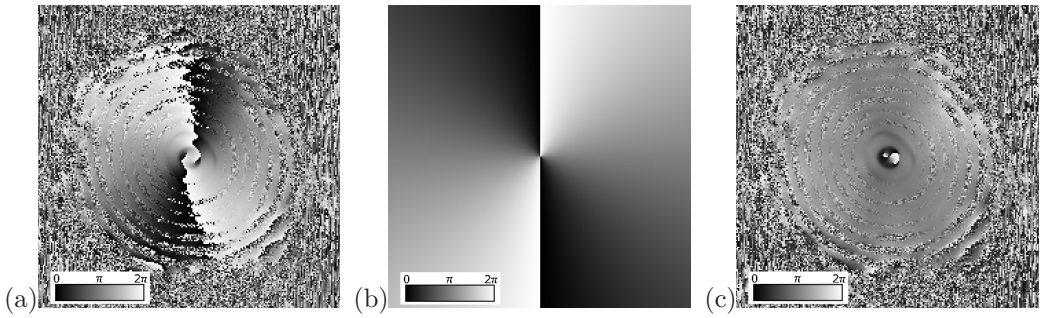

Figure 2.10: Vortex structure found in phase difference between independent phasing results. (a) a phase difference with two left-hand vortices (i.e. phase jumps two times due to 2π modulo); (b) an artificial phase with two right-hand vortices. (c) phase result after combining (a) with (b) by a complex multiplication.

The vortex is a spiral structure with integer times of 2π in a phase matrix. The integer corresponds to the number of vortices, which have two possible spiral directions (left- or right-hand). In practice, this can be reduced by multiplying an artificial phase with the vortex in the inverse direction. The structure might be related to the initialization of random phases, and the constraints during phasing iterations. However, the questions, where the structure comes from and how to describe it mathematically, are not fully understood [109]. In this work, a reconstructed object without vortex structure is chosen as a reference due to its unphysical features (similar structure in real space) produced by the structure.

(5) Phase ramp

When an object $g(x)$ is shifted by x_0 pixels in object plane, with a constant phase δ, the object in Fourier space

$$\tilde{G}(k) \equiv \int \left[g(x+x_0)e^{i\delta}\right]\, e^{-ikx}dx = e^{i(kx_0+\delta)}\, G(k)\,. \tag{2.21}$$

The phase shift along k pixel direction is linear, which is called "phase ramp" (Fig.2.11). The phase ramp, i.e. position shift of the object and a constant phase, does not change the measured intensity $|G(x)|^2$, and therefore, is uncertain in phasing process. In practice, the centre of the object support should be shifted to centre of the reconstruction image[11]. When overlap in an achievable accuracy of one pixel at least, two reconstructed objects may have a discrepancy of phase ramp, of 2π at most, over whole image plane (i.e. $i2\pi x \cdot 1/N$ in DFT). After averaging over many independent reconstructions, this phase discrepancy caused by object shift of less one pixel can be significantly reduced. For small objects which has a width of few pixels covered by the ramp, the phase discrepancy could be negligible.

[11]Sometimes the object centre has to be shifted to the corner of the image. It depends on the definition of the origin in the Fourier transform program used. In the same way, the central shift of diffraction pattern in the reciprocal space can cause phase ramp in the object (real space).

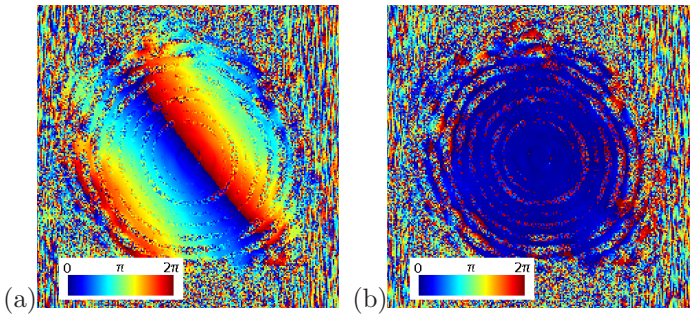

Figure 2.11: Phase ramp in a phase difference. (a) colorful strips show phase ramp due to the relative shift of two objects in real space. (b) phase difference after adjusting position of one object and subtracting the constant phase discrepancy. It becomes close to 0 (or 2π).

Therefore, higher-order (e.g. quadratic) correction [109] of this phase ramp within one-pixel accuracy of object overlapping is not considered here.

2.3.3 Phasing results

This part will present the phasing results on the three diffraction patterns. Before it, the definition of resolution in the results needs to be clarified. From the Bragg's law, the perfect resolution in real space for a diffraction pattern is

$$d_m = \frac{\lambda}{2\sin(\theta_m/2)}\,, \tag{2.22}$$

where θ_m is maximum scattering angle defined by middle point on pattern edge. The different resolution sizes are used: 420×420 for `cluster 571`, 340×340 for `cluster 940/292`. The perfect resolution is: $d_m \simeq$17.0 nm and 19.3 nm respectively. The actual resolution in reconstructed objects is smaller than this perfect one. The pixel size in real space is half of d_m due to sampling requirement for spatial frequencies. Reliability of the retrieved phases may be described by *phase retrieval transfer function*:

$$\mathrm{PRTF} = \left\langle \frac{G(x,y)}{|G(x,y)|} \right\rangle_n\,, \tag{2.23}$$

with x, y pixel indices in the patterns. Phases retrieved in the n independent reconstructions are averaged. If the phase of one pixel varies randomly, then the modulus of the complex average on this pixel is zero; if all phases are same, it becomes one. The PRTF matrix marks reliable phases with corresponding confidences at each pattern pixel. Its dependence on spatial frequency q is one of effective ways to define the resolution limit in reconstructions.

The phasing results are briefly listed below. The discussions in detail on these results are presented in the next section. Note that the definition of spatial frequency is $q = 1/d$ in Fig. 2.15. It uses the same convention with $k = 1/\lambda$, instead of $k = 2\pi/\lambda$ used in all formulas.

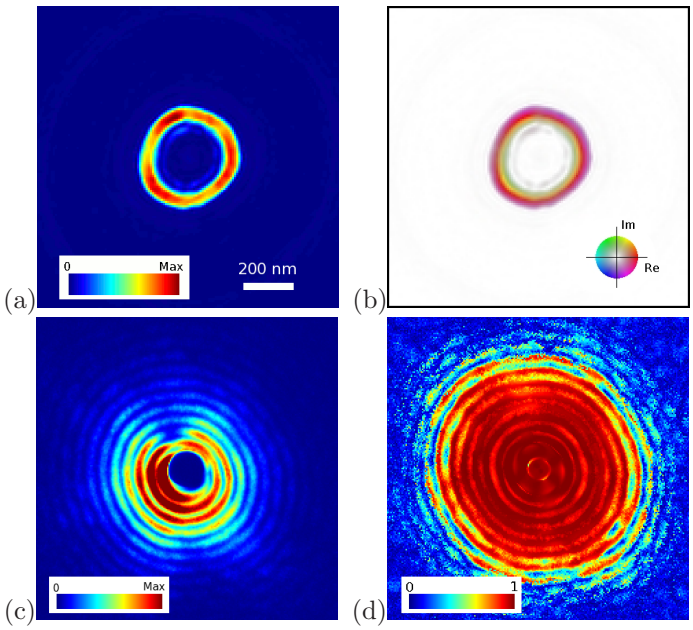

Figure 2.12: Averaged results of `cluster 571` reconstructions. There were 100 independent reconstructions performed. (a) object amplitude, the size is about 370 nm in diameter. (b) object phase, phase shift in the object is $\sim 90^{\circ}$. (c) diffraction pattern data, the minimum intensity has been shifted to zero. (d) PRTF matrix, that shows the reliability of retrieval phases.

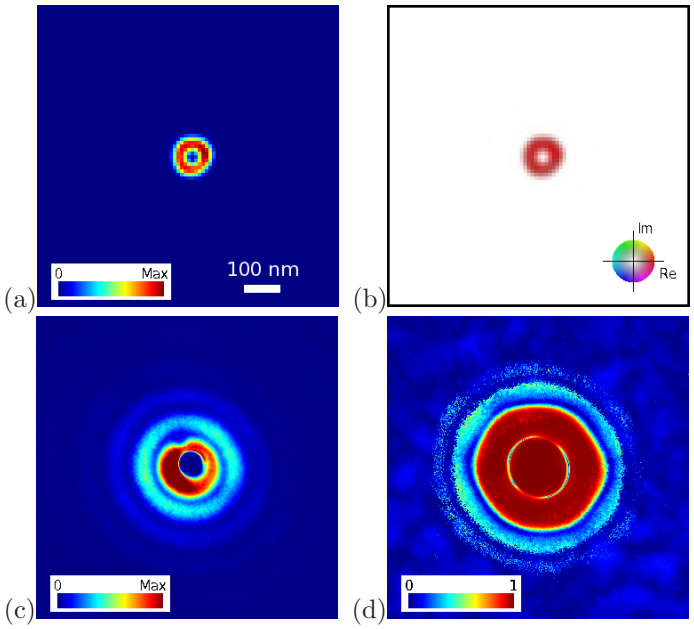

Figure 2.13: Averaged results of `cluster 940` reconstructions. 300 independent reconstructions were performed. (a) object amplitude, the size is about 90 nm in diameter. (b) object phase, phase shift in the object is less than 10°. (c) diffraction pattern data. (d) PRTF matrix.

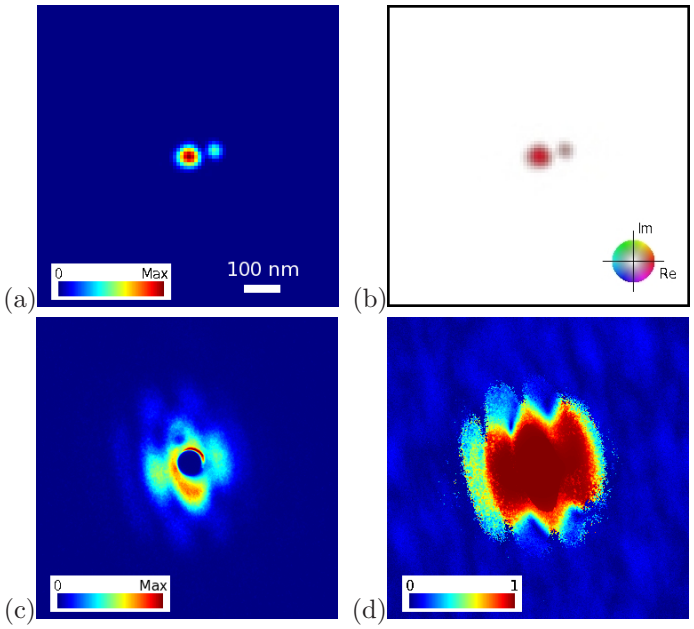

Figure 2.14: Averaged results of `cluster 292` reconstructions. 300 independent reconstructions were performed. (a) object amplitude, two separate clusters stay on different object planes. (b) object phase, phase shift in the big one is $\sim 10°$. (c) diffraction pattern data. (d) PRTF matrix.

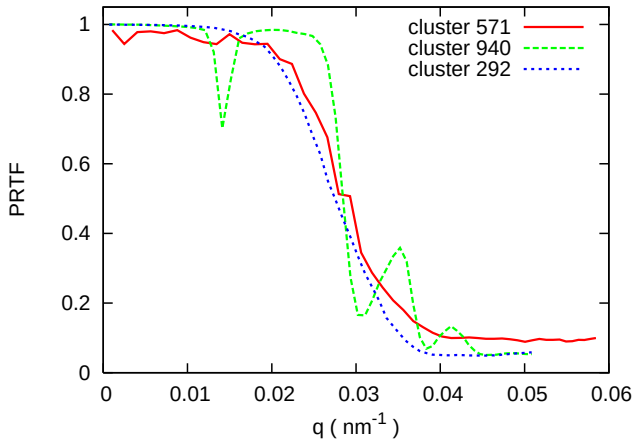

Figure 2.15: The q-averaged PRTF to show resolution limits in the reconstructions. The resolution limits is estimated to be around 25 nm (at $q = 0.04$ nm^{-1}, convention see text).

`Cluster 571` (Fig.2.12)

The fixed support with ring structure (Fig.2.8c) is used for about 100 independent reconstructions. From the average of these reconstructions, the irregular ring shape of the cluster can be seen (see Fig. 2.18 for details of the ring structure). The cluster image size is about 370 nm in diameter. The gradual phase shift can be observed on the ring structure. The total phase shift is estimated to be larger than 90°. The PRTF function shows the reliable phase retrieval that can reach 7th fringe. The resolution limit is about 25 nm (Fig.2.15).

`Cluster 940` (Fig.2.13)

In the support of this object, only one central pixel is removed to avoid unphysical modes, while the hole in the reconstructed object is 3 pixels large. The cluster image size is about 90 nm. The ring structure with such a small hole indicates that the penetration length of the FELs in the clusters could be less than the cluster size. The object phase is quite flat, and the shift is less than 10°. The PRTF function shows that the resolution limit is about 23 nm (Fig.2.15).

`Cluster 292` (Fig.2.14)

In this case, the image of two separate clusters were reconstructed. Since the objects have only a few pixels, it is hard to apply ring supports. The big cluster has image size of about 70 nm, while the small cluster has image size of about 30 nm. The phase shift for the big one is above 10°, and for the other one much less than 10°. The PRTF function shows that the resolution limit is about 26 nm (Fig.2.15). The small cluster could be difficult to

observe at this resolution limit without the presence of the big cluster[12].

2.4 Discussions

2.4.1 Defocus in `cluster 292`

Coherent diffraction imaging is lensless. The focus problem is directly related to the phase retrieval in reciprocal space. An object out of focus has loose support rather than its focus (tight) support. In reverse, the constraint of such loose support during phasing process leads to a defocus problem. This problem can be avoid by using tight support achieved through "Shinkwrap" algorithm. The defocus problem also occurs in case of two or more objects, which are in different object planes with distances much larger than the focus length. It is impossible to focus all objects at one time. This situation had been verified by both simulations and experiments in [111, 75]. There are two separate objects in `cluster 292`. It is interesting to determine if both of them are in same object plane[13].

Looking back to Eq. (2.4), it may be rewritten as:

$$F(z)\cdot e^{iq_z z}U(q_x,q_y,z)=\int U(x',y',0)e^{-i(q_x x'+q_y y')}\,dx'dy'\,, \tag{2.24}$$

where factor $F(z)=e^{-ikz}/iz\lambda$ is a trivial constant in q_x-q_y or x'-y' plane, and can be neglected in this problem. The left-hand side of the equation is what is obtained in phasing process. The wave propagator $e^{iq_z z}$, which only contributes to retrieval phase, is responsible for the defocus problem. A small shift, $-\delta z$, of the object's focus plane along z axis is equal to a δz shift in the propagator on detector plane. The depth of focus can be defined at maximum phase shift of $\pi/2$ in the propagator:

$$z_f=\frac{\pi/2}{|q_z|_{max}}=\frac{\lambda}{4(1-\cos\theta_m)}\,, \tag{2.25}$$

with θ_m the maximum scattering angle detected. In this work, this value is estimated to be around 10 nm, much smaller than the cluster sizes.

There is a practical way to find the focus plane: propagate the exit surface wave of an object and the position of its tightest shape is the focus plane. The propagation of the reconstructed exit surface wave from z_0 to $z_0-\delta z$ follows a convolution with the propagator:

$$g(x)|_{z_0-\delta z}=\mathcal{F}^{-1}\left\{\mathcal{F}\left\{g_0(x)|_{z_0}\right\}\cdot e^{iq_z\delta z}\right\}\,, \tag{2.26}$$

where $\mathcal{F}$ is the Fourier transform operator. Note that the propagator works in reciprocal space. In case of many objects in a 2D reconstruction, the focus plane for each object can be figured out by this method. However, it does not mean that 3D information of each

[12] A similar situation on biomolecule imaging has been discussed by T. Shintake [110].

[13] The cases of `cluster 571/940` have no defocus problem due to the tight supports used. Therefore, the calculated propagation of the exit surface waves in the two cases is not presented.

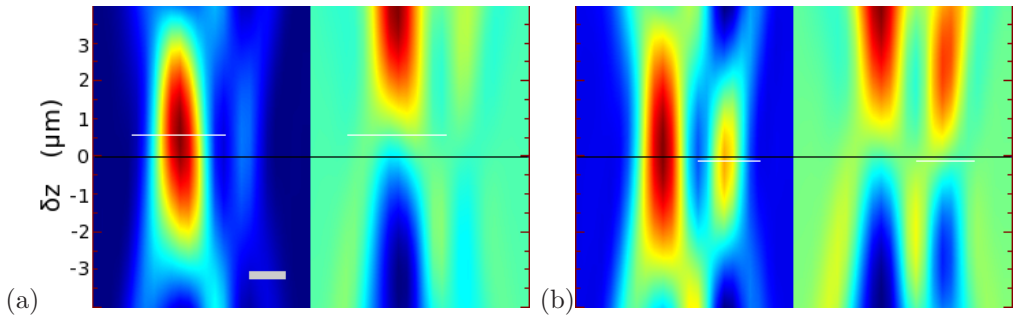

Figure 2.16: Estimation of defocus length in `cluster 292`. Two horizontal profile lines, with length 25 pixels cross center positions: (a) of the big cluster and (b) the small one, are chosen to reveal propagations. The results for both real part (Left) and imaginary (Right) in each case are showed with interpolation of the 25 pixels. The color mapping is linear and similar to Fig.2.14a. The white lines indicate the focus planes. Distance between two focus planes is about 700 nm. The scale bar is 100 nm.

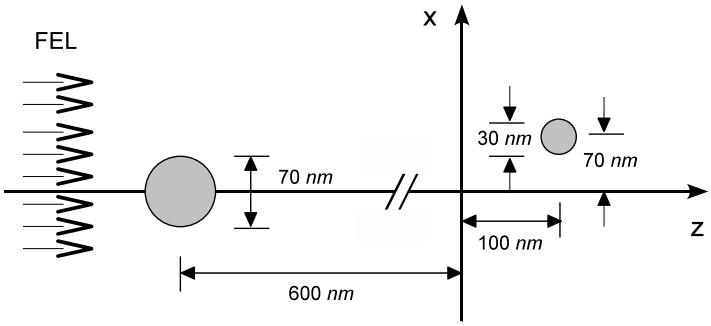

Figure 2.17: Estimated geometry of objects in `cluster 292`. The distance between two objects in y direction is estimated to be 20 nm, not presented here. Note that the clusters are assumed to be spherical in z direction. The position geometry of objects may have a uncertainty of 3D point reflection (see text).

single object can be recovered, because each tightest object is still a 2D "projection" on the respective object plane.

To show the propagations, two short horizontal lines with length of 25 pixels are chosen cross center of each cluster in `cluster 292`. Both real and imaginary parts of the objects are showed in Fig.2.16. Due to small phase shift in each object, the real part roughly represents the amplitude, while the imaginary part the phase. From the real parts, we can estimate the δz positions of the most compact objects.

It is found that the two clusters are not in the same object plane. The focus plane for the big cluster is at $-\delta z \simeq -600$ nm, and for the small one $-\delta z \simeq 100$ nm. There is no obvious change for object amplitudes (i.e. object size). This definitely limits accuracy of the estimated positions of the focus planes[14]. The phase shift of the big one in focus plane becomes about 8° , and that of the small one less than 5° . The distance, of around 700 nm, between two object planes is then much larger than the size of the objects. Fig.2.17 presents an estimated geometry of the two-cluster system.

Finally, recalling Eq. (2.20), the uncertainty of conjugation state in the reconstructed objects manifests itself as the possibility of an alternative geometry of the cluster positions. A 3D point reflection of the position geometry shown in Fig. 2.17 is also a possible solution. The Eq. (2.20) explains the point reflection in x-y plane due to the 2D diffraction pattern. Since the z positions of the clusters are estimated from real part of the exit wave after the propagation, the δz values will also change signs (i.e. 1D point reflection) after conjugation of the objects, indicated by Eq. (2.26).

2.4.2 Ring structures in `cluster 571/940`

As mentioned in § 2.2.1, a plane wave changes its form when transmits a bulk of uniform media

$$e^{i(kz-\omega t)} \rightarrow e^{i(nkz-\omega t)} = e^{i(n-1)k\Delta z}\, e^{i(kz-\omega t)}\,,$$

with refractive index of the media $n = 1 - \delta + i\beta$ and penetration depth Δz. The media-related transmission factor

$$e^{i(n-1)k\Delta z} = e^{-k\beta\Delta z}\, e^{-ik\delta\Delta z}\,, \tag{2.27}$$

contributes to the attenuation and phase shift of the plane wave in the media. The amplitude of the plane wave follows a decay over penetration depth. If a penetration depth z_p is defined at a threshold ratio $r_{th} = e^{-k\beta z_p}$, the phase shift within the defined depth can be written as:

$$\phi_p = -k\delta\, z_p = \frac{\delta}{\beta} \ln r_{th}\,, \tag{2.28}$$

[14] In Fig. 2.16, the obvious size changes of the big cluster exists in a propagation scale of 1∼2 μm.

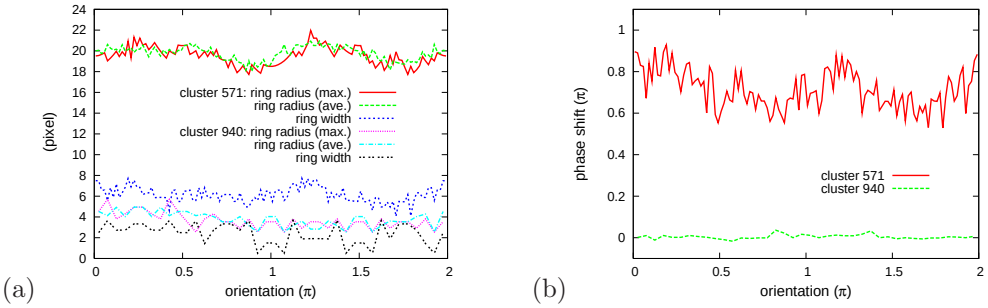

Figure 2.18: Ring structure in reconstructed cluster objects: (a) ring radii and widths estimated above threshold values of half maximum amplitude; (b) phase shifts in the ring structures. The value fluctuations indicate imperfect sphere structure of the clusters.

which depends only on the refractive index n. The following discussions on ring structures in reconstructions are based on this picture.

The refractive index for an atomic cluster can be estimated from its density by theoretical calculation [112]: $n = (1.0066, 0.046)$ for xenon cluster at density[15] $(4.33\,\text{Å})^{-3}$. At $r_{th} = \text{Exp}(-1) \simeq 0.37$, the penetration length is 48 nm, which is much less than diameter of the `cluster 571/940` object. This leads to ring structure in images of the clusters due to spherical geometry. The ring structures, as object supports, were used in the phasing process to remove unconstrained modes (see § 2.3.2). According to Eq. (2.28), the corresponding phase shift could be positive and very small, around $0.046\,\pi$. It could be independent of object sizes.

In the reconstructed objects, ring structures are not perfect with radii and widths fluctuated on azimuthal orientations (Fig. 2.18a). The `cluster 571` has ring radius ∼20 pixels (170 nm) and width ∼7 pixels (60 nm). The `cluster 940` has ring radius ∼4 pixels (40 nm) and width ∼3 pixels (30 nm). In the plots, two ways are used to estimate the ring radii: radii average over inner and outer ring border; radial maximum amplitude on the ring. The overlap between two radii estimations indicates that the expected feature of radial decay distribution on ring structure is not observed at such low resolution. If use $z_p = 48$ nm, an ideal sphere with radius larger than 40 nm has ring width of less than 8 nm. A decay of object amplitude within this width is definitely not resolvable within current resolution limit of 25 nm, even within the perfect resolution (17 nm). This increases the difficulty to extract further quantitive information from the ring structures.

The absolute phase shifts on the ring structures are plotted in Fig. 2.18b. The signs of the phase shifts are unknown, because the conjugate states of the objects are undetermined by diffraction intensity (refer to Eq. 2.20). The absolute phase shift in `cluster 571` is around $0.7\,\pi$, while that in `cluster 940` is below $0.03\,\pi$. According to Eq. (2.28), the large discrepancy between the phase shifts in the two clusters indicates that the n values or cluster densities of the two clusters could be much different.

[15] The same density for xenon clusters was used by the dynamics simulations in the preceding chapter.

However, this transmission picture does not take diffraction effect into account. The irregular shape of ring structures in reconstructions mainly results from diffraction of imperfect surfaces of the objects. The diffraction effect is described by Eq. (2.9) with constant $\varphi(\mathbf{r}')$ inside object. Unfortunately, the diffraction formula, which works only in regime of weak phase shift or absorption, can not explain the ring structures here.

The multislice method which considers both transmission and diffraction effects is introduced in § 2.4.4 to understand the ring structures, as an extension of discussions in this section. The real sizes of the objects, as input parameters in the multislice simulations, can be obtained from the diffraction patterns via simulations with Mie theory.

2.4.3 Mie theory simulation

Mie theory, basically, is an analytical solution to the problem of electromagnetic plane wave scattered by an uniform spherical particle, described by Maxwell's equations. The solution uses spherical vector wave functions as expansion bases for both scattering and internal field. The related coefficients can be determined by boundary conditions on surface of the spherical particle. In principle, Mie theory works for all possible ratios of object diameter to wavelength. The numerical accuracy of solution depends on the limited number of expansion bases used in simulations.

Mie theory is widely used for estimation of particle size by matching the measured diffraction patterns in the far field. For a spherical object, the scattering of polarized light field is described by following formulas [113]:

$$E_r = S_1(\theta)\frac{e^{-ikr}}{ikr}E_{r0}\,, \quad E_l = S_2(\theta)\frac{e^{-ikr}}{ikr}E_{l0}\,; \tag{2.29}$$

$$I(\theta) \propto \frac{|S_1(\theta)|^2 + |S_2(\theta)|^2}{r^2}\,, \tag{2.30}$$

where $S(\theta)$ are scattering-angle dependent amplitude elements, and r , l refer to electric fields perpendicular to and parallel with the scattering plane, respectively. The single dependence of the diffraction on the scattering angle (or q) results from spherical symmetry in the object.

The information on real size of clusters is crucial to understand possible changes due to radiation damage in the experiments. The Mie theory is used to obtain such information directly from the diffraction patterns. As a first step, the irradiated clusters are assumed to be spherical and density-uniform in Mie calculations.

In Mie theory, there are three input parameters: ratio between sphere size and wavelength, refractive index and scattering angle. The previously calculated refractive index $n = (1.0066, 0.046)$ is used here. Other parameters are the same as the imaging experiments. According to Eq. (2.30), the simulated Mie patterns can be reduce to 1D, as a function of spatial frequency $q(\theta)$. The simulated and experimental patterns are q-averaged for comparison due to imperfect shapes of the clusters. There are many popular Mie calculation programs for single spheres [114], such as BHMie [115] and Miev0 [116]. The "Miev0" code which includes self-tests is chosen in this work.

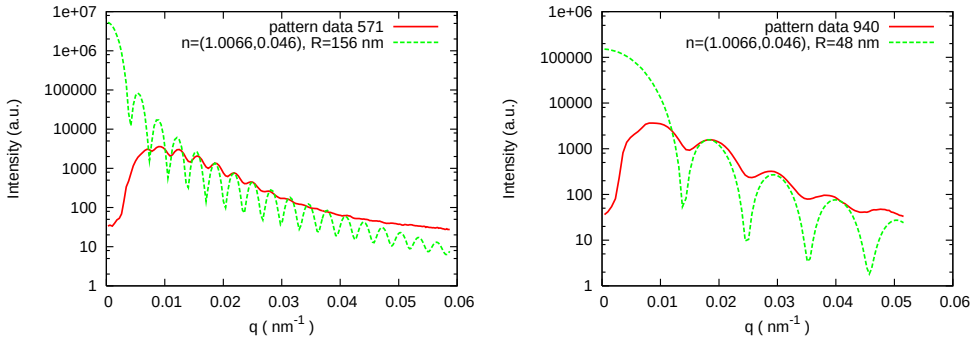

Figure 2.19: Mie fitting for the patterns of `cluster 571/940`. The q-averaged $I(q)$ of the pattern data were used. The respective fitting radii are: 156 nm and 48 nm. (The q has same convention as in Fig. 2.15.)

The matching results of Mie pattern intensity (Fig.2.19) show that the estimated real radius of the cluster in `cluster 571` is 156 nm, and that for `cluster 940` is 48 nm. The fitting sizes are quite close to that of the reconstructed objects (170/40 nm respectively) within the achieved resolution limit (25 nm). The fitting results do not change much when slightly different values of refractive index are used in Mie calculations. Both peaks (maximums and positions) and local depths (or minimums) are not perfectly reproduced in the Mie fitting. There are two reasons at least: (i) irregular fringe shapes in the diffraction patterns (i.e. the cluster objects are not fully spherical) lead to deviation of peak positions and depths after q-average; (ii) large signal background in the imaging experiments (Fig. 2.5b) comes from the imaging environment (such as dark signals, incoherent scattering of photons) and the detection system (such as point spread function, noise from the MCP and the Phosphor screen).

A Mie object can be obtained from a complex Mie pattern calculated with Eq.(2.29) by direct inverse Fourier transform. The Mie objects is calculated using the size values fitted in `cluster 571/940` and with same resolutions. Fig.2.20 shows center-cross profiles of the Mie objects. The Mie objects have sharp borders. The radii of the Mie objects are almost the same as input sizes. Both of the objects have flat phases with value $-0.18\,\pi$, which have no obvious phase shift and are different from the estimations in the last section ($+0.046\,\pi$). Note that the irrelevant phases outside the Mie objects have been set to zero.

However, no ring structure is repeated in the Mie objects, while the calculated absorption efficiency factor $Q_{abs} > 0.90$ clearly shows the strong absorption of light in Mie calculations. The spatial details of light absorption are missing probably due to the limit number of expansion bases used in numerical calculations, which is possibly set only for acceptable accuracy of simulated diffraction intensity, not of simulated phase. This problem is probably neglected when only size information is sought. The absence of this absorption information reduces the reliability of the nearly zero phase shifts in Mie objects.

In short, the Mie theory can allow the sizes of the clusters to be determined directly from

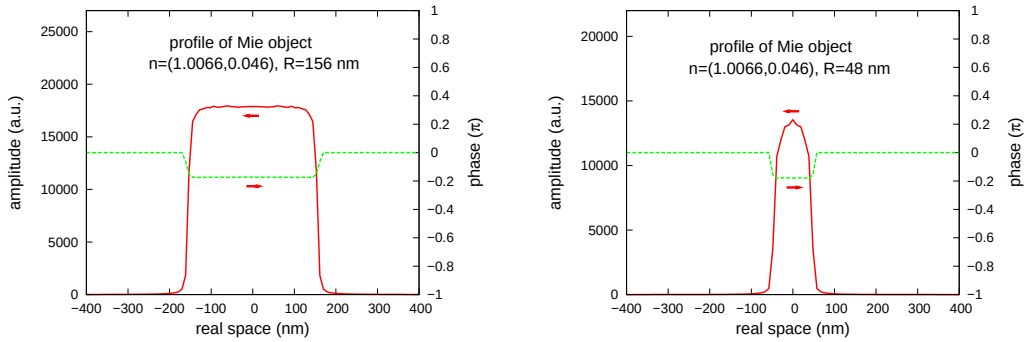

Figure 2.20: Mie object calculated from complex Mie patterns. Both profiles of amplitude and phase are presented. The Mie image sizes of the objects well match the input size parameters. The phases of both objects are almost uniform, around $-0.18\,\pi$. There is no obvious phase shift inside the Mie objects. The strong absorption effect (i.e. ring structure of amplitude), indicated by the absorption coefficient in Mie calculations, does not appear in the complex Mie objects.

the measured diffraction patterns, but the ring structures of absorption are not reproduced in current numerical Mie simulations. The above discussions are based on assumption of homogenous clusters. A more realistic cluster may have dilute density on its surface. It could be modeled as a coated sphere of two-layer structure, which had been solved in Mie theory [115]. The cases of inhomogeneous clusters will be studied in future.

In the next section, the multislice method is applied to describe both effects of diffraction and strong absorption in the irradiated clusters.

2.4.4 Multislice propagation simulation

The *Multislice method* is an accurate simulation tool for exit surface wave (see § 2.2.1) of a thick three-dimension object in CDI. It was firstly invented for transmission electron microscopy (TEM) on crystals of limited thickness [117]. The method is based on the finite difference form of Schrödinger's equation with backscattering being neglected [118, 119]. It had been generalized to soft X-ray sources in a similar formulation [120, 77].

Inside thick objects, light is always scattered many times by atoms. This effect of multiple scattering is described by the Born series in scattering theory (see Eq. 2.7). The first Born term (approximation) is applied in optically thin object where only single scattering is considered. The multislice method regards a thick and inhomogeneous object as a set of many slices with finite thickness δz. Each slice is thin enough ($\delta z < a_0$, see Eq. 2.14) that single scattering dominates and the first Born approximation is valid. Hence, the effects of transmission (single scattering) and diffraction (light propagation) can be separated for each slice based on the far field diffraction (relation of Fourier transform). Then, the multiple scattering can be reproduced by accumulation of the single scattering effects over all slices.

In each slice, the transmission of the wavefield $\psi(x, y)$ in the object is projected on

corresponding scattering plane z, and then propagates freely to the next scattering plane $z+\delta z$:

$$\psi'(x,y)|_z = \psi(x,y)|_z \cdot e^{ik\delta z \cdot n(x,y)|_z} \tag{2.31}$$

$$\psi(x,y)|_{z+\delta z} = \mathcal{F}^{-1}\left\{\mathcal{F}\left\{\psi'(x,y)|_z\right\} \cdot e^{-i\frac{q_x^2+q_y^2}{2k}\delta z}\right\}, \tag{2.32}$$

where $n(x,y)|_z$ is refractive index of the object at z plane and $e^{-i(q_x^2+q_y^2)/2k\cdot\delta z}$ is kernel of the Fresnel propagator[16]. The exit surface wave is obtained at end of the thick object immediately after iterations of all slices. The free-space propagation in Eq. (2.32) takes the small angle scattering (i.e. Fresnel approximation) into account. It had been extended to the cases of large angle scattering by authors in [77]:

$$\psi(x,y)|_{z+\delta z} = \mathcal{F}^{-1}\left\{\left[\frac{q_z}{k+q_z}\mathcal{F}\left\{\psi(x,y)|_z\right\} + \frac{k}{k+q_z}\mathcal{F}\left\{\psi'(x,y)|_z\right\}\right] \cdot e^{iq_z\delta z}\right\}, \tag{2.33}$$

where q_z becomes close to zero and $e^{iq_z\delta z}$ approaches the Fresnel propagator in approximation of small angle scattering (see § 2.2.1).

In CDI multislice simulations, an object may be illuminated by plane wave e^{ikz} within its transverse section on x-y plane. The thickness of each slice should satisfies the condition in Eq. (2.14), and the thinner the slice, the better the accuracy in the simulations. The pixel size d_p in slices of the object should obey Bragg's law required by the far field diffraction:

$$d_p = \frac{1}{2}d_m = \frac{1}{2}\frac{\lambda}{2\sin(\theta_m/2)} > \frac{\lambda}{2\sqrt{2}}, \tag{2.34}$$

where the maximum angle θ_m in forward scattering should be less than $90°$. Otherwise, the propagation direction is changed due to back scattering, and therefore, the relevant propagators are ill defined. The exit surface wave obtained at the end of the object may be out of focus. The focus plane is usually at center of the object along illumination direction where the wavefield has smallest object support. The exit surface wave should propagate freely back to the focus plane using Eq. (2.26) with the corresponding propagator to obtain so-called "object" image in focus.

In this work, the cluster objects are assumed to be homogenous with same refractive index used in the previous sections. The objects of `cluster 571/940` are optically thick with thickness larger than $a_0 \simeq$30 nm. The pixel sizes and resolution sizes used here are same as in the phasing processes. The simulated exit surface waves in focus planes are shown in Fig 2.21. The peak positions of amplitude and phase shifts in profiles of the reconstructed objects are almost perfectly reproduced. The slight differences result from both irregular shape of the objects and their low resolutions in the reconstructions. According to the simulations, the signs of the phase shifts inside objects are negative, while these are unknown in the reconstructions.

[16] It is the form in reciprocal space. The convolution operation in Eq. (2.32) applies the propagation to each point in real space.

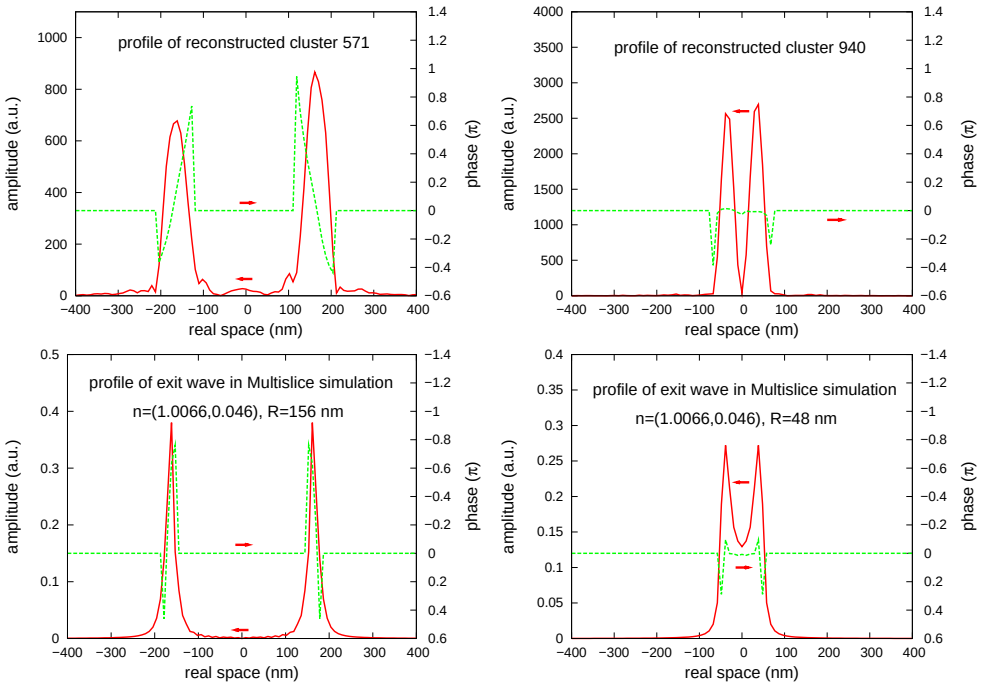

Figure 2.21: Simulations of exit surface wave with multislice method (Second Row) in comparison with the reconstructed objects (First Row) at 13.8 nm wavelength. The exit surface waves propagated back to focus planes reproduce the ring structures in the reconstructed objects. Note that input real sizes of objects in simulations are obtained from the Mie theory fitting.

The multislice method is not suitable for the case of `cluster 292`, which has an interesting phenomenon of defocus. Sizes of the cluster objects (with radius of around 35/15 nm) in this case are comparable to the wavelength (13.8 nm). According to Eq. (2.34), the objects can have only several pixels in a multislice simulation, similar as the corresponding reconstruction. This may lead to large errors in such simulations. However, a critical reason behind is: the multislice formulation used here is based on the scalar assumption of light wave, which could be invalid in such case of object size comparable to wavelength.

2.4.5 Radiation damage in the irradiated clusters

So far, the experimental pattern data and corresponding reconstructions results seem understood assuming that the irradiated clusters are homogenous. Radiation damage has not been considered. The sizes of objects and details in reconstructed images are consistent and not sensitive to the refractive index within the achieved resolutions. However, single FEL pulses are very intense and melt almost everything on their path, including the clusters investigated above. It is a fundamental interest to see and understand details about the interaction processes. In this part, the possible processes of radiation damage and measurements of relevant phenomena occurring in the irradiated clusters are briefly discussed.

The photon energy at 13.8 nm wavelength is 90.0 eV, which is above the sixth ionization threshold of xenon atom (71.8 eV) and below the seventh (92.1 eV). Electrons on outer-shell of xenon atoms can be directly ionized by the FEL photons. The dynamic simulations in the previous chapter conclude that the enhanced inverse bremsstrahlung absorption does not play a significant role at such short wavelength. Both photoionization and collisional ionization can be dominant processes in the irradiated clusters. Photoelectrons may deliver residual photon energies to ions through electron-impact ionization. The photon energies may be deposited in ions by a chain of ionization processes. If no significant mechanism but photoionization contributes to photon absorption, ions with charge higher than six are expected to be rare in the clusters. Energetic electrons may escape and leave the clusters charged.

During the irradiation there may be two typical spatial distributions of ions depending on the size of the clusters, as illustrated in Fig 2.22. (i) is for optically thick clusters which the FELs can hardly penetrate. The illumination fades out in the clusters and triggers ionization processes, which create high ion charges on their irradiated surface and lower charges as photons or electrons penetrate deeper. This leads to a cascade of ions with different charges on beam direction inside the clusters. (ii) is for much smaller clusters where illumination of the FELs can be assumed uniform. The generating ions in such clusters may spread almost uniformly if photoelectrons or secondary electrons in ionization processes have no preference on outgoing directions. The time-dependent details about charge population and spatial distribution of ions in the above two cases could be obtained through simulations with dynamic models[17], which are planed for the near future.

[17]The xenon clusters in the imaging experiments have a huge number of atoms. For instance, a xenon

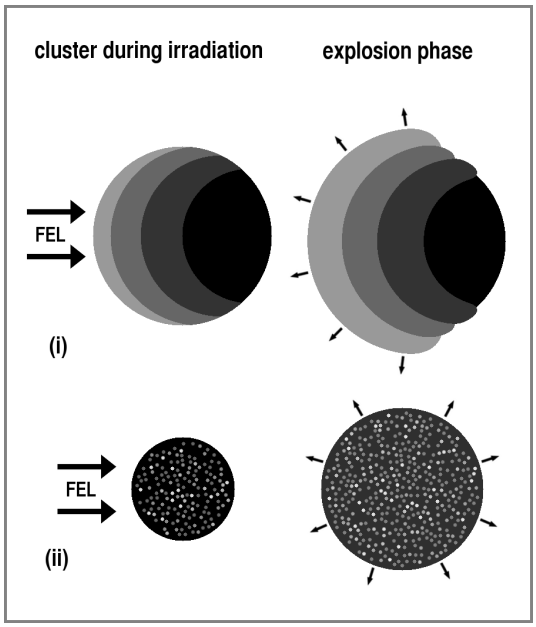

Figure 2.22: Hypothetical geometries of clusters during irradiation and explosion phase: (i) thick cluster which a single FEL pulse can not fully penetrate; (ii) small cluster which the pulse can illuminate fully and uniformly. Black color denotes neutral atoms, gray color ions (the lighter the color, the higher the charges, and electrons are not shown).

In the single-shot imaging experiments, the measured diffraction patterns are accumulations of scattering signals varied during single pulses, which are around ten femtoseconds. According to the discussions in the previous chapter, atoms and ions in the irradiated clusters are almost stationary over such a short timescale. A significant contribution to the varied signals comes from ions with varied charge states, which have low photon-scattering ability due to the missing of outer-shell electrons. The electron structure of the clusters which determines their optical properties may be significantly changed due to the intense pulses. In addition, the Thomson scattering from electron gas inside the clusters may contribute to the background of the signals.

Little detail can be obtained about the radiation damage from the analysis of the experimental data in the previous sections. There are two possible reasons: the FEL pulses are so short that the damage is less visible; or the spatial resolutions achieved (above 25 nm) is too low to resolve the damage details. The achieved resolution in the reconstructions is mainly limited by the FEL wavelength (13.8 nm). An irradiated cluster with size between that of type (i) and (ii) in Fig 2.22 may be very sensitive to its optical properties due to possible transition between the two types. Unfortunately, the typical radius of such cluster, estimated to be around 50 nm or smaller, can be resolved only by several pixels as indicated by the multislice simulations in Fig 2.21.

The single-shot imaging experiments can change electron configurations in the irradiated clusters through varying experimental parameters, for instance, the FEL source parameters:

cluster with radius of 50 nm has around five million atoms. The number is far beyond computation capability of the unoptimized MD model in the previous chapter. The Boltzmann model may simulate such clusters due to its sufficient reduction of degrees of freedom.

pulse length, laser intensity and wavelength. Contrast of the variable parameters may reveal more information about the radiation damage. However, such single-shot experiments cannot measure what occurs in the irradiated clusters after the FEL single shots.

A non-neutral cluster after the irradiation may enter into a expansion phase due to Coulomb interactions between ions. The expanding motions of ions occur at time scale of picoseconds, much longer than the single FEL pulse. As shown in Fig 2.22, the expansion geometry strongly depends on spatial configuration of ions (and electron gas inside as well) during the FEL irradiation. Time, as a new dimension, should be added into the imaging experiments to resolve the expansion phase.

There is a general method called *pump and probe* (P&P), using two laser pulses with time delay variable. The first pulse pumps the investigated system and the second pulse probes the system after the excitation. This method can resolve the whole time evolution of the excited system if the system is reproducible and time resolution is sufficient. In the field of CDI with FELs, it has been demonstrated by the picosecond-delay imaging experiment with optical laser pumping and FEL imaging [121]. The FEL probing was applied to image structure change at nanometer scale due to its high intensity and short wavelength. The P&P imaging experiment with two FEL pulses is not demonstrated until now. It is practically difficult to synchronize two separated FEL pulses with a particle beam meeting at a focus spot of micrometer size[18].

The complicated dynamics within the clusters after irradiation with FELs will be much more deeply understood once the P&P technique is ready. Such developments will help to figure out the limit of imaging using FEL pulses.

2.5 Summary and outlook

In summary, the objects of xenon clusters have been successfully reconstructed from the pattern data in the single-shot imaging experiments performed at FLASH at wavelength 13.8 nm. The cluster objects have clear single ring structures which indicate strong photon absorption during the exposure to the FEL irradiation. The smallest size of cluster objects is about 30 nm in diameter. The resolution limit achieved in the reconstructions is 25 nm. In `cluster 292`, the two clusters are found to stay in different focus planes, with distance 700 nm much larger than sizes of the clusters.

The Mie theory simulations show that the real size of `cluster 571/940` is very close to the reconstructed size within achieved resolution. The calculations of multislice propagation consistently reproduce their ring structures. These simulations assume that the irradiated clusters are density-uniform and not damaged by the FELs. The information about radiation

[18] A dedicate machine at FLASH, called the *Autocorrelator* [81], has been built to separate single FEL pulse into two children pulses: intensity of one fourth each, range of time delay from -3 ps to 20 ps, and maximum splitting angle 2° . It is potentially useful for this new type of experiments.

damage seems hard to extract from the current experimental patterns due to their limited spatial resolution.

There are a great many interesting questions related to imaging of atomic clusters. For example, the idea of sacrificial tamper coating a measured object (such as macromolecule) was proposed to protect the object exposed to intense FEL radiation [53]. Its effect was witnessed by the spectra measurements of xenon clusters coated by argon atoms [56]. It will be very interesting to see this effect in imaging experiments. Both dynamics simulations and imaging experiments can be extended further, to investigate such questions in parallel. It will be very exciting to see interactive progress made in future between dynamic (and diffraction) simulations and cluster imaging experiments (and spectra measurements as well).

A new FEL facility in the world, LCLS [83], is on operation now. Its FEL radiation wavelength can potentially reach the hard X-ray regime (1.5 Å), which is much smaller than the size of the atomic clusters. Its advantages of shorter wavelength and less attenuation enable discovery of more structural details at atomic scales. The studies of the atomic clusters will provide meaningful indications for single particle imaging experiments of biological samples with X-ray FELs.

Chapter 3

Imaging of biological samples

3.1 3D coherent diffraction imaging (CDI) of single bio-particles with XFELs

This section presents the scheme of 3D CDI technique with X-ray FELs, and the potential challenges for imaging biological particles, such as proteins, macromolecules and virus particles, at high resolution. These challenges require advanced experimental techniques and data analysis. However, one of the challenges, radiation damage within imaged samples, seems difficult to be fully taken into account in a data model. The damage effect should be minimized as much as possible by a careful choice of experimental parameters. One idea to reduce sample damage is to coat a sample with a sacrificial tamper [53]. It will be briefly discussed at the end of this part, and the corresponding diffraction effect will be investigated in the next section.

Imaging with FELs is quite different from that with synchrotron radiation. FEL radiation is so intense that most samples will be destroyed. On the other hand, FEL pulses are very short (with pulse lengths of tens of femtoseconds), and the structure of an object can be probed before its destruction [54]. It is impossible to image the same object for a second time. Synchrotron radiation is much less intense, and sample damage caused is much less. This allows diffraction measurements of the same object on different (known) orientations by rotating the sample holder [75]. In 3D CDI with FELs, identical objects are necessary for the collection of many 2D diffraction patterns from different views. Spraying techniques, such as aerojet [122] and electrospray [123], have been developed for efficient delivery of such identical objects (in droplets of solution or in gas phase) in vacuo to FELs beams. As shown in Fig. 3.1, the aim is that single objects in particle stream are shot in series by single pulses, with diffraction signals recorded on a CCD detector. Those objects that are hit dissociate quickly after single pulse radiation.

The first challenge in 3D CDI with FELs is the missing information of object orienta-

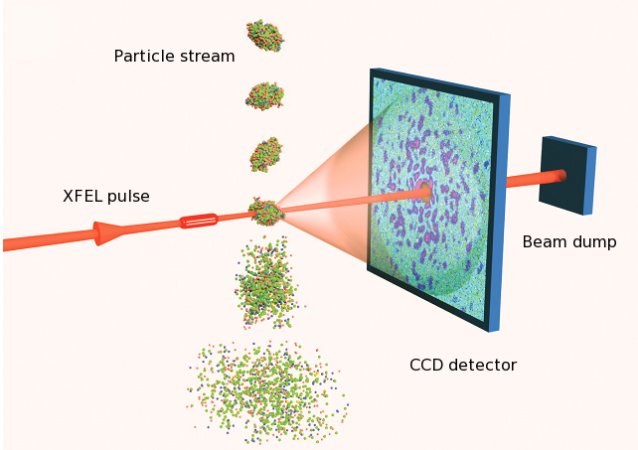

Figure 3.1: Schematic view of 3D single particle CDI with XFEL pulses (figure from [124]). Identical particles with random orientations are injected sequentially into the XFEL beam area. Diffraction patterns are recorded by a CCD detector after single pulses.

tions. 3D CDI needs a sufficient number of 2D diffraction patterns at different orientations to construct a 3D diffraction pattern, which is used to solve the 3D structure by the phasing process in CDI (see preceding chapter). Due to the delivery techniques, object orientations are unknown in the CDI with FELs. The assembling of a 3D pattern from measured 2D patterns is no longer straightforward. A solution, called *common line* method, has been applied in cryo-electron microscopy (cryo-EM) [125]. Here, it compares a pair of 2D diffraction patterns in reciprocal space from same object in different views, and there should exist a common line crossing the origin. Positions of the line in each pattern may uniquely identify the relative orientations between the two views. This method has been used in CDI simulations by authors in [126].

Another challenge is the low signal-to-noise ratio (SNR) in the measured diffraction patterns, which is specific to biological samples in the hard X-ray regime. The elastic scattering is very weak for light atoms such as carbon, which constitute the backbone of biological particles. An idea of *classification* from Cryo-EM [125] is applied to improve SNR in 2D diffraction patterns [127, 128, 129]. The measured 2D patterns are classified into groups through identifying highly correlated pattern pairs. Those patterns in same groups have very similar views, and their average will improve the SNR if they are properly classified. However, when particle size becomes smaller and smaller (for example, for single proteins or macromolecules, 10 nm or less), single pixels on the detector record photons with maximum of 2 or 3 counts (see § 3.2). The classification method based on the analysis of pair correlation is seriously limited by very low SNR [130], and will fail to recognize close views from noisy patterns. Without the improved SNR to find the lines, the common line approach becomes extremely difficult to determine relative orientations of 2D patterns. In contrast, X-ray crystallography has a large number of identical unit cells in the crystal, which scatter much more photons and concentrate them on Bragg peaks. It is a big challenge for CDI (single particle imaging) to reach the resolutions that X-ray crystallography achieves.

Assuming the noise follows Poisson distribution in a simple case, the above two challenges together constitute a problem to determine orientations of randomly orientated 2D

diffraction patterns with presence of significant Poisson noise. This problem has been studied separately by two groups with respective algorithms: *Generative Topographic Mapping* (GTM) [131] and *Expansion-Maximization-Compression* (EMC) [130]. Their algorithms are based on the same technique, called *expectation maximization* (EM), which uses an iterative method to find a maximum of defined likelihood of parameters in a data model that connects input diffraction data and latent variables (orientations). One of the slight differences between them is [132]: GTM uses a zero-centered Gaussian distribution for error tolerance of latent variables, which can be extended to other types of possible noise beyond Poisson noise; while EMC in the form given by the literature handles only the Poisson noise. The advantage of these methods is that they can surprisingly extract orientation information from high levels of *known* noise. For example, the Poisson noise can be down to average photon counts of 0.01 over whole single patterns. However, the weakness at present is that both methods are extremely computationally time consuming and scale as the sixth to ninth power of the number of pixels of object size. It is plausible to speed up iterative convergence to a solution (i.e. computation performance) by adding more physical constraints to these general methods. So far, EMC has been applied for 3D assembling of experimental 2D patterns at low resolution [133].

The third challenge is radiation damage during single FEL pulses. For X-rays with energy 12 keV, a conventional damage barrier is about 200 photons/Å^2. It can be extended to very high dose[1] [44] so long as FEL pulse is short enough [134, 135]. At present, pulse lengths of FELs, which can reach around three femtoseconds at LCLS, are promising to minimize radiation damage during single pulses. Several dynamic simulations [44, 58, 57, 70] related to CDI of biological particles with XFELs at 12 keV have revealed possible damage processes: (i) K-shell electrons in atoms (carbon, oxygen,nitrogen and sulphur) are ionized and escape, and then Auger decay follows of about 1-10 fs lifetimes; (ii) Auger electrons may cause impact ionizations and produce secondary electrons of low energies; (iii) electrons trapped in bioparticles may slow down their Coulomb explosion. (iv) quickly escaping ions may be protons, the lightest ions, and highly-charged sulphur ions (due to large photoionization cross sections). (v) heavy atoms or inhomogeneous density in bioparticle may lead to large local distortions or atom displacements.

It is important to include above possible damages into a complete data model for 3D CDI analysis at high resolution. However, the diffraction effects from radiation damage are difficult to quantify. For example, the electron gas contributes to background signal which depends on electron density and is a cumulative effect during a single pulse; motions of particles could be modeled as certain noise in real space when density of an object is uniform, but it becomes difficult when the density is inhomogeneous. The experimental study of those damage processes [85] is critical to those simulation models, but unfortunately, such experiments are limited by low SNR in CDI of single bioparticles. As mentioned in the preceding chapter, atomic clusters (or other good model objects for bioparticles) can be chosen in such experiments and may help to understand possible damages. Since modeling

[1]The dose will be about 10^6 photons/Å^2 for the ideal parameters of the LCLS [83].

the damage effects for data analysis is difficult, minimization of radiation damage in CDI experiments is preferred.

There is an interesting idea to reduce radiation damage, introduced by authors in [53]: an object is coated by a sacrificial tamper, such as liquid water or other liquids. This is natural in the spraying techniques: single bioparticles may be injected into vacuum within droplets of water. They simulated such a system using a 1D hydrodynamics model, and concluded that a sacrificial layer of water with thickness above a certain value significantly reduces atomic motions in the object. The argument is supported by independent simulations of a MD model [69]. The two groups investigated the diffraction signals contributed by the simulated radiation damages and the tampers. The diffraction signals from the former are reduced, while those from the latter increase.

However, the two groups did not answer the important question in the context of 3D CDI with FELs: how much does an effective tamper (with certain thickness) affect orientation information of imaged object in diffraction patterns? Atomic positions of the tampers for each identical object, such as two drops of liquid water, vary significantly. Hence, the identical objects with water layers become not fully identical. This variation must induce a negative effect in 3D data assembling to some extent, which could be critical for application of the interesting idea. Note that this variation effect behaves like some kind of random noise in real space. The question will be addressed in the next section.

3.2 Coherent diffraction of a single virus particle: the impact of a water layer on the available orientational information[2]

Abstract

Coherent diffractive imaging using X-ray free electron lasers (XFELs) may provide a unique opportunity for high resolution structural analysis of single particles sprayed from an aqueous solution into the laser beam. As a result, diffraction images are measured from randomly orientated objects covered by a water layer. We analyse theoretically how the thickness of the covering water layer influences the structural and orientational information contained in the recorded diffraction images. This study has implications for planned experiments on single particle imaging with XFELs.

Introduction

X-ray FELs are expected to open new horizons for structural studies of biological systems, especially for studies of non-crystalline samples, such as viruses or living cells. In general, radiation damage limits the accuracy of the structure determination of biological particles in standard diffraction experiments. However, computer simulations of damage formation have strongly suggested [44, 57, 51, 58, 52] that radiation tolerance may be extended to very high doses with ultrafast exposures, as will be possible with the presently operating and developing X-ray FELs, such as LCLS, SCSS, and the European XFEL. This is due to their photon pulses being of a shorter duration than the time atoms require to move a distance comparable to the required resolution. This improved radiation tolerance indicates the possibility of recording images of single biological particles at high resolution without the need to concentrate scattered radiation into Bragg reflections. This application of FELs could have a tremendous impact on structural studies at both the molecular and cellular level, with profound implications for biology and medicine. Recent experiments performed at FLASH [54, 123] have demonstrated the proof of this imaging principle.

There are, however, still many technical and physical issues that need to be resolved in a more quantitative manner, especially if one aims for structural information at high resolution. Here we address the important question of how a specific method of object preparation may affect the structural information that can be extracted by diffraction imaging methods. In particular, we investigate the possible loss of structural information due to the presence of a water layer surrounding the imaged object. Particles injected into an FEL beam by spraying techniques will be covered by an evaporating water layer [136, 137]. A thick layer of water around the imaged object is considered to be a method of slowing down the radiation damage. i.e. slowing the movement of ions due to repulsive Coulomb forces within

[2]This section has been submitted as *Paper V*: F. Wang, E. Weckert, B. Ziaja, D.S.D. Larsson and D. van der Spoel.

the irradiated sample [53]. Here we investigate in detail how the thickness and structure of the surrounding water layer (WL) influences the diffraction images of virus particles. We consider surrounding water layers of $0.5-2.5$ nm average thickness. The loss of orientational and structural information due to the presence of a water layer and its varying molecular structure is quantified theoretically, using molecular dynamics (MD) and coherent diffraction imaging simulations. The effect of Poissonian noise (PN) for scattered photons is also taken into account.

Pattern Generation

We consider here a small bioparticle to reduce the computational effort, but the results obtained can be generalized for larger objects as the mean photon count per pixel approximately scales with the object radius. The test object for the simulations is the Satellite Tobacco Necrosis virus (STNV), whose capsid structure has been solved by X-ray crystallography [138] (Protein Data Bank ID: 2BUK): object size ∼17 nm, ∼0.18M atoms, icosahedral symmetry. We generate realistic water shells around the virus using the Tip3P model of liquid water [139] with average thicknesses of 0.5/1.5/2.5 nm, and use the molecular dynamics (MD) simulation package GROMACS [140, 141] to simulate these systems in vacuum. In this scheme we keep the positions of the equilibrated virus atoms fixed, and only allow the surrounding water molecules to move during the simulations, as we consider the effects of "random" water layers on diffraction images. The related effects of slightly different protein conformations within the virus shell [142] as well as effects due to the radiation damage processes are not considered in this work. The MD simulation of radiation damage within a homogeneous carbon cluster in [53, 69] suggested that a thick water layer coating, as a sacrificial tamper, can significantly reduce the damage inside the cluster. In the case of STNV, a water tamper with 2.5 nm thickness would be sufficient to achieve a comparable effect [53].

In order to generate diffraction patterns, we use the snapshot coordinates of atoms after simulating with physical time sufficiently long to randomize the water layer, and calculate the diffracted intensity with the following formula:

$$I(\mathbf{q}) = \left| \sum_i f_i(q)\, e^{2\pi i \mathbf{q}\cdot \mathrm{r}_i} \right|^2 \; r_e^2\, \Phi_{in}\, \Omega_{pix}\,, \tag{3.1}$$

where $\mathbf{q}$ is the wavevector transfer (same convention as Fig. 2.15); f_i are the atomic form factors for each element species; r_e is the classical radius of the electron; Φ_{in} is the photon fluence, and Ω_{pix} is the solid angle for one pixel. Fig. 3.2 shows the average diffracted intensity versus resolution calculated using the following parameters [83]: wavelength 1.5 Å , and $\Phi_{in} = 10^{14}\,\mathrm{ph}/\mu\mathrm{m}^2$ (i.e. 10^{12} photons per pulse within the spot size of 100×100 nm^2). The solid angle Ω_{pix} in the patterns is determined by the Nyquist sampling rate. The maximum q value corresponds to a perfect resolution of 1.8 Å in real space. The most

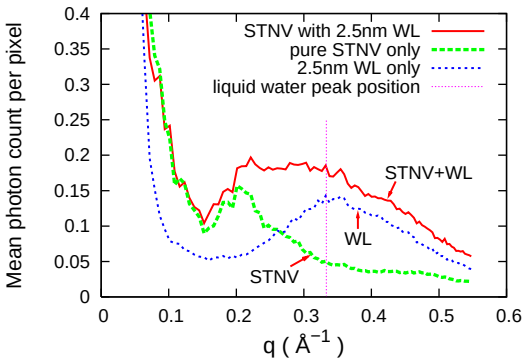

Figure 3.2: Average diffraction intensity $I(q)$ from the virus covered with a water layer of 2.5 nm thickness, calculated with parameters: 1.5 Å wavelength, 10^{12} photons per pulse, 100×100 nm^2 focus spot. The maximal photon count was $2-3$ counts in one pixel. The separate contributions from the pure virus and the water layer are shown as references. Significant contributions from water molecules lie within the liquid water peak range (~ 3 Å) indicated by the vertical line.

significant contribution from the water layers lies in the q-range of bulk water ($\sim (3\text{Å})^{-1}$). We note here that due to the coherent interference between contributions from water layer and the virus the curve STNV+WL is not a strict sum of virus (STNV) and water layer (WL) contributions.

The diffraction patterns obtained from such small single virus particles have too low photon statistics for a reasonable 2D reconstruction. Therefore, patterns of a large number of individual particles need to be averaged with the correct orientation to improve the signal-to-noise ratio (SNR). This procedure requires a classification of the diffraction patterns according to the different rotation angles of the object [127, 130, 131].

Analysis of Correlations between Diffraction Patterns

In order to quantify the possible loss of orientational and structural information, the q-dependence of the correlation of diffraction patterns for different relative particle orientations α is calculated in analogy to [129], as

$$G(\alpha,q) \equiv \frac{\tilde{I}(\alpha,q)\cdot\tilde{I}(0,q)}{\sqrt{\langle\tilde{I}(\alpha,q)^2\rangle_q}\cdot\sqrt{\langle\tilde{I}(0,q)^2\rangle_q}}\,, \tag{3.2}$$

with $\tilde{I}(\alpha,q) = I(\alpha,q) - \langle I(\alpha,q)\rangle_q$. For all further calculations only rotations perpendicular to the incident beam direction are considered, however, the results can be generalized for arbitrary rotation axes. Large-angle rotations can be reduced by the icosahedral symmetry of the sample and are not considered here.

In Fig. 3.3, we present the q-dependence of pattern correlations between snapshots of pure water layers calculated from two independent simulations using the same evolution

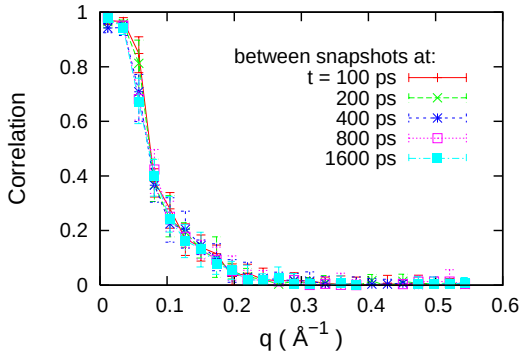

Figure 3.3: Demonstration of randomness in water layers obtained from molecular dynamics simulations: the pattern correlations between snapshots taken from two independent simulations at same time and at the same orientation. The error bars show the spread of correlation values along 10 randomly chosen orientations. The water layers have a 1.5 nm average thickness.

time. The correlations are calculated using Eq.(3.2) at the same orientation. The correlation curves do not show any significant change between 100 ps and 1.6 ns simulation time. This indicates that a random water layer around the virus is achieved after a single molecular dynamics simulation time of about 100 ps. There is almost no correlation for q larger than 0.2 Å^{-1}, while at low q, the water layers are still highly correlated due to their relatively stable shell shapes outside the virus. We study the effects of these random water layers on virus orientational classification by correlation analysis.

As an example, in Fig. 3.4, the diffraction pattern correlations between the STNV particles with WLs or PN were calculated as function of relative rotation angle at a given small q range ($[0.069, 0.104]$ Å^{-1}). In a purely mathematical treatment of the calculated diffraction patterns, for an ideal virus capsid, the correlation is trivially one for the same orientation and it decreases with the increasing angular difference in orientation (Fig. 3.4). In a more realistic model, after introducing Poisson noise and water layers of different thickness, the correlation of the diffraction images is significantly reduced. This increases the difficulty of identifying the orientation of the particles. The reduction of correlation, described by correlation fluctuations, originates from two parts: (i) heterogeneity of the sample, depending on the rotational symmetry of the virus, e.g. the correlation as a function of orientation even for perfect diffraction images depends slightly on the absolute orientation of the virus particle; and (ii) randomness in real space (WLs) or in reciprocal space due to the Poisson noise (PN). Here we would like to emphasize that the case with WL only is an unrealistic (statistically limiting) case. We show this case in order to evaluate the contribution of the diffraction from WLs, especially in the range of liquid water peak, unbiased by the statistical noise effects. However, only the full WL+PN case can be used to draw any experimentally feasible conclusions. The correlation curves calculated after including the PN/WL effect have a larger variance than in the pure virus case. Due to the limited number of patterns used in the diffraction simulations the variances are estimated within a limited accuracy. In

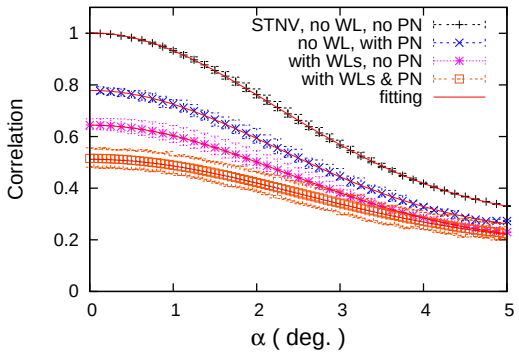

Figure 3.4: Examples of rotation-angle dependent correlation curves at the fixed range of $q = [0.069, 0.104]$ Å^{-1}: (1) correlation between noise-free patterns of pure STNV in different orientations; (2) STNV particle with water layers of 1.5 nm average thickness each from a different MD simulation; correlation between noise-free patterns for different orientations; (3) correlation as in (1), but patterns include Poisson noise at level of photon flux 10^{15} photons/μm^2 per pulse; (4) both WL+PN contributions are included. Error bars show estimated variance obtained for different absolute orientations and due to Poisson noise. The fitting function presented in Eq. (3.3) fits well the averaged correlation curves.

what follows we focus on the averaged correlation curves. However, it would be not enough for the average correlation to identify nearby patterns if the fluctuation variance would be too large. Then even nearby patterns would have a good chance of escaping detection.

The averaged correlation curves can be parameterized by a Gaussian fit:

$$G(\alpha, q) = a(q)\, e^{-\alpha^2/2b(q)^2} + c(q)\,, \tag{3.3}$$

with q-dependent fitting parameters a , b and c .

We fit the three parameters, using the correlation curves obtained from our simulations with fitting errors less than 2%. Results are shown in Fig. 3.5. The parameters $a(q)$ and $c(q)$, that determine the magnitude of the correlation, strongly depend on the imaged structure. They show the highest values for pure virus structure, and decrease significantly as soon as WL or PN are included. The rotation-independent background $c(q)$ always decreases strongly for high values of q. When "random" water layers are included, the parameters $a(q)$ and $c(q)$ are significantly suppressed at the range of the liquid water peak ($\sim (3\text{Å})^{-1}$). In the water layer case with average 2.5 nm thickness, the parameter $a(q)$ is decreasing to less than 0.1, which is comparable to the correlation variance. After including both WL and PN, the fitted $a(q)$ and $c(q)$ are smaller than in the cases with a WL or with PN only, implying a much reduced correlation.

Fig. 3.6 shows the parameter $b(q)$ for different cases. As can be seen, this parameter is determined only by the structure of virus. Adding WL and PN does not change the value of $b(q)$ that corresponds to half of the Shannon angle α_S, $\alpha_S = (2\, R_0\, q)^{-1}$, where R_0 is the

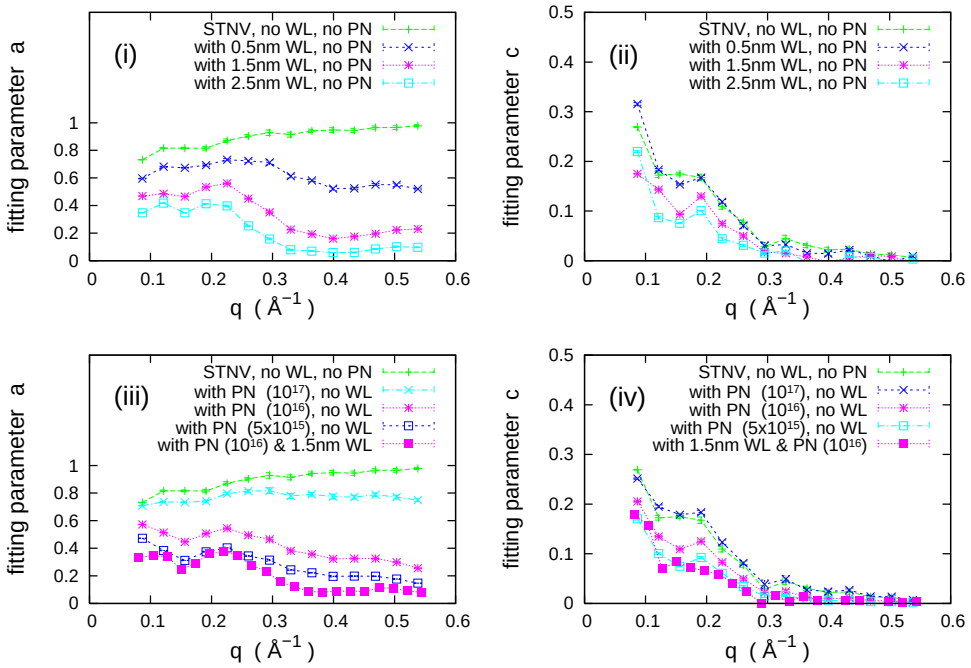

Figure 3.5: The q-dependence of fitting parameters $a(q)$ and $c(q)$ in cases: (i-ii) virus with water layers (WLs) only; (iii-iv) virus with Poisson noise (PN) only and virus with both WLs and PN. The unit for photon fluxes, which PN levels correspond to, is ph/μm^2 per pulse.

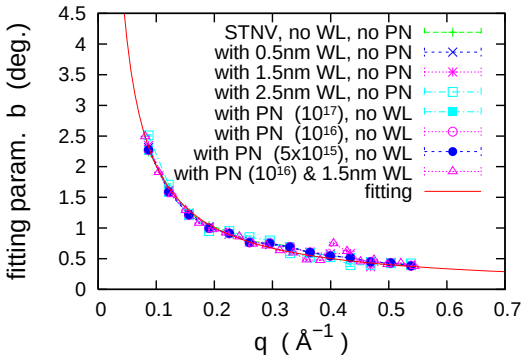

Figure 3.6: The q-dependence of the fitting parameter $b(q)$ for pure virus structure, and with WL and with PN included. The fit is $b(q) = (4\,R_0\,q)^{-1}$ (half of the Shannon angle) at the average virus radius, $R_0 \sim 71$ Å.

average virus radius. The Shannon angle denotes the q-dependent angular span of a Shannon speckle on the detector. The minimum rotation distance required to distinguish between two speckles corresponds to half of the Shannon angle. The Shannon angle is therefore the natural unit of orientational resolution (similarly to the definition of resolution in optical microscopy). Randomness introduced by WL or PN does not affect the reference resolution, given by half of α_S. This implies that the information about the structure that is contained in $b(q)$ is preserved after including WL or PN.

Therefore, the accuracy of the orientation of the patterns according to different rotation angles is determined by the parameters $a(q)$ and $c(q)$. Depending on the details of the reconstruction method, the orientational classification can be possible also at lower correlation values, assuming that their values are still above the statistical fluctuation level. We do not discuss any specific reconstruction methods here, since this is beyond the scope of this paper.

We would like also to emphasize that our analysis is based on the comparison of correlations between pairs of single patterns. Beyond this method, there are other sophisticated techniques to recover the orientation of the diffraction images via analysis of a large number of patterns [131, 130]. These methods can possibly reconstruct the image at lower levels of signal that is not accessible by the simple pattern-to-pattern correlation method. This would require further and more elaborate studies beyond the scope of this communication.

Finally, we state that in our diffraction simulations, we have simulated only the empty capsid without filling it with RNA genome. The RNA structure inside a virus capsid appears to be disordered as determined from single particle EM analyses. Similar to these methods, it is expected that its contribution will average out for the large number of exposures considered here.

Summary

We have investigated a possible loss of orientational and structural information due to the presence of a water layer surrounding the imaged object, using the pattern-to-pattern correlation method. Our analysis shows that liquid water layers reduce the orientational information. The thicker the water layer, the more difficult the orientational classification is. The structural information is blurred at values of q above the liquid water peak position ($\sim (3\text{Å})^{-1}$) which also indicates the achievable orientational resolution by the corresponding Shannon angle.

It has been shown through simulations that a water layer of a certain thickness slows down the Coulomb expansion of the virus particle [53, 69, 136, 137]. Depending on the size of the virus, there is an optimal thickness of the water layer, where the structure is preserved and possibly without too large reduction in the orientational and structural information contained in diffraction patterns.

3.3 Summary and outlook

There are some challenges in 3D CDI with FELs, especially for biological particles. The idea of an imaged object coated with a thick tamper, such as a layer of liquid water, can be used to reduce radiation damage during FEL illumination. Coating layers of liquid water with efficient thickness have significant diffraction signals at the peak range of liquid water ($\sim (3\text{Å})^{-1}$). Randomness in such water layers leads to obvious suppression of pattern-pair correlations at this signal range, even between the patterns in a same view. The orientation information is statistically preserved in the patterns, but the correlation contrast becomes lower, and this increases the difficulty in recognizing the orientations, especially in the water peak range. However, it is quite plausible to recover orientation of each pattern beyond the water peak range.

A future data model could be built on GTM or EMC if their computation performances are improved significantly. The data model should include diffraction effects from radiation damage (and the tamper effect as well, if applied), such as scattering ability of ions, free electron gas and accumulation over pulse length. The signal background might be included into the model, such as that from incoherent scattering or an imperfect imaging environment. Because it might be significant when SNR is too low.

Variation in conformations of a bioparticle seems inevitable when it is prepared in liquid water at room temperature by current spraying techniques. Therefore, "identical" objects used for 3D imaging are not perfectly identical, and this will degrade resolution to the level of typical length scale of the conformation variance [142]. The same problem occurs in single particle cryo-EM, which can achieve best resolutions around 8 Å [143, 144]. The newly emerging techniques, such as manifold mapping [145], are used to extract possible conformations from a large number of measured patterns. This kind of method allows constructing conformation models directly from imaging experiments, which is also one of the great interests of structural biology.

It will be challenging to build a complete data model with above possible effects considered, and to isolate reliable 3D structural information about "identical" objects as much as possible.

Returning to the orientation problem, there are some ideas and techniques which are potentially useful to determine the orientations of flying particles. For example, rare species of ions such as sulphur in an irradiated particle can be used to estimate orientation of the particle by Velocity Map Imaging (VMI) techniques, if such ions have preference of escaping directions. Gas-phase particles with polarity could be aligned by a laser pulse before a FEL imaging pulse. The estimated orientation information may make a data model easier to handle low SNR data.

There are also some possible ways to increase SNR in imaging of biological particles. For example, holography [146] can be extended to image bioparticles [134, 147] with specific considerations of geometry or reference. In a similar way, Shinktake [110] suggested to use

gold balls as spectators in imaging of bioparticles. Actually, the strong scattering spectators do not significantly increase the scattering information from weak bioparticles due to the large contrast between them [80]. It may help when objects have comparable scattering ability, for example, using a number of copies of bioparticles in one imaging window to increase diffraction signals. There are several variants of this case: (i) the copies are randomly assemble in the same object plane [85, 148], and averaged structure information can be obtained from single-shot patterns. (ii) the copies are aligned in one direction using polarity properties of neutral molecules [149], and meaningful structure or dynamics information stays in diffraction patterns along the aligning direction. (iii) nanocrystals (the copies are fully 3D ordered on normal lattice) have a much better SNR (while there exists a finite size effect, i.e. satellite Bragg's peaks), and it can potentially solve those proteins for which only small crystals are available, at comparable resolution as X-ray crystallography.

Beyond the scheme of 3D CDI with FELs discussed in § 3.1, there are potential techniques that could extract sufficient 3D information from single 2D diffraction patterns, although this is still an open question. If some reliable techniques appear in this direction, it would change the current situation of 3D CDI with FELs.

There are many interesting ideas and techniques, as mentioned above, related to biological imaging with FELs on front of us. With more FEL facilities (such as LCLS II and European XFEL) going into operations, it is expected that lots of exciting progress ahead would be made in this new field.

Appendix A

Algorithm in Molecular Dynamics simulations

Molecular Dynamics (MD) is a general algorithm for simulation of time evolution of a molecule or a system constituting of point particles with mutual interactions. The motion of each particle is classical and is described by Newton's equations:

$$\frac{\partial \mathbf{r}_i}{\partial t} = \mathbf{v}_i \,,$$
$$\frac{\partial \mathbf{v}_i}{\partial t} = \frac{\mathbf{F}_i}{m_i} \,,$$

where $(\mathbf{r}_i, \mathbf{v}_i)$ are six degrees of freedom (DOF) in phase space for ith particle, and $\mathbf{F}_i$ is a force sum that this particle experiences from other particles or background field. For a system with N particles, determination of its evolution requires the solution of ordinary differential equations in $6N$ dimensions:

$$\frac{\partial y}{\partial t} = f(t, y) \,, \tag{A.1}$$

where y is a vector to represent all DOF in phase space with initial conditions $y(t_0) = y_0$. In MD, the problem is solved numerically by discrete integration over finite time steps. $f(t, y)$ is updated each time step, and is determined by the configuration of y in previous time step. The numerical integration in a single time step is critical to simulation accuracy. There are many sophisticated integration algorithms such as Verlet-Stoermer integration and Runge-Kutta integration.

In this thesis, the Runge-Kutta-Fehlberg integrator at 7(8)th order (RKF78) [150] is applied. The formula for integration of a single time step Δt is:

$$y_{n+1} = y_n + \Delta t \sum_{\alpha=0}^{12} c_\alpha k_\alpha \,, \tag{A.2}$$

where

$$k_0 = f(t_n, y_n)\,;$$
$$k_\alpha = f(t_n + a_\alpha \Delta t, y_n + \Delta t \sum_{\beta=0}^{\alpha-1} b_{\alpha\beta} k_\beta) \quad (\alpha > 0)\,.$$

The truncation error in one step is at the order of $(\Delta t)^7$, which is estimated by following formula:

$$\mathrm{T}_{err} = \frac{41}{840}\Delta t\,(k_0 + k_{10} - k_{11} - k_{12})\,. \tag{A.3}$$

When the error goes beyond the tolerable error range for a single step, the integration should be calculated again in this step with smaller time interval Δt. The relevant coefficients are listed in the following Butcher tableau.

	a_α	$b_{\alpha\beta}$												$\tilde{c}_\alpha$	c_α
$\alpha\backslash\beta$		0	1	2	3	4	5	6	7	8	9	10	11		
0	0	0												$\frac{41}{840}$	0
1	$\frac{2}{27}$	$\frac{2}{27}$												0	
2	$\frac{1}{9}$	$\frac{1}{36}$	$\frac{1}{12}$											0	
3	$\frac{1}{6}$	$\frac{1}{24}$	0	$\frac{1}{8}$										0	
4	$\frac{5}{12}$	$\frac{5}{12}$	0	$-\frac{25}{16}$	$\frac{25}{16}$									0	
5	$\frac{1}{2}$	$\frac{1}{20}$	0	0	$\frac{1}{4}$	$\frac{1}{5}$								$\frac{34}{105}$	
6	$\frac{5}{6}$	$-\frac{25}{108}$	0	0	$\frac{125}{108}$	$-\frac{65}{27}$	$\frac{125}{54}$							$\frac{9}{35}$	
7	$\frac{1}{6}$	$\frac{31}{300}$	0	0	0	$\frac{61}{225}$	$-\frac{2}{9}$	$\frac{13}{900}$						$\frac{9}{35}$	
8	$\frac{2}{3}$	2	0	0	$-\frac{53}{6}$	$\frac{704}{45}$	$-\frac{107}{9}$	$\frac{67}{90}$	3					$\frac{9}{280}$	
9	$\frac{1}{3}$	$-\frac{91}{108}$	0	0	$\frac{23}{108}$	$-\frac{976}{135}$	$\frac{311}{54}$	$-\frac{19}{60}$	$\frac{17}{6}$	$-\frac{1}{12}$				$\frac{9}{280}$	
10	1	$\frac{2383}{4100}$	0	0	$-\frac{341}{164}$	$\frac{4496}{1025}$	$-\frac{301}{82}$	$\frac{2133}{4100}$	$\frac{45}{82}$	$\frac{45}{164}$	$\frac{18}{41}$			$\frac{41}{840}$	0
11	0	$\frac{3}{205}$	0	0	0	0	$-\frac{6}{41}$	$-\frac{3}{205}$	$-\frac{3}{41}$	$\frac{3}{41}$	$\frac{6}{41}$	0		0	$\frac{41}{840}$
12	1	$-\frac{1777}{4100}$	0	0	$-\frac{341}{164}$	$\frac{4496}{1025}$	$-\frac{289}{82}$	$\frac{2193}{4100}$	$\frac{51}{82}$	$\frac{33}{164}$	$\frac{12}{41}$	0	1	0	$\frac{41}{840}$

The most time consuming parts of computation in MD simulations are calculations of mutual interactions among N particles, which are usually done using loops. They scale with particle number as N^2. There are many sophisticated techniques to minimize such computational costs within acceptable accuracy. For example, the weak two-body interactions which act over long distances, such as that due to Coulomb potential, can be simplified by multipole approximation. In perfect cases the scaling behavior can be reduced to $N \ln N$. The MD programs developed for this thesis is not optimized, and can only deal with small numbers of particles.

Appendix B

Experimental cross section data

All cross section (CS) data in this part come from experimental measurements. For convenience of using these data in simulation programs, some CS data are parameterized by empirical formulas with respective fitting plots shown. Note that relevant references can be found in the plots.

Photoionization cross sections

$E_\gamma = 12.7\,\mathrm{eV}\,(100\,\mathrm{nm})\,,\ \sigma_\gamma(Xe^{0+} \to Xe^{1+}) = 0.40\,\text{Å}^2\,,\ \sigma_{2\gamma}(Ar^{0+} \to Ar^{1+}) = 0.010\,\text{Å}^2\,;$

$E_\gamma = 37.8\,\mathrm{eV}\,(32\,\mathrm{nm})\,,\ \sigma_\gamma(Ar^{0+} \to Ar^{1+}) = 0.050\,\text{Å}^2\,,\ \sigma_\gamma(Ar^{1+} \to Ar^{2+}) = 0.026\,\text{Å}^2\,;$

$E_\gamma = 90\ \mathrm{eV}\,(14\,\mathrm{nm})\,,\ \sigma_\gamma^{tot}(Xe) = 0.24\,\text{Å}^2\,;$

$E_\gamma = 1.8\,\mathrm{keV}\,(7.0\,\text{Å})\,,\ \sigma_\gamma^{tot}(Xe) = 5.6 \times 10^{-3}\,\text{Å}^2\,;$

$E_\gamma = 8.3\,\mathrm{keV}\,(1.5\,\text{Å})\,,\ \sigma_\gamma^{tot}(Xe) = 6.0 \times 10^{-4}\,\text{Å}^2\,.$

Note that 1 $\text{Å}^2 = 100$ Mb. References:
J.A.R. Samson and W.C. Stolte, J. Electron Spectrosc. Relat. Phenom. **123**(2002)265
J.B. West and J. Morton, At. Data Nucl. Data Tab. **22**(1978)103

Electron impact cross sections: argon

Total cross section

$$\sigma(E) = \begin{cases} A_0 + A_1 ln(E) + A_2 ln(E)^2 + A_3 ln(E)^3 + A_4 ln(E)^4\,, & E \le 13.5\,eV\,; \\ B_0 + B_1 e^{-E/B_2} + B_3 e^{-E/B_4}\,, & E > 13.5\,eV\,. \end{cases} \tag{B.1}$$

The following parameters A_i , B_i $(i = 0, 1, 2, 3, 4)$ are fitted from experimental data. The units for the parameters are (Å^2 , eV).

subscript	A	B
0	1.29	2.11
1	1.79	29.8
2	1.16	17.2
3	0.405	8.12
4	0.102	259.7

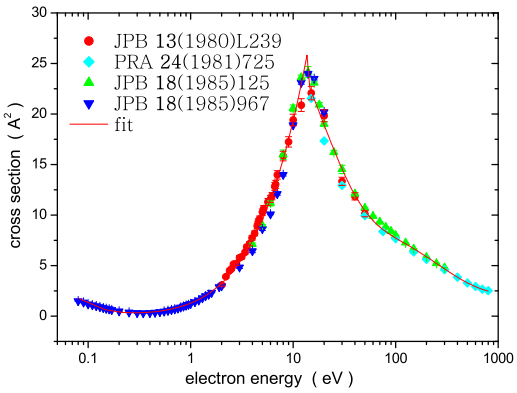

Single ionization

$$\sigma_q(E) = e^A \left(1 - \frac{I_q}{E}\right)^c \ln\left(\frac{E}{I_q}\right) \frac{I_q}{E}, \tag{B.2}$$

with ionization energy I_q for $Ar^{(q-1)+} \longrightarrow Ar^{q+}$. The fitting values of parameters A and c are listed in the Table B.1. The fitting plots are shown below. (units: Å^2 , eV)

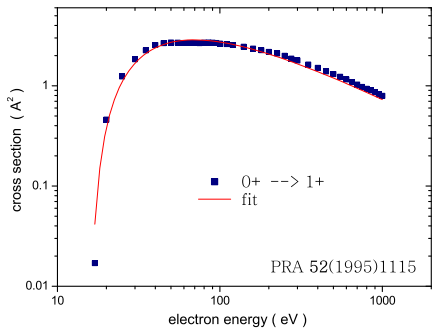

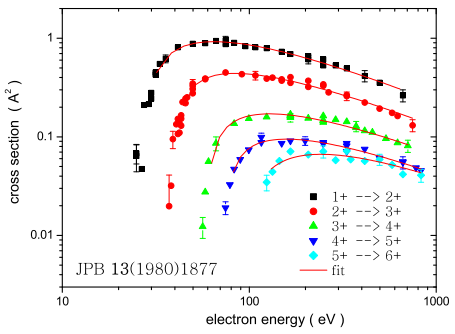

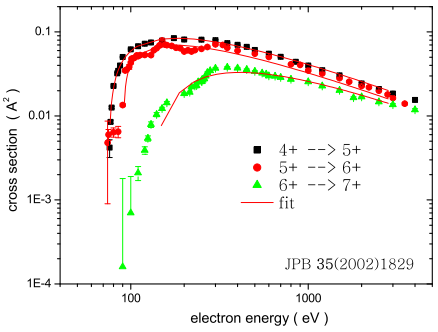

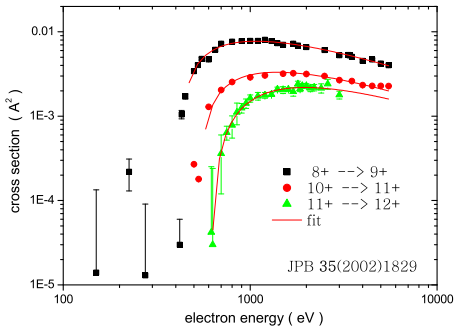

Table B.1: Electron impact ionization cross sections for Argon. (unit: $Å^2$)

	I_q	Ref.[1]		Ref.[2]		Ref.[3]	
$Ar^{q-1} \longrightarrow Ar^q$	(eV)	A	c	A	c	A	c
$0+ \longrightarrow 1+$	15.8	2.427	1.101				
$1+ \longrightarrow 2+$	27.6			0.802	-0.233		
$2+ \longrightarrow 3+$	40.9			-0.052	-0.419		
$3+ \longrightarrow 4+$	59.7			-0.952	-0.350		
$4+ \longrightarrow 5+$	75.2			-1.564	-0.385	-1.577	-0.207
$5+ \longrightarrow 6+$	91.2			-1.732	-0.046	-1.956	-0.509
$6+ \longrightarrow 7+$	125					-2.262	0.370
$7+ \longrightarrow 8+$	143						
$8+ \longrightarrow 9+$	423					-3.916	-0.114
$9+ \longrightarrow 10+$	479						
$10+ \longrightarrow 11+$	539					-4.746	-0.081
$11+ \longrightarrow 12+$	618					-5.000	0.300

[1] H. Straub, Phys.Rev. A **52**(1995)1115

[2] A. Muller et. al., J.Phys. B **13**(1980)1877

[3] H. Zhang et. al., J.Phys. B **35**(2002)1829

Electron impact cross sections: xenon

(Fitting results provided by Beata Ziaja)

Total cross section

$$\sigma(E) = E^a \cdot e^b \,. \tag{B.3}$$

The parameters are listed below with unit cm^2 .

$E(eV)$	a	b
[0. , 0.8]	-1.50	-36.80
[0.8 , 5.0]	1.70	-36.17
[5.0 , 9.0]	0.0	-33.38
[9.0 , $+\infty$]	-0.55	-32.20

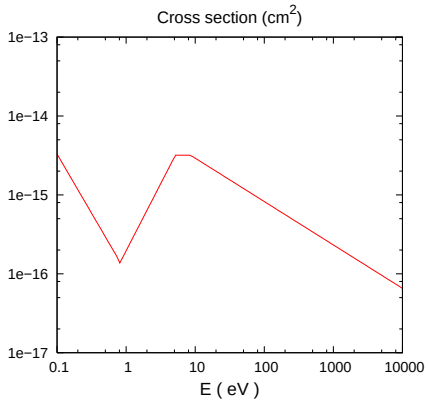

Single ionization

Similar fitting formula as Eq.(B.2) with unit cm^2.

$Xe^{q-1} \longrightarrow Xe^q$	$I_q(eV)$	A	c
0+ $\longrightarrow$ 1+	12.1	-33.90	0.40
1+ $\longrightarrow$ 2+	21.2	-35.12	-0.36
2+ $\longrightarrow$ 3+	32.1	-35.96	-0.72
3+ $\longrightarrow$ 4+	46.7	-36.30	-0.48
4+ $\longrightarrow$ 5+	59.7	-36.60	-0.82
5+ $\longrightarrow$ 6+	71.8	-36.56	-0.48
6+ $\longrightarrow$ 7+	92.1	-36.83	-0.32
7+ $\longrightarrow$ 8+	105.9	-37.36	-0.38

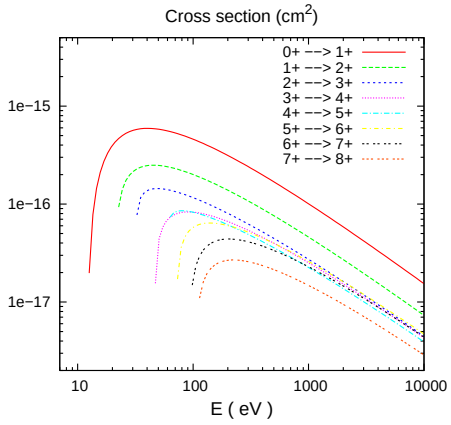

Appendix C

Cross section formula

Energy-splitting in electron-impact ionization

In electron-impact ionization, the intrinsic momentum distribution of a bound electron being ionized leads to a broadened distribution of outgoing energy. It is described by the *binary-encounter-dipole* (BED) model [37, 38]:

$$\frac{d\sigma(E_s; E_{in}, E_{_I})}{dE_s} \propto \frac{1}{(E_{in} - E_s)^3} + \frac{1}{(E_{_I} + E_s)^3} \equiv f(E_s; E_{in}, E_{_I})\,, \tag{C.1}$$

where E_{in} , E_s are kinetic energies of the incident electron and the outgoing second electron respectively, and $E_{_I}$ is the ionization energy. The formula implies $E_{in} \geq E_{_I} + E_s$ which keeps the energy conservation in the process of ionization. The left energy $E_k \equiv E_{in} - E_{_I}$ splits into two pieces of kinetic energies for two outgoing electrons. The cross section is symmetrically distributed on two splits of the kinetic energies: E_s and $E_k - E_s$.

Practically, the cumulative probability is convenient for realization of the distribution in simulations. The probability of the energy splitting at E_s is normalized as:

$$\begin{aligned} \mathrm{R}(E_s) &= \frac{\int_0^{E_s} f(E_s; E_{in}, E_{_I})\, dE_s}{\int_0^{E_k} f(E_s; E_{in}, E_{_I})\, dE_s} \\ &= \frac{E_{in}^2 E_{_I}^2 \left[(E_{_I} + E_s)^2 - (E_{in} - E_s)^2\right]}{2(E_{in}^2 - E_{_I}^2)(E_{_I} + E_s)^2(E_{in} - E_s)^2} + \frac{1}{2}\,. \end{aligned} \tag{C.2}$$

It is a monotone function due to accumulation of positive numbers. The inverse dependence of E_s on R is complicated and can be evaluated numerically based on the monotone property. The numerically obtained E_s follows the splitting distribution in Eq (C.1) when the probability R is uniform. In simulations, R is a random number in range (0,1) to decide the splitting energy E_s .

Cross section formula for three-body recombination

The recombination process is treated as an inverse collisional ionization process in § 1.4 based on the principle of detailed balance. In the MD simulations, three-body recombination, $2e + I^{n+} \rightarrow e + I^{(n-1)+}$, is assumed to be dominant in recombination processes. The estimated cross sections for three-body recombination can be defined through that of electron-impact ionizations:

$$\sigma_{RC}^{n\rightarrow n-1}(E_{in}) = \frac{g_{n-1}}{g_n}\,\frac{\rho_e \lambda_e^3}{2}\,\sigma_{CI}^{n-1\rightarrow n}(E_I + 2E_{in})\,, \tag{C.3}$$

with n ion charge, E_{in} kinetic energy of the incident electron to be absorbed by the ion, ρ_e ion density and E_I ionization energy for $q-1$ charge state to q. g_n is the statistical weight of the bound energy level of a ion with charge n. The $\lambda_e = h^3/\sqrt{2\pi m_e k T_e}$ is the thermal de Broglie wavelength of free electrons. The formula assumes that the kinetic energies of electrons in recombination follow the Maxwell-Boltzmann distribution and the spectator electron has comparable kinetic energy to the one to be recombined.

Appendix D

Rotation representation

Euler angles

The most common definition of a 3D rotation is its representation by Euler angles, ϕ , θ , and ψ . In so-called x-convention: rotation is firstly by an angle ϕ around the z-axis; then by an angle θ around new x-axis; and finally by an angle ψ around new z-axis. ϕ , $\psi \in (0, 2\pi]$, $\theta \in (0, \pi]$. The corresponding rotation matrix is

$$\mathbf{R}(\phi\,,\,\theta\,,\,\psi) = \begin{pmatrix} c_\psi & s_\psi & 0 \\ -s_\psi & c_\psi & 0 \\ 0 & 0 & 1 \end{pmatrix} \begin{pmatrix} 1 & 0 & 0 \\ 0 & c_\theta & s_\theta \\ 0 & -s_\theta & c_\theta \end{pmatrix} \begin{pmatrix} c_\phi & s_\phi & 0 \\ -s_\phi & c_\phi & 0 \\ 0 & 0 & 1 \end{pmatrix}$$

$$= \begin{pmatrix} c_\psi c_\phi - c_\theta s_\phi s_\psi & c_\psi s_\phi + c_\theta c_\phi s_\psi & s_\psi s_\theta \\ -s_\psi c_\phi - c_\theta s_\phi c_\psi & -s_\psi s_\phi + c_\theta c_\phi c_\psi & c_\psi s_\theta \\ s_\theta s_\phi & -s_\theta c_\phi & c_\theta \end{pmatrix},$$

with the convention $s_A \equiv \sin A$ and $c_A \equiv \cos A$. If the matrix elements R_{32} , R_{23} are nonzero, Euler angles can be expressed as following:

$$\phi = \tan^{-1}\left(-\frac{R_{31}}{R_{32}}\right),\ \theta = \cos^{-1}(R_{33}),\ \psi = \tan^{-1}\left(\frac{R_{13}}{R_{23}}\right).$$

Quaternions

Compared to the representations of Euler angles and rotation matrices, unit quaternions provide a simple and direct notation for 3D rotations. It has the advantage of numerical robustness in applications. For a vector $\vec{v}$ rotated by angle α around the $\vec{u}$ (unit vector) direction,

$$\vec{v'} = q\,\vec{v}\,q^{-1}\,, \quad q = \cos\left(\frac{\alpha}{2}\right) + \vec{u}\,\sin\left(\frac{\alpha}{2}\right) = q_0 + q_1\mathbf{i} + q_2\mathbf{j} + q_3\mathbf{k}\,,$$

with $\mathbf{i}^2 = \mathbf{j}^2 = \mathbf{k}^2 = \mathbf{ijk} = -1$ and $q_0^2 + q_1^2 + q_2^2 + q_3^2 = 1$. The corresponding orthogonal rotation matrix is:

$$\mathbf{R}(q_0, q_1, q_2, q_3) = \begin{pmatrix} 1 - 2(q_2^2 + q_3^2) & 2(q_1 q_2 - q_0 q_3) & 2(q_0 q_2 + q_1 q_3) \\ 2(q_0 q_3 + q_1 q_2) & 1 - 2(q_1^2 + q_3^2) & 2(q_2 q_3 - q_0 q_1) \\ 2(q_1 q_3 - q_0 q_2) & 2(q_0 q_1 + q_2 q_3) & 1 - 2(q_1^2 + q_2^2) \end{pmatrix} .$$

The trace of the matrix is

$$Tr(\mathbf{R}) = 4q_0^2 - 1\,, \text{ with } q_0 = \cos\left(\frac{\alpha}{2}\right) .$$

Therefore, from the rotation matrix we can obtain the angle for direct single rotation:

$$\cos\alpha = \frac{1}{2}\left[Tr(\mathbf{R}) - 1\right] .$$

List of Figures

List of Tables

Bibliography

[1] V. Ayvazyan et al. Generation of GW radiation pulses from a VUV free-electron laser operating in the femtosecond regime. Phys. Rev. Lett., 88:104802, 2002.

[2] V. Ayvazyan et al. A new powerful source for coherent VUV radiation: Demonstration of exponential growth and saturation at the TTF free-electron laser. Eur. Phys. J. D, 20:149, 2002.

[3] H. Wabnitz et al. Multiple ionization of atom clusters by intense soft X-rays from a free electron laser. Nature, 420:482, 2002.

[4] H. Wabnitz. Interaction of intense VUV radiation from FEL with rare gas atoms and clusters. Ph.D. thesis, DESY-THESIS-2003-026, 2003.

[5] R. Santra and C.H. Greene. Xenon clusters in intense VUV laser fields. Phys. Rev. Lett., 91:233401, 2003.

[6] Z.B. Walters, R. Santra, and C.H. Greene. Interaction of intense VUV radiation with large xenon clusters. Phys. Rev. A, 74:043204, 2006.

[7] C. Siedschlag and J-M. Rost. Small rare-gas clusters in soft X-ray pulses. Phys. Rev. Lett., 93:043402, 2004.

[8] I. Georgescu, U. Saalmann, and J.M. Rost. Clusters under strong VUV pulses: A quantum-classical hybrid description incorporating plasma effects. Phys. Rev. A, 76:043203, 2007.

[9] C. Jungreuthmayer, L. Ramunno, J. Zanghellini, and T. Brabec. Intense VUV laser cluster interaction in the strong coupling regime. J. Phys. B: At. Mol. Opt. Phys., 38:3029, 2005.

[10] G.J. Pert. Inverse bremsstrahlung in strong radiation fields – the Born approximation re-examined. J. Phys. B: At. Mol. Opt. Phys., 29:1135, 1996.

[11] A. Brantov et al. Enhanced inverse bremsstrahlung heating rates in a strong laser field. Phys. Plasmas, 10:3385, 2003.

[12] N.M. Kroll and K.M. Watson. Charged-particle scattering in the presence of a strong electromagnetic wave. Phys. Rev. A, 8:804, 1973.

[13] R. R. Fäustlin et al. Observation of ultrafast nonequilibrium collective dynamics in warm dense hydrogen. Phys. Rev. Lett., 104:125002, 2010.

[14] V.P. Krainov and M.B. Smirnov. Cluster beams in the super-intense femtosecond laser pulse. Phys. Rep., 370:237, 2002.

[15] V.P. Krainov. Inverse stimulated bremsstrahlung of slow electrons under Coulomb scattering. J. Phys. B: At. Mol. Opt. Phys., 33:1585, 2000.

[16] A. Tronnier. Absorption von VUV-photonen in warm dense matter. Ph.D. thesis, Technische Universit01t Mnchen, 2007.

[17] S. Atzeni and J. Meyer-ter Vehn. The Physics of Inertial Fusion: Beam Plasma Interaction, Hydrodynamics, Hot Dense Matter. Oxford University Press, 2004.

[18] A.R.B. de Castro et al. Non-linear phenomena in atoms and clusters induced by intense VUV radiation from a free electron laser. J. Elec. Spec. Rel. Phenom., 144:3, 2005.

[19] T. Laarmann et al. Emission of thermally activated electrons from rare gas clusters irradiated with intense VUV light pulses from a free electron laser. Phys. Rev. Lett., 95:063402, 2005.

[20] A.R.B. de Castro et al. Spectroscopy of rare gas clusters using VUV light from a free-electron-laser. J. Elec. Spec. Rel. Phenom., 156:25, 2007.

[21] T. Laarmann et al. Interact ion of argon clusters with intense VUV-laser radiation: the role of electronic structure in the energy-deposition process. Phys. Rev. Lett., 92:143401, 2004.

[22] J. Schulz et al. Energy absorption of free rare gas clusters irradiated by intense VUV pulses of a free electron laser. Nucl. Instrum. Methods Phys. Res., Sect. B, 507:572, 2003.

[23] D. Bauer. Small rare gas clusters in laser fields: ionization and absorption at long and short laser wavelengths. J. Phys. B: At. Mol. Opt. Phys., 37:3085, 2004.

[24] U. Saalmann, C. Siedschlag, and J.M. Rost. Mechanisms of cluster ionization in strong laser pulses. J. Phys. B: At. Mol. Opt. Phys., 39:R39, 2006.

[25] B.H. Bransden and C.J. Joachain. Physics of Atoms and Molecules.

[26] C. Deiss et al. Laser-cluster interaction: X-ray production by short laser pulses. Phys. Rev. Lett., 96:013203, 2006.

[27] B. Ziaja, A.R.B. de Castro, E. Weckert, and T. Moeller. Modelling dynamics of samples exposed to free-electron-laser radiation with Boltzmann equations. Eur. Phys. J. D, 40:465, 2006.

[28] B. Ziaja, H. Wabnitz, E. Weckert, and T. Moeller. Femtosecond non-equilibrium dynamics of clusters irradiated with short intense VUV pulses. New J. Phys., 10:043003, 2008.

[29] B. Ziaja, H. Wabnitz, E. Weckert, and T. Moeller. Atomic clusters of various sizes irradiated with short intense pulses of VUV radiation. Europhys. Lett., 82:24002, 2008.

[30] R.H. Garvey, C.H. Jackman, and A.E.S. Green. Independent-particle-model potentials for atoms and ions with 36<Z<54 and a modified Thomas-Fermi atomic energy formula. Phys. Rev. A, 12:1144, 1975.

[31] M.S. Murillo and J.C. Weisheit. Dense plasmas, screened interactions, and atomic ionization. Phys. Rep., 302:1, 1998.

[32] Y. Hahn. Plasma density effects on the three-body recombination rate coefficients. Phys. Lett. A, 231:82, 1997.

[33] S. Eliezer. The interaction of high-power lasers with plasmas. IOP Publishing, 2002.

[34] Y. Ochi, I. Golovkin, R. Mancini, and I. Uschmann. Temporal evolution of temperature and density profiles of a laser compressed core. Rev. of Scient. Instr., 74:1683, 2003.

[35] J. Oxenius. Kinetic theory of particles and photons, page 21. Springer-Verlag, Berlin, 1986.

[36] H.K. Chung et al. FLYCHK: Generalized population kinetics and spectral model for rapid spectroscopic analysis for all elements. High Energy Density Phys., 1:3, 2005.

[37] Y. Kim and M. Eugene Rudd. Binary-encounter-dipole model for electron-impact ionization. Phys. Rev. A, 50:3954, 1994.

[38] Y. Kim, J.P. Santos, and F. Parente. Extension of the binary-encounter-dipole model to relativistic incident electrons. Phys. Rev. A, 62:052710, 2000.

[39] J. Colgan et al. Recent developments in the modeling of dense plasmas. AIP Conf. Proc., 926:180, 2007.

[40] H. Tawara and T. Kato. Total and partial ionization cross sections of atoms and ions by electron impact. At. Data and Nucl. Data Tabl., 36:167, 1987.

[41] Y. Ralchenko et al. NLTE-4 Database. http://nlte.nist.gov/NLTE4/.

[42] F. Wang, E Weckert, and B. Ziaja. Inverse bremsstrahlung cross section estimated within evolving plasmas using effective ion potentials. J. Plasma Phys., 75:289, 2009.

[43] B. Ziaja, H. Wabnitz, F. Wang, E. Weckert, and T. Moeller. Energetics, ionization, and expansion dynamics of atomic clusters irradiated with short intense vacuum-ultraviolet pulses. Phys. Rev. Lett., 102:205002, 2009.

[44] R. Neutze, R. Wouts, D. van der Spoel, E. Weckert, and J. Hajdu. Potential for biomolecular imaging with femtosecond X-ray pulses. Nature, 406:752, 2000.

[45] DESY. Technical Design Report of the European XFEL. ISBN 3-935702-17-5 5, 7-9 2006.

[46] LCLS. LCLS: The first experiments. SSRL, SLAC, Stanford, USA, 2000.

[47] T. Shintake et al. (SCSS Team). Proceedings of FEL 2006, page 33. BESSY, Berlin, 2006.

[48] XFEL-info. 2007.

[49] C. Bostedt et al. Multistep ionization of argon clusters in intense femtosecond extreme ultraviolet pulses. Phys. Rev. Lett., 100:133401, 2008.

[50] J. Miao, K.O. Hodgson, and D. Sayre. An approach to three-dimensional structures of biomolecules by using single-molecule diffraction images. Proc. Natl Acad. Sci., 98:6641, 2001.

[51] Z. Jurek, G. Oszlanyi, and G. Faigel. Imaging atom clusters by hard X-ray free-electron lasers. Europhys. Lett., 65:491, 2004.

[52] S.P. Hau-Riege et al. Pulse requirements for X-ray diffraction imaging of single biological molecules. Phys. Rev. E, 71:061919, 2005.

[53] S.P. Hau-Riege et al. Encapsulation and diffraction-pattern-correction methods to reduce the effect of damage in X-ray diffraction imaging of single biological molecules. Phys. Rev. Lett., 98:198302, 2007.

[54] Henry N. Chapman et al. Femtosecond diffractive imaging with a soft-X-ray free-electron laser. Nat. Phys., 2:839, 2006.

[55] M. Rusek and A. Orlowski. Different mechanisms of cluster explosion within a unified smooth particle hydrodynamics Thomas-Fermi approach: Optical and short-wavelength regimes compared. Phys. Rev. A, 71:043202, 2005.

[56] M. Hoener et al. Charge recombination in soft X-ray laser produced nanoplasmas. J. Phys. B: At. Mol. Opt. Phys., 41:181001, 2008.

[57] Z. Jurek, G. Faigel, and M. Tegze. Dynamics in a cluster under the influence of intense femtosecond hard X-ray pulses. Eur. Phys. J. D, 29:217, 2004.

[58] S.P. Hau-Riege, R.A. London, and A. Szoeke. Dynamics of biological molecules irradiated by short X-ray pulses. Phys. Rev. E, 69:051906, 2004.

[59] H. Thomas et al. Shell explosion and core expansion of xenon clusters irradiated with intense femtosecond soft X-ray pulses. J. Phys. B: At. Mol. Opt. Phys., 42:134018, 2009.

[60] H. Iwayama et al. Frustration of direct photoionization of Ar clusters in intense extreme ultraviolet pulses from a free electron laser. J. Phys. B: At. Mol. Opt. Phys., 42:134019, 2009.

[61] B.F. Murphy et al. Explosion of xenon clusters driven by intense femtosecond pulses of extreme ultraviolet light. Phys. Rev. Lett., 101:203401, 2008.

[62] C. Bostedt et al. Experiments at FLASH. Nucl. Instrum. Methods Phys. Res. A, 601:108, 2009.

[63] T. Fennel et al. Laser-driven nonlinear cluster dynamics: from single- and multiphoton excitations to the strong-field domain. arXiv:0904.2706, 2009.

[64] U. Saalmann, I. Georgescu, and J.M. Rost. Tracing non-equilibrium plasma dynamics on the attosecond time scale in small clusters. New. J. Phys., 10:025014, 2008.

[65] I. Georgescu, U. Saalmann, and J.M. Rost. Attosecond resolved charging of ions in a rare-gas cluster. Phys. Rev. Lett., 99:183002, 2007.

[66] M. Rusek, H. Lagadec, and T. Blenski. Cluster explosion in an intense laser pulse: Thomas-Fermi model. Phys. Rev. A, 63:013203, 2000.

[67] C. Siedschlag and J-M. Rost. Electron release of rare-gas atomic clusters under an intense laser pulse. Phys. Rev. Lett., 89:173401, 2002.

[68] M. Arbeiter and T. Fennel. private communication. 2009.

[69] Z. Jurek and G. Faigel. The effect of tamper layer on the explosion dynamics of atom clusters. Eur. Phys. J. D, 50:35, 2008.

[70] Z. Jurek and G. Faigel. The effect of inhomogenities on single-molecule imaging by hard XFEL pulses. Europhys. Lett., 86:68003, 2009.

[71] H.N. Chapman. X-ray imaging beyond the limits. Nature Materials, 8:299, 2009.

[72] A.L. Cavalieri et al. Attosecond spectroscopy in condensed matter. Nature, 449:1029, 2007.

[73] Jianwei Miao, Pambos Charalambous, Janos Kirz, and David Sayre. Extending the methodology of X-ray crystallography to allow imaging of micrometre-sized non-crystalline specimens. Nature, 400:342, 1999.

[74] M.A. Pfeifer et al. Three-dimensional mapping of a deformation field inside a nanocrystal. Nature, 442:63, 2006.

[75] H. N. Chapman et al. High-resolution ab initio three-dimensional X-ray diffraction microscopy. Journal of the Optical Society of America A, 23:1179, 2006.

[76] D. Shapiro et al. Biological imaging by soft X-ray diffraction microscopy. Proc. Natl Acad. Sci. USA, 102:15343, 2005.

[77] P. Thibault, V. Elser, C. Jacobsen, D. Shapiro, and D. Sayre. Reconstruction of a yeast cell from X-ray diffraction data. Acta Cryst. A, 62(4):248, 2006.

[78] Y. Nishino, Y. Takahashi, N. Imamoto, T. Ishikawa, and K. Maeshima. Three-dimensional visualization of a human chromosome using coherent X-ray diffraction. Phys. Rev. Lett., 102:018101, 2009.

[79] A. Ravasio et al. Single-shot diffractive imaging with a table-top femtosecond soft X-ray laser-harmonics sources. Phys. Rev. Lett., 103:028104, 2009.

[80] C.G. Schroer et al. Coherent X-ray diffraction imaging with nanofocused illumination. Phys. Rev. Lett., 101:090801, 2008.

[81] R. Mitzner et al. Spatio-temporal coherence of free electron laser pulses in the soft X-ray regime. Optic Express, 16:19909, 2008.

[82] W. Ackermann et al. Operation of a free-electron laser from the extreme ultraviolet to the water window. Nature Photonics, 1:336, 2007.

[83] J. Arthur et al. LCLS Conceptual Design Report. SLAC-R-593, UC-414, 2002.

[84] M. Bergh, N.O. Timneanu, and D. van der Spoel. Model for the dynamics of a water cluster in an X-ray free electron laser beam. Phys. Rev. E, 70:051904, 2004.

[85] H.N. Chapman et al. Femtosecond time-delay X-ray holography. Nature, 448:676, 2007.

[86] D. Sayre. Some implications of a theorem due to Shannon. Acta Cryst., 5:843, 1952.

[87] C.E. Shannon. Communication in the presence of noise. Proc. Institute of Radio Engineers, 37:10, 1949.

[88] R.W. Gerchberg and W.O. Saxton. A practical algorithm for the determination of the phase from image and diffraction plane pictures. Optik, 35:237, 1972.

[89] J. R. Fienup. Phase retrieval algorithms: a comparison. Applied Optics, 21(15):2758–2769, 1982.

[90] J. W. Goodman. Introduction to Fourier Optics, page 65. The McGraw-Hill companies, 1996 (2nd Edition).

[91] X. Xiao and Q. Shen. Wave propagation and phase retrieval in Fresnel diffraction by a distorted-object approach. Phys. Rev. B, 72:033103, 2005.

[92] K.S. Raines et al. Three-dimensional structure determination from a single view. Nature, 463:214, 2010.

[93] Refer to the discussions between J. Maio and P. Thibault. arxiv:0909.1643, arxiv:0910.0272.

[94] John M. Cowley. Diffraction physics. ELSEVIER SCIENCE B.V., 3rd Edition, 1995.

[95] M. Born and E. Wolf. Principle of optics. Cambridge University Press, 2002.

[96] F. Natterer. An error bound for the Born approximation. Inverse Problems, 20:447, 2004.

[97] J. Miao, D. Sayre, and H. N. Chapman. Phase retrieval from the magnitude of the fourier transforms of nonperiodic objects. J. Opt. Soc. Am. A, 15:1662–1669, 1998.

[98] J. Miao and D. Sayre. On possible extensions of X-ray crystallography through diffraction-pattern oversampling. Acta Crystallographica Section A, 56:596–605, Nov 2000.

[99] D. Sayre. Imaging Processes and Coherence in Physics, page 229. Lecture Notes in Physics, Vol. 112, Springer, 1980.

[100] V. Elser and R. P. Millane. Reconstruction of an object from its symmetry averaged diffraction pattern. Acta Cryst. A, 64:273, 2008.

[101] M. Bertero and P. Boccacci. Introduction to inverse problems in imaging. IOP Publishing Ltd, 1998.

[102] D. Russell Luke. Relaxed averaged alternating reflections for diffraction imaging. Inverse Problems, 21:37–50, 2005.

[103] Heinz H. Bauschke, Patrick L. Combettes, and D. Russell Luke. Hybrid projection–reflection method for phase retrieval. J. Opt. Soc. Am. A, 20:1025–1034, 2003.

[104] Gábor Oszlányi and András Süto. *Ab initio* structure solution by charge flipping. Acta Cryst. A, 60:134–141, Mar 2004.

[105] Gábor Oszlányi and András Süto. *Ab initio* structure solution by charge flipping. II. Use of weak reflections. Acta Cryst. A, 61:147–152, 2005.

[106] V. Elser, I. Rankenburg, and P. Thibault. Searching with iterated maps. Proc. Natl. Acad. Sci. U.S.A., 104:418, 2007.

[107] S Marchesini. A unified evaluation of iterative projection algorithms for phase retrieval. Rev. Sci. Instrum., 78:011301, 2007.

[108] S. Marchesini, H. He, H. N. Chapman, S. P. Hau-Riege, A. Noy, M. R. Howells, U. Weierstall, and J. C. H. Spence. X-ray image reconstruction from a diffraction pattern alone. Phys. Rev. B, 68:140101, 2003.

[109] S. Marchesini et al. Phase aberrations in diffraction microscopy. Proc. 8th Int. Conf. X-ray Microscopy, IPAP Conf. Series 7:380, 2005.

[110] T. Shintake. Possibility of single biomolecule imaging with coherent amplification of weak scattering X-ray photons. Phys. Rev. E, 78:041906, 2008.

[111] Spence J. C. H., Weierstall U., and Howells M. Phase recovery and lensless imaging by iterative methods in optical, X-ray and electron diffraction. Phil. Trans. R. Soc. Lond. A, 360:875, 2002.

[112] Website for calculation of refractive index http://henke.lbl.gov/optical_constants/getdb2.html.

[113] H.C. van de Hulst. Light scattering by small particles, page 35. Dove Publications, Inc., 1981.

[114] A list of Mie scattering codes on website http://atol.ucsd.edu/scatlib/index.htm.

[115] C.F. Bohren and D.R. Huffman. Absorption and scattering of light by small particles. John Wiley & Sons, Inc., 1998.

[116] The code was written by Dr. Warren J. Wiscombe. Refer to [114].

[117] J.M. Cowley and A.F. Moodie. The scattering of electrons by atoms and crystals i. a new theoretical approach. Acta Cryst., 10:609, 1957.

[118] P. Goodman and A.F. Moodie. Numerical evaluation of N-beam wave functions in electron scattering by the multi-slice method. Acta Cryst. A, 30:280, 1974.

[119] K. Ishizuka and N. Uyeda. A new theoretical and practical approach to the multislice method. Acta Cryst., 33:740, 1977.

[120] A.R. Hare and G.R. Morrison. Near-field soft X-ray diffraction modelledby the multislice method. Journal of Modern Optics, 44:31, 1994.

[121] A. Barty et al. Ultrafast single-shot diffraction imaging of nanoscale dynamics. Nature Photonics, 2:415, 2008.

[122] D.P. DePonte et al. Gas dynamic virtual nozzle for generation of microscopic droplet streams. J. Phys. D: Appl. Phys., 41:195505, 2008.

[123] M.J. Bogan et al. Single particle X-ray diffractive imaging. Nanolett., 8:310, 2008.

[124] K.J. Gaffeny and H.N. Chapman. Imaging atomic structure and dynamics with ultrafast X-ray scattering. Science, 316:1444, 2007.

[125] J. Frank. Three-Dimensional Electron Microscopy of Macromolecular Assemblies. Academic Press, Inc., 1996.

[126] V.L. Shneerson, A. Ourmazd, and D.K. Saldin. Crystallography without crystals. i. the common-line method for assembling a three-dimensional diffraction volume from single-particle scattering. Acta Cryst. A, 64:303, 2008.

[127] G. Huldt, A. Szoke, and J. Hajdu. Diffraction imaging of single particles and biomolecules. J. Struct. Biol., 144:219–227, 2003.

[128] G. Bortel and G. Faigel. Classification of continuous diffraction patterns: A numerical study. J. Struct. Biol., 158:10–18, 2007.

[129] G. Bortel, G. Faigel, and M. Tegze. Classification and averaging of random orientation single macromolecular diffraction patterns at atomic resolution. J. Struct. Biol., 166:226–233, 2009.

[130] N. Duane Loh and V. Elser. Reconstruction algorithm for single-particle diffraction imaging experiments. Phys. Rev. E, 80:026705, 2009.

[131] R. Fung, V. Shneerson, D.K. Saldin, and A. Ourmazd. Structure from fleeting illumination of faint spinning objects in flight. Nat. Phys., 5:64–67, 2009.

[132] B. Moths and A. Ourmazd. Bayesian algorithms for recovering structure from single-particle diffraction snapshots of unknown orientation: a comparison. arXiv: 1005.0640, 2010.

[133] N.D. Loh et al. Cryptotomography: Reconstructing 3D fourier intensities from randomly oriented single-shot diffraction patterns. Phys. Rev. Lett., 2010.

[134] J.C. Solem and G.C. Baldwin. Microholography of living organisms. Science, 218:229, 1982.

[135] J.C. Solem. Imaging biological specimens with high-intensity soft X rays. J. Opt. Soc. Am. B, 3:1551, 1986.

[136] A. Patriksson et al. Protein structures under electrospray conditions. Biochemistry, 46:933, 2007.

[137] E. G. Marklund et al. Structural stability of electrosprayed proteins: temperature and hydration effects. Phys. Chem. Chem. Phys., 11:8069, 2009.

[138] T.A. Jones and L. Liljas. Structure of satellite tobacco necrosis virus after crystallographic refinement at 2.5 Å resolution. J. Mol. Biol., 177:735, 1984.

[139] W.L. Jorgensen et al. Comparison of simple potential functions for simulating liquid water. J. Chem. Phys., 79:926, 1983.

[140] D. van der Spoel et al. GROMACS: Fast, flexible, and free. J. Comput. Chem., 26:1701, 2005.

[141] B. Hess et al. GROMACS 4: Algorithms for highly efficient, load-balanced, and scalable molecular simulation. J. Chem. Theory Comput., 4:435, 2008.

[142] F.R.N.C. Maia et al. Structural variability and the incoherent addition of scattered intensities in single-particle diffraction. Phys. Rev. E, 80:031905, 2009.

[143] B. Böttcher, S.A. Wynne, and R.A. Crowther. Determination of the fold of the core protein of hepatitis B virus by electron cryomicroscopy. Nature, 386:88, 1997.

[144] J.F. Conway et al. Visualization of a 4-helix bundle in the hepatitis B virus capsid by cryo-electron microscopy. Nature, 386:91, 1997.

[145] P. Schwander, R. Fung, G.N. Phillips Jr, and A. Ourmazd. Mapping the conformations of biological assemblies. New J. Phys., 12:035007, 2010.

[146] S. Eisebitt et al. Lensless imaging of magnetic nanostructures by X-ray spectroholography. Nature, 432:885, 2004.

[147] S. Marchesini et al. Massively parallel X-ray holography. Nature photonics, 2:560, 2008.

[148] D.K. Saldin, V.L. Shneerson, R. Fung, and A. Ourmazd. Structure of isolated biomolecules obtained from ultrashort X-ray pulses: exploiting the symmetry of random orientations. J. Phys.: Condens. Matter, 21:134014, 2009.

[149] L. Holmegaard et al. Laser-induced alignment and orientation of quantum-state-selected large molecules. Phys. Rev. Lett., 102:023001, 2009.

[150] E. Fehlberg. Classical fifth-, sixth-, seventh-, and eighth-order Runge-Kutta formulas with stepsize control. NASA Technical Report, TR R-287, 1968.

Acknowledgement

First of all, I have to thank Beata Ziaja and Edgar Weckert who brought me into this booming fields of FEL applications. I feel lucky to catch the opportunity to study in DESY, which is a center of FEL frontier researches. Beata Ziaja taught me what is important in scientific researches and writings, and some about life as well. She extended my views of the FEL science as much as possible, with her passion. I was impressed by her social contact with other scientists, which helps to generate new collaborations and projects. We work together like a miniteam. Her encouragement made me more confident of my study and future career. Edgar Weckert is extremely busy, but never forgot his group meeting every week and always knew what we were doing. His sharp eyes and friendly jokes sometimes show his serious concerns about us. I enjoyed very much the discussions with him, and learned how he thought about research problems. He sets an example of a scientist for me.

Henry Chapman always kindly answered any of my questions in a clear way. He taught me all knowledge about coherent diffraction imaging, and the critical attitude on literatures and important questions. I am very happy to learn more from him. I have to thank him for all that he has done for me.

Most experimental results that I mentioned in this thesis came from Thomas Möller and Christoph Bostedt (and their colleagues). I have to thank them for the collaboration in passed several years and the chance for me to analyze the experimental data. Thomas Möller discussed things in a simple but basic way. I appreciate his critical comments on the thesis work.

I want to thank Alexander Lichtenstein for organizing and reviewing my PhD study, from the beginning, and till this end. His kind and positive feedback encouraged me a lot.

During my PhD study, I learned a lot from our group members, especially Ivan Vartaniants, Adrian Mancuso, Andrej Singer, Oleksandr Yefanov. Some questions that confused me have been clarified during the friendly door-to-door discussions. A bunch of people gave useful suggestions on part of this thesis: Adrian Mancuso, Andrej Singer, Mengning Liang, Andrew Aquila, Andrew Martin and A.R.B. de Castro, and I thank all of them. I give my great thanks to Thomas White for helping to revise the thesis on writing style and written English. (If there still exist some defects of language, I will take all the responsibilities.) I want to thank our secretaries, especially Maja Stolper, and International Office at DESY for many helps during this period.

Finally, I leave my millions of thanks to my big families who stand behind me and support me all the time. I give my special thanks to Honglian for staying with me patiently during this hard time of thesis writing. Without her care by heart, I would not have finished it in time.